The role of spatial size and orientation of electronic wavefunction in exciton dissociation at van der Waals interfaces

By

Tika Ram Kafle

Submitted to the graduate degree program in the Department of Physics and Astronomy and the Graduate Faculty of the University of Kansas in partial fulfillment of the requirements for the degree of Doctor of Philosophy

Committee Members

Dr. Wai-Lun Chan, Chair

Dr. Dave Z. Besson

Dr. Hui Zhao

Dr. Judy Wu

Dr. Marco Caricato

Date Defended: 12/03/2019

The dissertation committee for Tika Ram Kafle certifies that this is the approved version of the following dissertation:

The role of spatial size and orientation of electronic wavefunction in exciton dissociation at van der Waals interfaces

_____

Dr. Wai-Lun Chan, Chair

Date Approved: 12/03/2019

Abstract

Organic photovoltaic (OPV) devices are environmental-friendly, lightweight, flexible and inexpensive. However, one of the setbacks for commercial application is its relative low performance in solar to electrical energy conversion compared to inorganic counterparts such as Si solar cells. Unlike typical inorganic materials in which free carriers are generated directly by the light absorption, excitons, Coulombic bound electron-hole pairs, are created upon light absorption in OPV materials. The performance of OPVs depends on how effective the bound charge transfer (CT) exciton, an exciton with its electron and hole spatially separated by the donor-acceptor interface, can dissociate to generate free charge carriers. In this thesis, the roles of the orientation of the delocalized electron wavefunction and the interfacial energy landscape in the exciton dissociation (ED) process are studied in order to understand mechanisms that control the ED efficiency. A number of donor–acceptor interfaces including organic/organic and organic/transition metal dichalcogenides (TMDs) interfaces with different molecular orientations were prepared, and exciton dynamics at these interfaces were probed. We employed time-resolved photoemission spectroscopy to measure the CT exciton dynamics, by which we were able to track the temporal evolution of the energy and the size of CT excitons. Our results on the organic-organic donor-acceptor interfaces show that the relative orientation of the delocalized electron and hole wavefunction within the CT exciton plays an important role in determining whether free carriers can be generated effectively from the CT exciton. Energy uphill, spontaneous exciton dissociation (SED) was observed on the few picosecond (ps) timescale at the zinc phthalocyanine (ZnPc)/fluorinated zinc phthalocyanine (F_8ZnPc) interface with a face-on molecular orientation, at which both the electron and hole wavefunctions delocalize in the direction perpendicular to the interface. By contrast, cooling of hot CT excitons to lower energy

bound CT excitons (cold excitons) was observed at the ZnPc/fullerene (C_{60}) interface with an edge-on ZnPc orientation, at which the hole wavefunction in the CT exciton delocalizes in a direction parallel to the interface. The difference in the CT exciton dynamics suggests that free charges can be generated more effectively at the ZnPc/F_8ZnPc interface with a face-on orientation. In addition, two very similar organic-TMD interfaces (ZnPc/bulk-MoS_2 and ZnPc/monolayer (ML) MoS_2) were studied and distinctly different CT exciton dynamics were observed. At the ZnPc/bulk-MoS_2 interface, after the formation of the CT exciton, back electron transfer occurs which results in the formation of triplet excitons in the ZnPc. On the other hand, at the ZnPc/ML MoS_2 interface, free carriers are generated effectively from CT excitons. This difference in the CT exciton dynamics is explained by the difference in the extent of the interfacial band bending found at the two interfaces. Overall, our study demonstrates that whether free carriers can be generated from the CT exciton depends sensitively on the local energy landscape around the interface and the electron delocalization within the CT exciton at the nanoscale. Understanding how the interfacial structure would affect the temporal evolution of the CT exciton is important for designing interfaces for effective charge generation.

This dissertation includes material from the previously published journals authored by me.

To my family

Acknowledgements

To those who helped me directly or indirectly at various stages of my PhD: Heartfelt thanks!

First, to my advisor Wai-Lun Chan whose invaluable guidance, continuous support, and encouragement have given me the strength and spirit to excel the research and achieve the present stage. I appreciate for the opportunities he provided in an outside of the KU that has helped me to grow professionally. The lessons and the shared experiences from him and his generosity and dedication towards the research have imbued me with a positive mindset to grow further as a researcher and thinker.

To my committee members: Dave Besson, Hui Zhao, Judy Wu and Marco Caricato for their time and effort to review my work and insightful inputs despite of their busy schedule. Thanks to Dr. Zhao and Dr. Wu for the collaborative work, I had with their group. To Siyuan Han for the feedback he provided during my comprehensive exam and the expertise he shared during AP seminar and 516 lab.

I am very much thankful to my lab mates: Ti Wang for introducing me with the experimental method and the measurement techniques. To Bhupal, Shanika, Fatimah, Liang, Aaron and Jack with whom I shared the lab, ideas, joys and worked together at various projects. To my colleagues at condensed matter physics group for the useful conversations we had.

To the entire department: mainly the staff members Joel, Kristin and Kim (former staff) for always being there to help. To chem-store keeper, Donnie Scott, for providing chemicals, gas cylinders and other stuffs on a regular basis.

To my parents for showering their unconditional love and support at all stages of my life and my other family members who have supported me along the way. Most importantly, to my wife, Shristi, for her consistent care, support and keeps telling me, “You can do it!”

“Rock Chalk, Jayhawk!”

Table of Contents

List of Figures

1. Introduction

1.1 A brief history of Photovoltaics

Since the Earth's formation, solar energy has been an essential source of lighting, warming, food and water directly or indirectly for all the living creatures. With the evolution of the humankind, solar energy is being used in various forms. Thanks to the advancement in science and technology for developing methods to harvest solar energy as electricity. Electric current can be created in a material system upon absorption of light; this effect is known as photovoltaic effect. Light consists of energy packets called photons. The energy of light photons depends on the frequency/wavelength of light. Mostly, the light photons from infrared to ultraviolet range have sufficient energy to excite electrons across the bandgap of semiconducting materials from which charge carriers can be generated to produce electrical current.

The first photovoltaic effect was demonstrated by Edmond Becquerel in 1839, experimenting with an electrolytic cell.[1] In 1883, Charles Fritts created the first solar cell that used Selenium wafers coated with gold film.[1] Early solar cell comprised of metal electrodes and semiconductors, in which the electrodes hindered the transmission of incident light; hence, they had a very low efficiency, less than 1%. After the observation of photoelectric effect by Heinrich Hertz in 1883, and its theoretical explanation by Albert Einstein in 1921, photovoltaic technology started garnering attention. In 1954, Daryl Chapin, Calvin Fuller, and Gerald Pearson developed the Silicon photovoltaic with 4% efficiency at Bell Labs that was capable to run daily electrical equipment. Progress in PV technology was advancing and in the late 1960's, satellites Vanguard, Explorer, and Sputnik were launched with PV-powered systems on board. Since then, various satellite power stations have been successfully operated with increased power conversion

efficiency. Attracted by the photovoltaic technology, search for improved performance of PVs led to successful development of PVs made up of Cadmium sulphide (CdS), Cadmium telluride (CdTe), Gallium arsenide (GaAs) in 70s and 80s.[1] These PVs have their own advantages and limitations. For example, CdTe is cheap and has more power conversion efficiency but it is chemically risk to environment. Likewise, GaAs has record-breaking efficiency of 29.1% for single junction[2] but the technology is expensive. Similarly, perovskite based solar cells has higher efficiency but it has stability issue i.e., it loses its efficiency when exposed to light. To date, Si-based solar cells are optimum with efficiency 27.6%[3] over other technologies in terms of optical, electronic, thermal, mechanical properties and environmental concerns. According to National Renewable Energy Laboratory, the percentage of electricity generation from solar cells has increased 47 times since 2008, though their net contribution to the total electric generation is low (~ 5%).[4] In particular, most of the contribution, among solar cells, comes from Silicon-based PV devices. However, for large production scale, their installation requires specific space such as flat area, and hence requirement of designing them into a structural shape for effective performance generates a lot of wastage. On the other hand, the use of highest contributor, coal and natural gas, has dropped down from 71% to 63% in the same time-period. Due to the increasing demand of energy supply and limited oil resources, alternative sources of energy is essential. Other forms of energy like nuclear energy, hydro energy, and wind energy can be sought as an alternative but environmental impacts, cost, efficiency and non-practical for daily use could be some serious limitations. In this context, search for cost effective, environment friendly, flexible and efficient alternative source of energy is ongoing. In the next section, we will be focus on organic photovoltaics, an alternative material for converting light energy to electricity.

1.2 Organic Photovoltaics

OPV devices make use of semiconducting organic materials to convert solar energy to generate electricity. Organic compounds are abundant in nature, and can be chemically synthesized and carefully modified to tailor certain properties like band gap, electron affinity, morphology etc. Hence, compared to conventional semiconducting materials such as silicon, organic semiconducting materials have advantages such as low production cost and applicability in flexible electronics.[5-7] In addition, they are eco-friendly and have tunable band gap for light absorption. As a result, they are suitable for low-cost solar energy conversion. Research on OPV materials have flourished in recent years. The present efficiency of organic solar cells has reached over 16% for single junction bulk heterojunction devices (BHJs), but it is still poor compared to their inorganic counterparts, Si-based first generation solar cells (~ 27.6%).[3] Likewise, thin film based second-generation solar cell technologies (CdTe, CIGS) have efficiency (~ 25%) close to Si-based solar cells but its higher cost for mass production and other limitations discussed above has made this technology uncompetitive in the market. Hence, the efficiency of OPVs must be increased to become economically competitive. However, the performance of OPV devices has been steadily increasing since a major breakthrough in 1986 with efficiency of 1%.[8] These improvements result from the development of new low-band gap polymers and the use of device architectures such as tandem solar cells and nano-structured BHJs.[9] Potentially, the efficiency can be increased further with the usage of new charge generation mechanism such as singlet fission.[10-11] This makes OPVs a potential runner for the third generation solar cells.

OPV devices consist of two active layer materials: donor and acceptor. These organic materials are semiconducting and generally have a low dielectric constant (~ in the range of 3 –

4).[12] The Coulomb screening effect is weak and the interaction between charges is strong. Upon the absorption of photons, they form bound electron-hole pairs called excitons. Unlike their inorganic counterparts, these excitons need to be dissociated in order to generate free charges. Theoretically, the binding energy (E_B) for an electron-hole pair is given by:

$$E_B = \frac{e^2}{4\pi\varepsilon_o\varepsilon_r r}$$

where e is the electronic charge, ε_o is the permittivity of free space, ε_r is dielectric constant of the organic material and r is the distance between electron and hole. The low dielectric constant results in a large binding energy (0.1 to 1.0 eV)[13] which is fairly above the thermal energy (0.025 eV) at room temperature. Usually, this binding energy can be determined experimentally by:

$$E_B = E_{TG} - E_{OG}$$

In this equation, E_{TG} is transport gap, which is equivalent to the energy required to form an unbound electron-hole pair. E_{OG} is optical band gap, which is equivalent to the minimum energy required to form an exciton by optical excitation. To generate photocurrent, the bound charge pair must separate before they recombine. The charge neutral exciton undergoes a diffusion process and reaches donor-acceptor interface. The donor-acceptor interface is a heterojunction with a type-II band alignment as shown in Figure 1.1. The type-II band alignment is energetically favorable for charge transfer as the band-offset (difference in LUMOs of donor and acceptor) at the interface provides the driving force for the exciton dissociation (ED). The path 1 in Figure 1.1 shows optical excitation of an electron to form an exciton. The electron transfers from the electron donor to the electron acceptor (path 2) but the hole resides in the same layer, thus it creates a so-called charge transfer (CT) exciton state. Finally, the CT exciton follows the path 3 where it dissociates into a free electron and a hole to form a charge separation (CS) or

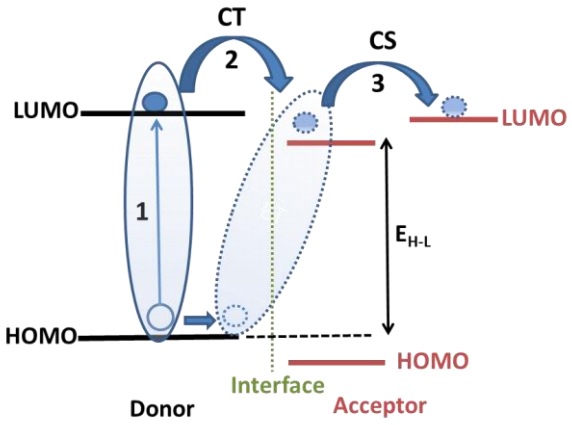

Figure 1.1: Type II band alignment for charge transfer in OPVs. The LUMO of acceptor is below than that of donor and this offset can act as a driving force for electron transfer. The path 1 shows optical excitation, the path 2 shows electron transfer from the donor to the acceptor to form a charge transfer (CT) exciton and the path 3 directs to charge separated (CS) state.

ED state. The free charge carriers then move towards the electrodes in response to external electric field and hence electricity is generated.

The efficiency of the OPVs cells directly depends on the open circuit voltage (V_{OC}) between the donor and the acceptor. For an ideal case, V_{OC} has the maximum theoretical value equivalent to the difference between HOMO of the donor and LUMO of the acceptor ($E_{H\text{-}L}$). In practice, there is always some energy loss (Δ) due to various factors like recombination, interfacial energetic disorder, defects etc.[14-16] Thus, the actual V_{OC} turns out to be

$$V_{OC} = \frac{1}{e}(|E_{H-L}| - \Delta)$$

One of the major factors contributing for the energy loss in OPV cells is the CT state exciton binding energy, which is roughly around 0.5 eV for most of the OPV cells. Reducing this binding energy can help in effective exciton dissociation without significant loss of $E_{H\text{-}L}$ voltage; hence this can push the present efficiency of OPVs closer to that of conventional cells.

As shown in Figure 1.1, in-depth understanding of light photon absorption, CT and CS process can help in the material selection and the architectural design, which can increase the overall efficiency of photocurrent generation. Among these, the mechanism of CS is under continuous debate and fundamentally intriguing. The major question is; how the Coulomb bound CT exciton overcomes the large binding energy to produce free charge carriers. Different mechanisms have been proposed to understand separation of excitons at organic semiconductor interface. For example, it has been proposed that the interfacial dipoles formed at the donor – acceptor interface can lower the energy barrier for the charge separation.[17-19] On the other hand, some researchers suggest that the entropy gain when an electron and a hole moves away from each other can lower the actual barrier for exciton dissociation.[20] The number of configurations of the electron-hole pair increases when the average distance between them increases, which increases the total entropy. The change in the Helmholtz free energy ΔF is related to the change in the entropy ΔS by:

$$\Delta F = \Delta E - T\Delta S$$

Therefore, the free energy can decrease during ED even though the change in the potential energy of the bath ΔE is positive. The microstructure of the interface can also affect the charge separation efficiency. It is argued that structures with intermixed donor and acceptor nano-crystallites are essential for effective charge separation. The binding energy is reduced in the crystalline structure due to a larger distance between the electron and the hole in the CT excitons.[21-23] Other researchers propose that doping[22] and charged defects can influence the exciton separation mechanism.[22, 24] While each of these proposals is relevant in explaining ED within a certain material system and/or experimental condition, no consensus has emerged from these studies to explain ED mechanism. Indeed, because of the lack of control at the interface

structure and other experimental conditions, some of these works seem to contradict each other without a proper justification. Therefore, an in-depth understanding of the ED mechanism is required in further improving the efficiency of the OPV devices.

1.3 Exciton dissociation mechanisms at donor – acceptor interface

As discussed above, the low dielectric constant of organic semiconductors cannot provide effective screening to the Coulomb attraction between an electron and a hole, thus it results in the formation of an exciton. The binding energy of the exciton can be as large as ~ 1.0 eV, which is much larger than the thermal energy at room temperature (~ 0.025 eV). Therefore, the CT exciton cannot produce free carriers effectively merely by thermal activation. Among the different pictures proposed for exciton dissociation so far, it can be broadly classified into conventional and hot CT picture. The conventional picture of exciton dissociation is presented in Figure 1.2a. In this picture, the electron from the exciton in the donor transfers to the acceptor at the interface, which is a CT exciton state where the electron and hole are still bounded by the Coulomb force. To separate the electron from the hole (CS state), it needs to overcome an energy barrier that is equal to the exciton binding energy. The CT exciton usually has a short lifetime because of the close proximity of the electron and hole. The short lifetime together with the large energy barrier, makes exciton dissociation an unlikely event compared to the charge recombination at the interface. This apparently contradicts the fact that some organic solar cells can have a rather high internal quantum efficiency (defined as the number of free electron hole pairs generated per absorbed photon) that can approach unity at selected wavelengths.[25] To explain the effective charge separation, it is proposed that the excess energy originated from the band offset produces the so-called hot CT states.[26] This picture is presented in Figure 1.2b. This hot CT state can dissociate before it relaxes to the lower energy CT state without overcoming the

exciton binding energy. The hot-CT model, in general, can explain the effective exciton dissociation. However, the model itself does not provide the physical origin of these hot CT excitons.

For organic materials, it is often assumed that an exciton localizes on a single molecule. According to this assumption, an exciton is first required to diffuse to interface before the charge separation can occur. For a typical solar cell structure with nm-sized (1-10 nm) aggregates, the exciton diffusion time is in the range of picoseconds to nanoseconds (ps – ns). This does not comply with recent studies in which the majority of the charge carriers are found to exist within

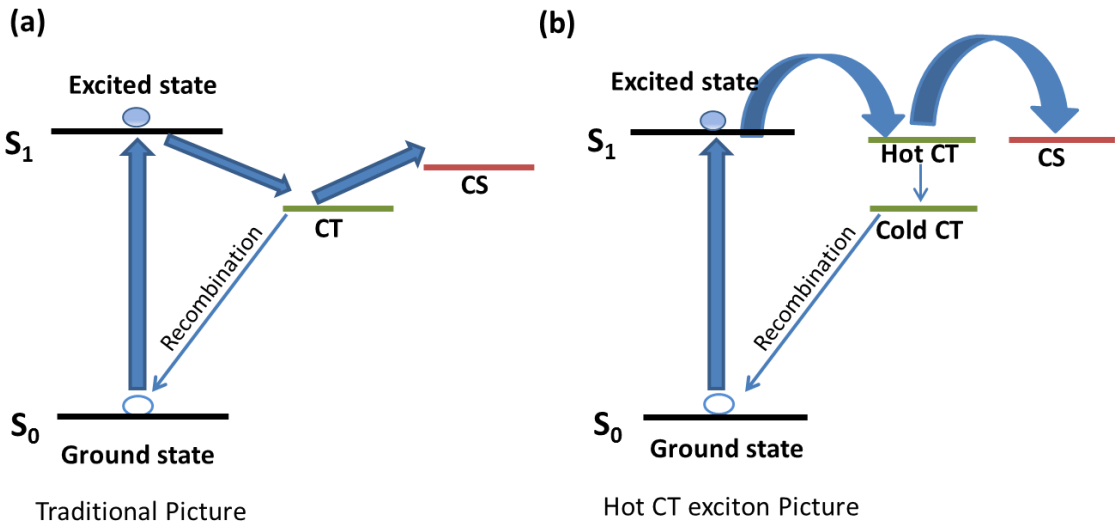

Figure 1.2: Schematics of exciton dissociation mechanism at donor – acceptor interface: (a) conventional picture and (b) hot CT exciton picture.

a few picosecond after photoexcitation.[27] One explanation of such findings is that the exciton wavefunction is delocalized. The larger coherent size of the exciton allows it to interact with the donor/acceptor interfaces without the need for slow incoherent diffusion process.

Similarly, a CT exciton consists of a delocalized electron and a hole. Efforts have been made to explain the origin of the hot CT states with this delocalization mechanism. For example,

Savoie *et al.* have studied the delocalization of the electron in the CT exciton using large-scale simulation.[28] Figure 1.3 gives a schematic view of this work. A point positive charge (+) was placed in front of an acceptor crystallite to see how it affected the energies and sizes of electronic states in C_{60} acceptors. The vertical axis is the energy of electronic states referenced to the vacuum level. The horizontal axis is the spatial delocalization (left), and number of acceptor molecules covered by the wavefunction (right). Each dot in 1.3a represents an eigenstate and the colored dots are the states visualized in 1.3b. The left panel of Figure 1.3b shows the lowest energy eigenstate is localized spatially and confined to a single acceptor molecule as expected for a bound CT state. However, the next eigenfunction is delocalized over several molecules (right panel). In general, eigenstates with higher energies have larger delocalization sizes and they are called hot CT states. From the energy conservation point of view, charge separation *via* resonance/delocalization states should be quicker and more effective than the bound CT state. In addition, a larger crystallite size will have a higher number of delocalized states. These delocalized states can convert into free carriers without the need of thermal activation. Thus, a better crystallinity with larger crystallite sizes should promote charge separation.

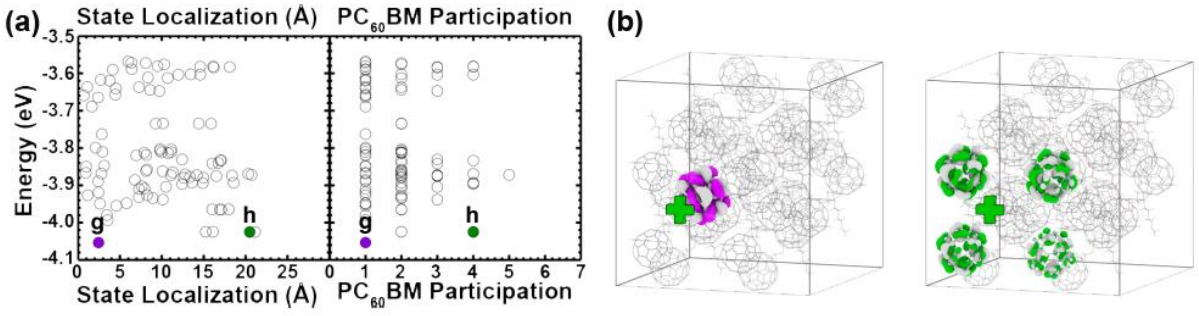

Figure 1.3: Effect of point positive charge on spatial extent of CT states in acceptor. Each dot in (a) represents the eigenstates and the colored dots are the states whose eigenfunctions are visualized in (b). (b) shows the eigenfunction with size contraction (left) and delocalization (right) of corresponding eigenstate in (a). "Figure adapted with permission from reference [28][28] Copyright (2014) American Chemical Society."

Besides the point charge, Savoie *et al.* also did study on charge separation by using a line (1D) and a plane (2D) of positive charges with its orientation parallel and perpendicular to the acceptor surface. They found that a plane of positive charges oriented perpendicular to the acceptor surface enhances the delocalization of CT states as compared to a line of positive charges oriented in the parallel direction.[28] Therefore, the orientation of the molecules can play an important role in controlling the charge separation mechanism.

1.4 Organization of the Dissertation

This dissertation primarily focuses on the role of electron and hole wavefunction orientation and energy landscape at the donor – acceptor interface to investigate ED mechanism. The structural organization of the dissertation is discussed below.

The second chapter will deal with experimental techniques applied for sample preparation, characterization and measurement. First, two photoemission spectroscopy techniques – Ultraviolet photoemission spectroscopy (UPS) and time resolved-two photon photoemission (TR-TPPE) techniques will be discussed. The underlying theory, experimental set-up and the data analysis procedure for these two techniques will be explained. Second, we will describe thermal evaporation deposition technique. How we grow and control orientation of organic molecules on various substrates will be illustrated. Finally, we will briefly introduce the atomic force microscopy (AFM) and low energy electron diffraction (LEED) techniques used to characterize our sample.

In the third chapter, how the CT state and CT exciton delocalization size are measured using TR-TPPE technique will be demonstrated. Using ZnPc – C_{60} on Au as a model system, the hot and cold CT states arising due to CT from ZnPc to C_{60} are spectrally resolved. The CT exciton

delocalization size is determined from the temporal dynamics of the CT state by varying the C_{60} film thickness.

In the fourth chapter, CT and ED dynamics will be compared on two different molecular orientations – face-on and edge-on. F_8ZnPc – ZnPc on HOPG (highly oriented pyrolytic graphite) maintains face-on while F_8ZnPc – ZnPc on SiO_2 has edge-on orientation. Interestingly, only the former system exhibits the spontaneous exciton dissociation (SED) at an ultrafast time scale. How the SED is originated due to perpendicular orientation of electron-hole wavefunction at face-on interface will be illustrated. Results from sub-band gap photoexcitation of this system will also be shown, which precludes the assumption that hot CT exciton is the kinetic pathway (see Figure 1.2b) for ED. On the other hand, the electron-hole wavefunction has parallel orientation at edge-on interface, which does not favor SED. CT exciton dynamics in ZnPc – C_{60} on Au, in which ZnPc has edge-on orientation, will also be discussed. Results show the relaxation of hot CT excitons into cold CT excitons – a favored kinetic pathway for edge-on molecular orientation.

The effect of the interfacial energy landscape on exciton dissociation process will be focused in chapter 5. Organic – 2D heterostructure comprised of ZnPc – MoS_2 system will be introduced for the study. ZnPc maintains face-on orientation on both bulk-MoS_2 and monolayer (ML) MoS_2. While both systems show type II band alignment at the interface, notably ZnPc's HOMO exhibits more band bending in ZnPc – bulk-MoS_2 compared to ZnPc – ML-MoS_2 system. Free charge carrier generation is observed in ML system due to less band bending while the back electron transfer occurs in bulk system due to increased band bending. Finally, results from type I band alignment in ZnPc – bulk-WSe_2 system will be discussed in brief, where both electron and hole transfer takes place from ZnPc to WSe_2 and recombination occurs consequently. This

illustrates the importance of type II band alignment as a pre-requisite for CS but does not necessarily guarantee.

At last, we will summarize our experimental findings. A brief outlook on the present and future direction of the research field will also be discussed.

2. Experimental Techniques

2.1 Introduction to Photoemission Spectroscopy

The proposed research requires measurement of band alignment between donor and acceptor at interface. In addition, detection of charge transfer (CT) states and understanding of subsequent exciton dynamics is essential. This requires measurement of filled electronic states and energy, population and time dynamics of excited states. Two different photoemission techniques – Ultraviolet photoemission spectroscopy and time resolved-two photon photoemission spectroscopy (TR-TPPE) are used for the measurement. Photoemission spectroscopy (PES) is a technique based on the photoelectric effect, a phenomenon in which free electrons are emitted when a material absorbs light of certain frequency. It was originally observed by Heinrich Rudolf Hertz in 1887 as sparkling between the two metal electrodes resulting in voltage change when ultraviolet beam was shined on the electrodes.[29] Later Philip Lennard did control experiment and showed that the intensity of light had no effect on the kinetic energy (E_{kin}) of the emitted particle, instead the light frequency was responsible for it. In 1905, Albert Einstein was able to explain this discrepancy by treating each light particle as quanta (photon), packets of discrete energy, which depends on the frequency of light.[30] According to which, a light photon of a certain frequency *(f)* interacts with an electron inside the sample and ejects it above the vacuum level (E_{vac}), an energy level beyond which the electron is free from the material surface. The threshold frequency required to emit electrons from a certain energy level is the characteristic of the material and is referred as the binding energy (E_B) of the electrons.

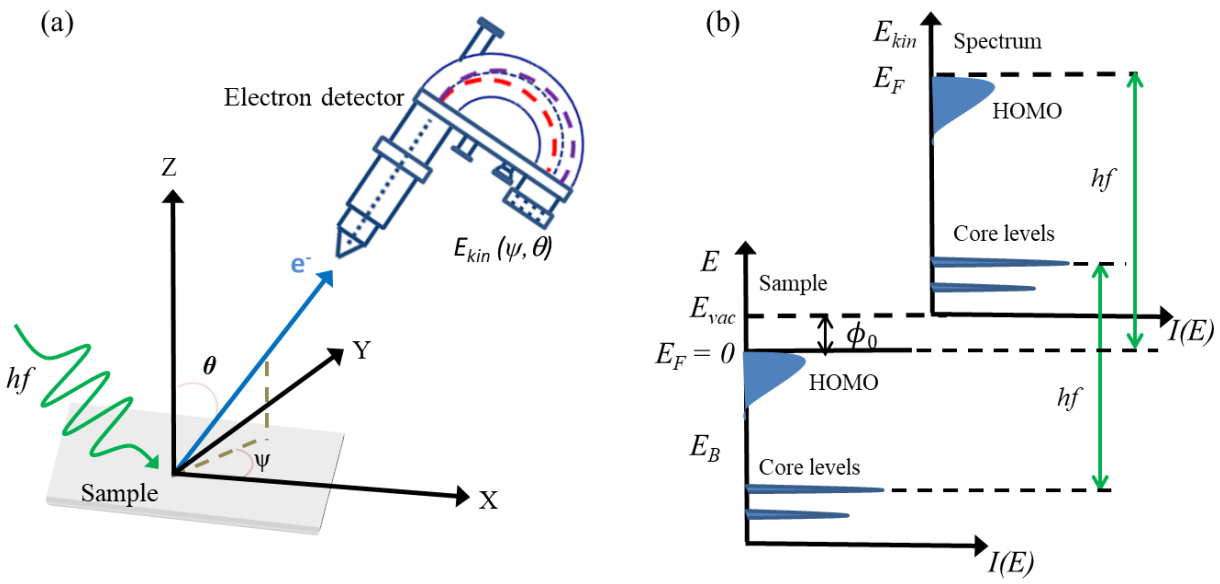

Figure 2.1: (a) Principle of photoemission spectroscopy. Monochromatic photons with energy *hf* hits the sample surface to eject the electrons. The E_{kin} of the photoelectrons is anlaysed by the electron detector. (b) Energetics of the photoemission process is mapped to the energetics as read by the detector. Electrons with binding energy E_B absorb energy *hf* and escape into the vacuum, becoming photoelectrons with kinetic energy $E_{kin} = hf - \boldsymbol{\phi_0} - E_B$.

Figure 2.1a shows the schematic of the PES. A monochromatic light with photon energy *hf* greater than the E_B impinges on a sample surface and ejects electrons above the E_{vac}. The electron detector measures intensity and E_{kin} of the photo-emitted electrons, which gives a plot of photoemission intensity *I(E)* as a function of the electron E_{kin}. This allows us to determine the binding energy (E_B) of the electrons before the photoemission and hence, the possible electronic states of an atom/molecule. The schematic of the energy levels in PES is shown in Figure 2.1b. The scale of PES energetics (lower diagram) is mapped in accordance to the PES spectrum read by the detector (upper diagram). The core levels have higher E_B and hence they read lower E_{kin} in the spectrum measured by the detector. The HOMO levels (valence bands in inorganic materials) are near the fermi level (E_F) and hence they have least E_B that corresponds to the highest E_{kin} in the spectrum. Thus, the kinetic energy distribution reflects the binding energy distribution of the

electrons. Taking work function (ϕ_0) of the sample into account and referencing the binding energy with respect to the Fermi level (E_F), the relationship between E_{kin}, ϕ_0, and E_B can be governed by the equation:

$$\boldsymbol{E_{kin} = hf - \phi_0 - E_B} \tag{2.1}$$

PES has been a powerful technique to probe occupied and unoccupied electronic states of material. Based on the probing objective, improved PES techniques with different photon source exist. Some of the widely used PES techniques are:

1. X-ray photoemission spectroscopy (XPS) – This technique uses X-ray to irradiate the material to study the electronic states and chemical analysis of inner core levels.
2. Ultraviolet photoemission spectroscopy (UPS) – It employs ultraviolet photons to study the HOMO level/outer shell electrons of the material.
3. Angle-resolved photoemission spectroscopy (ARPES) – This method maps a direct measurement of E_{kin} and momentum of electrons resulting to detailed band dispersion/electronic structure and fermi surface of the material.
4. Inverse photoemission spectroscopy (IPES) – It is a complementary to UPS technique used to study the unoccupied states near the fermi level.
5. Two-photon photoemission spectroscopy (TPPE) – This technique makes use of two photons to study occupied and excited electronic states. Since one of the photon can be controlled in time, it allows tracking the time dynamics of excited electronic states.

Three Step Model

The semi-classical approach of photoemission treats photon absorption, electron escape and detection as a single coherent process and is referred as one-step model. However, one step-model is very complex to deal with, hence a well-established three step model is used for a detail

quantum mechanical description of the photoemission process.[31-33] While the theoretical explanation of the three-step model is beyond the scope of this thesis, we will discuss the scheme of this model in brief.

(1) Photoexcitation of electrons: A photon interacts with a single electron in the material and excites to an unoccupied state. The transition probability ω_{fi} for an optical excitation between N-electron ground state Ψ_i^N and one of the possible final states Ψ_f^N is given by the Fermi's golden rule.[31]

$$\omega_{fi} = \frac{2\pi}{\hbar} \left|\left\langle \Psi_f^N \middle| H_{int} \middle| \Psi_i^N \right\rangle\right|^2 \delta\left(E_f^N - E_i^N - h\nu\right) \tag{2.2}$$

where $E_i^N = E_i^{N-1} - E_B^{\boldsymbol{k}}$ and $E_f^N = E_f^{N-1} + E_{kin}$ are the initial and final-state energies of the N-particle system. During this process, the wavefunction could be factorized into N-1 electron terms and a photoelectron. However, during the photoemission process the system itself will relax. The *sudden approximation i*s applied in order to simplify the problems. The *sudden approximation* is in principle applicable to the high kinetic energy electrons. It assumes that photoemission is so instant that it hardly interacts with (N-1) electron system. The final state Ψ_f^N can be written as:

$$\Psi_f^N = A\phi_f^k \, \Psi_f^{N-1}$$

where *A* is an antisymmetric operator that properly antisymmetrizes the N-electron wavefunction to satisfy the Pauli principle. The total transition probability is given by the sum over all possible excited states *m* such that $\left|c_{m,i}\right|^2 = \left|\left\langle \Psi_m^{N-1} \middle| \Psi_i^{N-1} \right\rangle\right|^2$ is the probability that the removal of an electron from state *i* will leave (N-1) electrons in the excited state *m.*

(2) Transport of excited electrons to the sample surface: Here the excited electron travels to the surface of the material with a probability proportional to its mean free path assuming that

scattering of electrons do not occur. However, photoelectrons can interact with electrons and phonons that affect the mean free path. Since the mean free path is very small for the UV photon range, the sample surface must be contamination free and clean.

(3) Escape of photoelectrons: The final step explains the transmission probability of photo-emitted electrons from the surface to the vacuum. Photo-emitted electrons with kinetic energy greater than the work function of the sample ($E_{kin,} > \phi_0$) can escape into the vacuum. Most of the semiconductors we studied have work function in the range of 4 – 6 eV.

As discussed earlier, my research requires probing of filled electronic states and excited states at the interface for which UPS and TPPE are the ideal PES techniques. These two experimental methods are extensively used in our research and will be discussed in the next section. ARPES, in our case, is used for the characterization of the material and will be discussed in brief.

2.2 Ultraviolet Photoemission Spectroscopy (UPS)

In UPS, the ultraviolet beam (5 - 100 eV) is used as a photon source. In our lab, photon energy is obtained by ionization of Helium gas i.e., line spectra corresponding to He I_α – 21.22 eV and He II_α – 40.82 eV energy. First of all, a well-prepared sample is kept facing normal to the electron detector. The UV photon impinges on the sample to knock-off the electrons to vacuum and the electron detector measures intensity of the photo-emitted electrons as a function of $E_{kin.}$ In general, the photoemission process is explained by three step model discussed earlier.

Surface sensitive

The escape depth of electrons is very small, just a few nanometers (1 – 2 nm) for the energy range of UV photons used in our experiment, which means the UPS technique detects electrons only from the top surface. Thus, the sample has to be atomically clean and free from

adsorbed contaminants to investigate the surface electronic states. This makes UPS a surface sensitive technique, which requires an ultrahigh vacuum chamber with pressure below 10^{-10} Torr. In order to quantify this, we can introduce sticking coefficient. In surface physics, sticking coefficient (S) is the ratio of the number of adsorbate atoms or molecules that stick to a surface to the number of total molecules impinging on it during the same period of time[31]. The sticking coefficient is a function of surface temperature, surface coverage, structural details and kinetic energy of the impinging molecules. In general, for S=1, it needs an exposure of nearly 2.5 Langmuirs (1L= 10^{-6} torr-s) for a monolayer coverage. Our chamber can be as kept as low as 2.5×10^{-11} Torr, hence it would take approximately 27 hours to cover one monolayer on the surface. The sticking coefficient can vary depending on the materials and molecules. Most of our sample can survive in UHV chamber for several days. If the sample remains for a longer time, we anneal the sample around 100 °C to outgas any adsorbed air molecules. In order to maintain an ultrahigh vacuum, two turbo pumps, a mechanical pump backs each of which, pump the main chamber. In the cases, when the chamber is exposed to air, baking is performed, a process of heating the chambers to outgas the trapped molecules and adsorbed contaminants so that the desired pressure is attained.

Analysis of UPS spectrum

Figure 2.2a shows the energy distribution curve (EDC) obtained from UPS with He I – 21.22 eV. The position of secondary electron cut off (SECO), HOMO peak and the fermi level (E_F) is marked with blue arrow. Figure 2.2 b and c is the UPS spectrum near SECO and HOMO region respectively labelled in terms of binding energy with respect to E_F. As discussed earlier, the electrons with highest kinetic energy has least binding energy and vice-versa. The electrons near

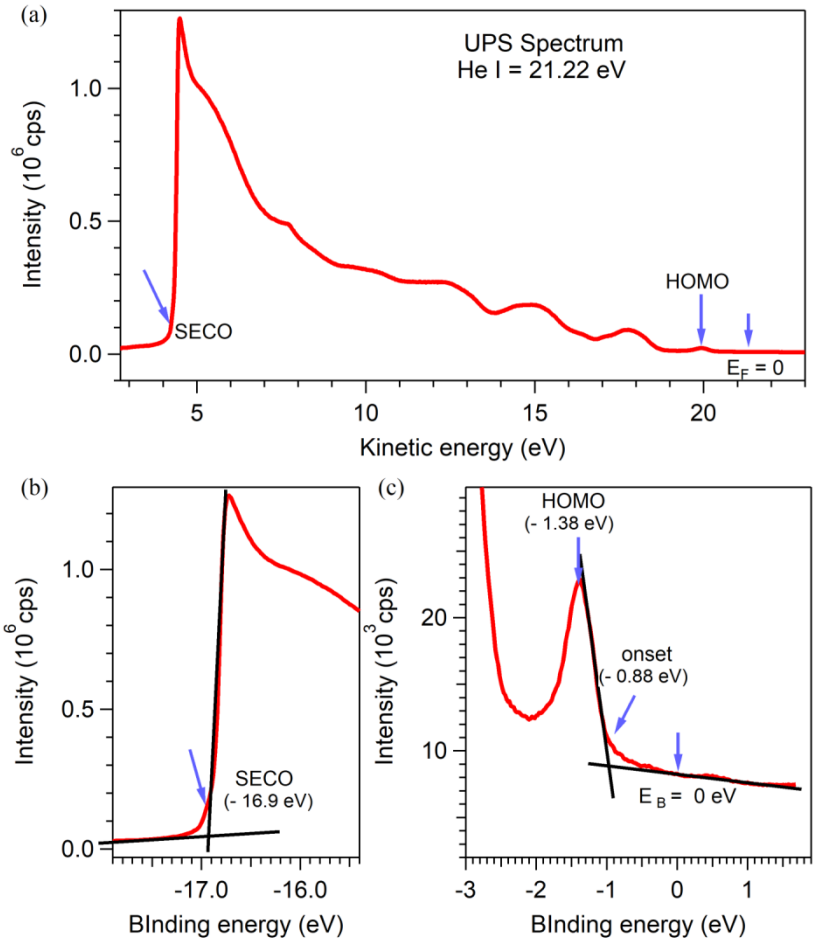

Figure 2.2: (a) UPS spectrum of 10 nm ZnPc/HOPG collected with photon energy of He I = 21.22 eV. The SECO marks the onset of inelastic electrons. The same UPS spectrum referenced w.r.t binding energy (b) near SECO region and (c) near HOMO region.

the E_F do not undergo any inelastic collision and has the maximum kinetic energy. They preserve information of initial electronic states and hence represent density of electronic states. The first peak below E_F is referred as HOMO peak, a filled orbital in organic semiconductors (similar to valence band in inorganic semiconductors). On the other hand, deeper electrons undergo inelastic scattering within the material before they are photo-emitted. Such electrons are called secondary electrons. They lose the information of initial states. As the kinetic energy decreases, we observe increase in intensity of the secondary electrons. Finally, a sharp drop in intensity is seen when

the kinetic energy reaches a minimum value. The onset of the secondary electrons is referred as secondary electron cut-off (SECO).

Work function, Ionization Potential and HOMO/VBM

UPS spectrum is used to determine work function, ionization potential (IP) and occupied electronic states of the sample. Theoretically, the work function of sample is the minimum energy required to free electrons from the sample. The SECO position in the UPS spectrum can be directly used to determine work function (ϕ_0) of the sample. From the above UPS spectrum (Figure 2.2a), the SECO is at 4.32 eV and hence the ϕ_0 of the sample is 4.32 eV. In energy band diagram, work function is the difference between E_F and E_V level (see Figure 2.1b) and experimentally it is equivalent to the energy difference between the supplied photon energy and the maximum E_B (minimum E_{kin}) i.e., $\phi_0 = hf - E_{Bmax}$. From figure 2.2b, the absolute value of E_{Bmax} is 16.9 eV, thus ϕ_0 of ZnPc is 4.32 eV. Likewise, the HOMO peak position can be directly measured from the spectrum. The measured HOMO of ZnPc is 1.38 eV below the E_F (Figure 2.2c). The onset of the HOMO peak is at 0.88 eV below E_F and it is used to determine the ionization potential (IP). IP is the minimum energy required to remove a bound electronic state from the material and is given by the relation:

$$\boldsymbol{IP = hf - |SECO_{onset} - HOMO_{onset}|} \tag{2.3}$$

Plugging in all the values, the calculated IP value is 5.20 eV. With the information of E_{kin}, ϕ_0, and photon energy, the binding energy of various other electronic states can be determined by rearranging the equation 2.1.

$$\boldsymbol{E_B = hf - \phi_0 - E_{kin}} \tag{2.4}$$

The momentum of the outgoing electrons is determined from its E_{kin} and is given by:

$$\boldsymbol{p = \sqrt{2mE_{kin}}} \tag{2.5}$$

For crystalline materials, ARPES measurements are performed that gives the information on the band dispersion of the material. By changing the angle (ψ, θ) and collecting the electrons in angle mode of the detector, the band dispersion of crystalline materials can be obtained. The APRES spectrum shows angular dependent intensity and is specific to material.

2.3 Time Resolved -Two Photon Photoemission (TR-TPPE)

This photoemission technique, based on photoelectric effect, allows the investigation of unoccupied/intermediate states in metals and semiconductors. It employs two femtosecond laser pulses with their energies chosen in such a way that the first laser pulse, the pump, excites an electron from its initial state (E_B) to an unoccupied state (below E_V). The second laser pulse, the probe, kicks out the electron to vacuum. A hemispherical electron detector, equipped with CCD camera measures population and E_{kin} of the ionized electrons with respect to the E_V. The schematic of the TPPE process is shown in Figure 2.3. Applying the energy conservation rule, the binding energy of the intermediate state (E_{Bi}) can be determined by rearranging equation 2.4. Note that the photon energy *hf* is the probe energy (E_{pr}) here and the energy will be referenced with respect to the E_{vac} level. The E_{Bi} takes the absolute value since it is the unoccupied state above E_F.

Next, TPPE also allows to measure temporal dynamics of the intermediate state by changing optical path difference between the pump and the probe pulse via a computer controlled delay stage. The optical path (μm – cm) can be directly correlated with time, hence our experimental set-up enables us to capture the intermediate state dynamics from fs – ps range.

Since most of the events like CT and CS occur within sub-ps range for the system we investigate, it is critical to have laser pulse-width time shorter or comparable to the lifetime of excited states. The lifetime of excited states can be obtained using appropriate mathematical model to fit experimental data since the lifetime and the dynamics can vary depending on the system we investigate. Thus, the mathematical model will be discussed accordingly as they appear while interpreting the data. It is noteworthy to mention here that the intermediate energy state obtained by rearranging equation 2.4 could be lower, higher or remain in the steady state depending on the energetics of the system under study and the pump energy provided. For example, if an organic semiconductor is pumped with energy higher than its optical excited state, the exciton could quickly lose energy to relax into its optical excited state. On the other hand, in a donor-acceptor system, the energy level of a free electron becomes higher if exciton dissociation occurs. TPPE has the capability of tracking the evolution of excited state in terms of energy and femtosecond time resolution, hence it is used to study variety of electron/exciton behaviors in metals, semiconductors, and hybrid interfaces.

Experimental Configuration

The schematic of the experimental set-up is shown in Figure 2.3 It can be mainly categorized into three units: femtosecond laser unit, optical beam path and UV chamber in conjunction with electron analyzer.

Femtosecond laser: It consists of two non-collinear optical parametric amplifiers, Orpheus-N, pumped by the PHAROS laser unit. PHAROS is a compact femtosecond laser system, built upon chirped amplification technique, employing seed oscillator, regenerative amplifier and pulse stretcher/compressor modules.[34] Yb:KGW acts a lasing medium for the regenerative amplifier with repetition rate tunable from single pulse to 1 MHz at wavelength centered at 1028 nm.

Other tunable parameters include: pulse duration (< 290 fs -10 ps), pulse energy (up to 2 mJ) and average power (up to 20 mW). The parameters can be easily set via user-controlled software installed in laptop PC. The two Orpheus-N, pumped by PHAROS, has built in second harmonic (Orpheus-N-2H) and third harmonic generator (Orpheus-N-3H) producing 514 nm or 343 nm pump. The wavelength is tunable from 650-900 nm (by Orpheus-N-2H) and 520-670 nm range (by Orpheus-N-3H) via computer controlled stepping motor stages. The second harmonic of the output wavelength can further be generated in external environment extending the wavelength range down to 250-450 nm. Their built-in pulse compressor generates pulses < 30 fs thus, making ORPHEUS-Ns a suitable instrument for time resolved spectroscopy.

Optical Path: The typical optical beam path for TR-TPPE is shown in Figure 2.3. It comprises of two paths, pump beam path and probe beam path, both paths eventually lead the pulses to the sample in the UV chamber. The pump beam emerging from the Orpheus-N-2H, follows the optical path marked with red color. The beam traverses through a delay stage that undergoes translational motion and enables us to control the optical path travelled by the pump beam. The second pulse (marked with green color) comes out from Orpheus-N-3H and passes through a non-linear crystal, beta barium borate (BBO), which doubles the frequency (second harmonic generation). Finally, the spherical mirror reduces the beam size. The full width at half maximum (FWHM) of the beam diameter is 0.8 mm at the sample. The beam alignment of the two pulses is confirmed at different points to ensure the spatial overlap of two pulses in the sample while the temporal overlap is established by moving the delay stage.

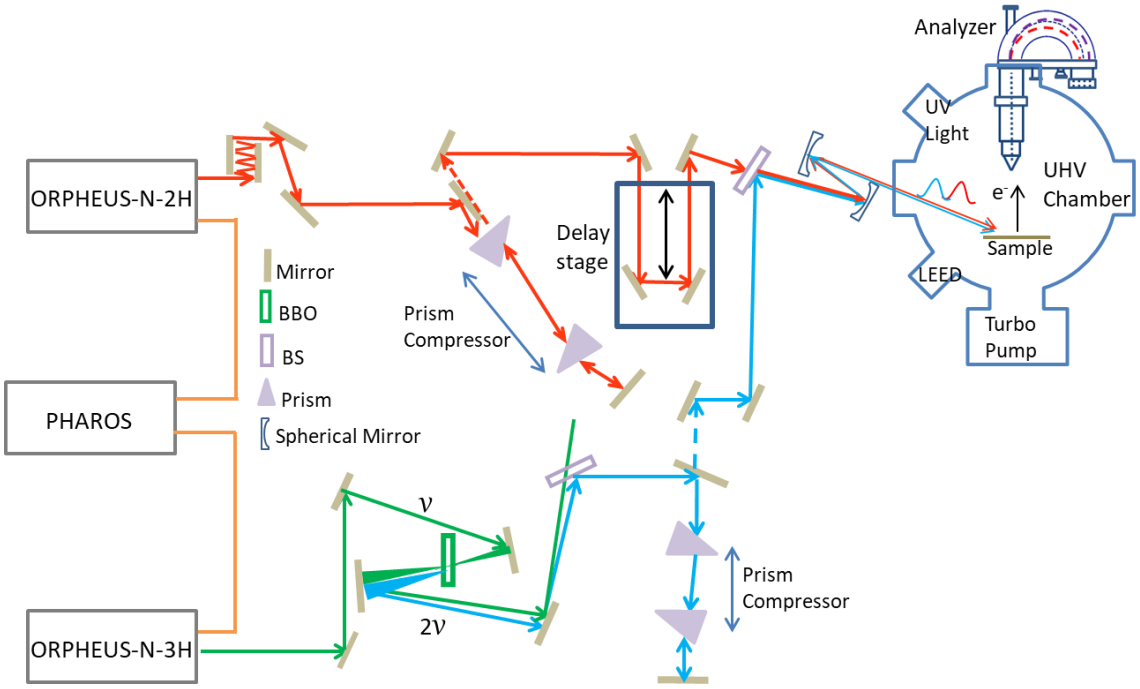

Figure 2.3: Schematic of TR-TPPE experimental set up. Two beam lines-pump line (orange) and probe line (green) are generated by ORPHEUS-N-2H and ORPHEUS-N-3H respectively. The optics are set up to maintain optical path and direct the beam towards sample. The pump passes through delay stage. The frequency of the probe line is doubled using a BBO crystal. Both beams are spatially overlapped before striking the sample in UHV chamber.

Electron Analyzer

The electron analyzer set up in our lab is PHOIBOS-100 that consists of a vacuum housing and four main internal components. Every parts are within UHV environment to avoid the loss of information of photo-emitted particles. Otherwise, they could collide with the gas particles resulting to the loss of its intrinsic information. The major internal components are labelled in Figure 2.4. They are:

- Input lens system for imaging the photoemitted particles from the sample surface
- Hemispherical analyzer (HSA) with 100 mm nominal radius for performing spectroscopic energy measurements;
- Detector assembly equipped with CCD for particle detection

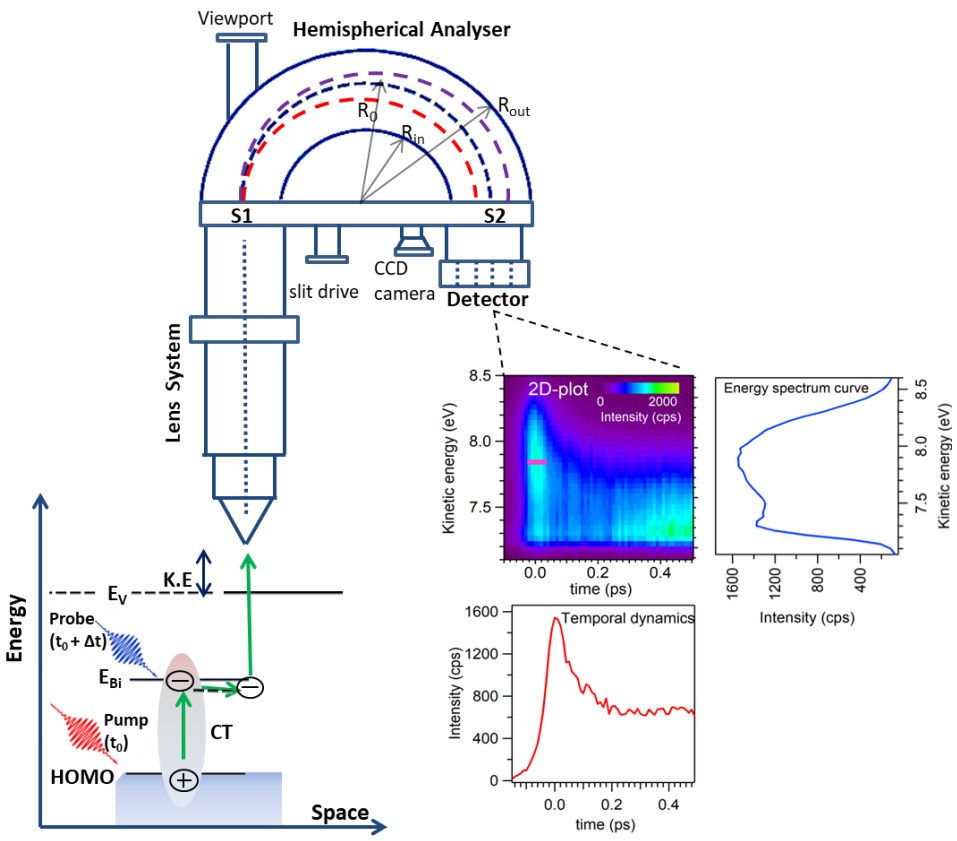

Figure 2.4: Schematic of time resolved-two photon photoemission spectroscopy technique. The pump excites electron to an unoccupied state and the probe knocks off the electron to vacuum. The detector measures population and kinetic energy of the photo-emitted electrons for subsequent times and thus a 2D plot is generated. For clarity, the figures are not in scale.

The computer software records population and kinetic energy of the photo-emitted electrons from the excited states for every temporal step of the delay stage. Thus, a 2D data can be obtained as shown in the Figure 2.4, which can be resolved to get the spectral and temporal information of the excited electrons.

Data Analysis of TPPE Spectrum

Previously, we applied TR-TPPE technique to explore hot exciton (exciton with excess

energy compared to the optical band gap) dynamics in semiconducting single walled carbon nanotube (s-SWCNT). Pump pulses of energy 1.56 and 3.76 eV, that is larger than the average band gap (E_g ~ 0.7 eV) of s-SWCNT, excited the electron. The higher pump energy was used to access higher energy states. A probe pulse of energy 4.59 eV was sent at a subsequent time to photo-ionize the electrons. The electron detector measured the population and the kinetic energy at subsequent delay times; hence, a 2D data image was obtained. The background, which is the signal contributed from the probe pulse alone, was subtracted from thus obtained 2D image. The background subtracted 2D image for pump energy 1.77 eV and 3.76 eV, and the TPPE spectra for selective probe delay times (t) are shown in Figure 2.5. Applying equation 2.4, the energy of the excited state can be determined. For convenience, the excited state energy is referenced w.r.t first discrete valence band (V_1), obtained from UPS spectrum (Figure 2.5d). In the 2D plot, the pseudo-color represents intensity of photo-emitted electrons at various energies and pump probe delay times. The 2D image gives us general information on population dynamics and energy of excited electrons. At temporal overlap of pump-probe pulse (t = 0), the excited electrons have higher energies as shown by the high-energy tail in the 2D image. It is observed that excitons closer to the band edge are populated almost instantaneously after photoexcitation but it decays quickly to lower energy states, which implies an extremely fast hot exciton relaxation. More detailed information on the spectrum can be obtained by plotting a vertical cut (a fixed probe delay time) of the 2D image. Figure 2.5c shows the spectra obtained from vertical cuts of the 2D images at 20 fs and 500 fs. At t = 20 fs, electrons with energies as high as 2 eV and 3 eV above V_1, for pump energy 1.77 eV and 3.76 eV respectively can be seen. As expected, the spectrum obtained with the 3.76 eV pump shows a broader high energy tail near time zero. The hot excitons gradually vanish with increasing delay time. At t = 500 fs, the hot exciton is relaxed and

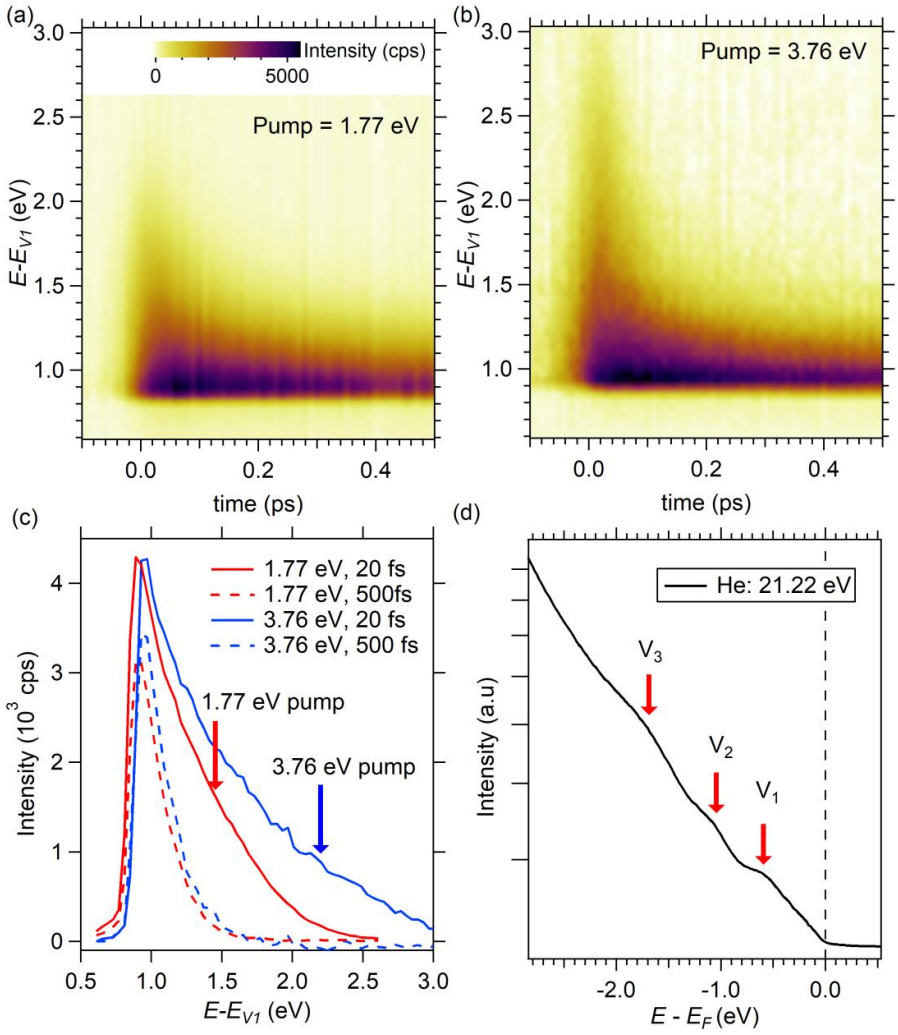

Figure 2.5: Two-dimensional image of CNT obtained from TPPE using (a) pump energy 1.77 eV and (b) 3.76 eV. (c) Vertical cut taken at selected delay times between pump and probe pulses. (d) UPS spectrum near valence band edge. "Figure reprinted with permission from reference [35].[35] Copyright (2016) American Chemical Society."

no significant change in the spectral shape is found at larger delay times for both pump energies. Likewise, the horizontal cuts (fixed energy) of the 2D image give population dynamics, which is shown in Figure 2.6. The intensity is plotted as a function of time at various electron energies obtained with pump photon energy equal to 1.77 eV. The energies in the legend are referenced

with respect to the band-edge energy E_{11} so that $E - E_{11}$ represents the excess energy of hot excitons. E_{11} is the first van Hove singularity and assumed that the valence band maximum and

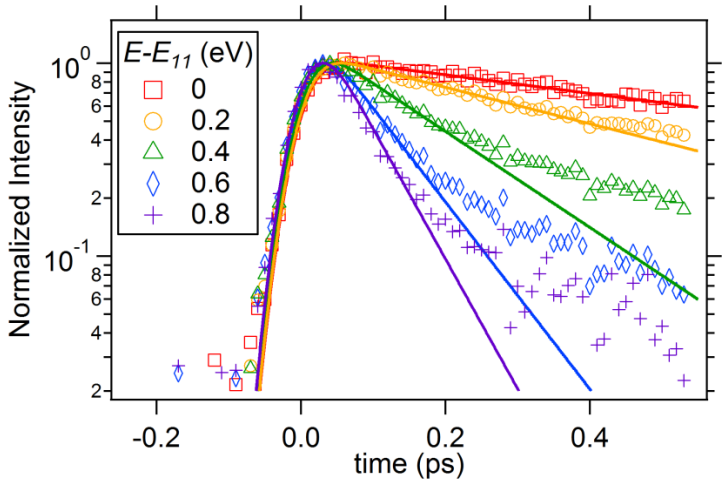

Figure 2.6: The time evolution of the photoemission intensity at various energies above the lowest exciton energy E_{11}. The pump photon energy is 1.77 eV. The curves are fitted with a single exponential function convoluted with the laser pulse. "Figures reprinted with permission from reference [35].[35] Copyright (2016) American Chemical Society."

the conduction band minimum are symmetric around $E_{11} \approx 0.7$ eV. For those curves at high energies, the overall decay is a bi-exponential and we attribute the fast decay to hot exciton relaxation. The initial fast decay rates are fitted with a single exponential function that is convoluted with the laser pulse duration using a rate equation model (solid lines in Figure 2.6).

The data illustration on single-walled carbon nanotubes shows that TR-TPPE can resolve the exciton dynamics in both the energy and time domains, which are essential for studying exciton dissociation process. The next section focusses on sample preparation and characterization techniques.

2.4 Sample Preparation and Characterization Techniques

The samples used for the study are mainly donor – acceptor bilayer films. They are either organic – organic or organic – TMD heterostructures. ZnPc, F_8ZnPc and C_{60} are the organic molecules (purity > 99%, sublimed). They were purchased from the commercial vendor. MoS_2 and WSe_2 are the semiconducting TMDs used for the study. The organic molecules are grown either on TMDs or on various other substrates such as HOPG, graphene, Au, SiO_2 or glass. Prior to growth of organic molecules, it is essential to remove any adsorbed molecules on the substrate to avoid contamination. Substrates like Si, glass, HOPG, and graphene are annealed to a sufficiently high temperature and time length in UHV environment to outgas the adsorbed molecules. For single crystal metals, sputtering-annealing cycle is employed to clean the surface. The sputtering-annealing cycle is repeated to ensure surface cleanness. The substrate is then ready for deposition.

2.4.1 Thermal Evaporation Deposition

Thermal evaporation technique is employed to deposit organic molecules on the substrate. The schematic of the thermal evaporation technique is shown in Figure 2.7. This system is equipped with three thermal evaporation sources. The base pressure of the chamber is around 10^{-9} Torr. Organic molecules in powder form is stored in boron-nitride crucibles. The thickness of the film is monitored by the quartz crystal microbalance (QCM) placed near to substrate. On heating, the molecule sublimes at its evaporation temperature, traverses the chamber as a vapor stream and hits the target substrate, sticking as a thin film uniformly over the area. This technique allows precise control on nm thick film deposition.

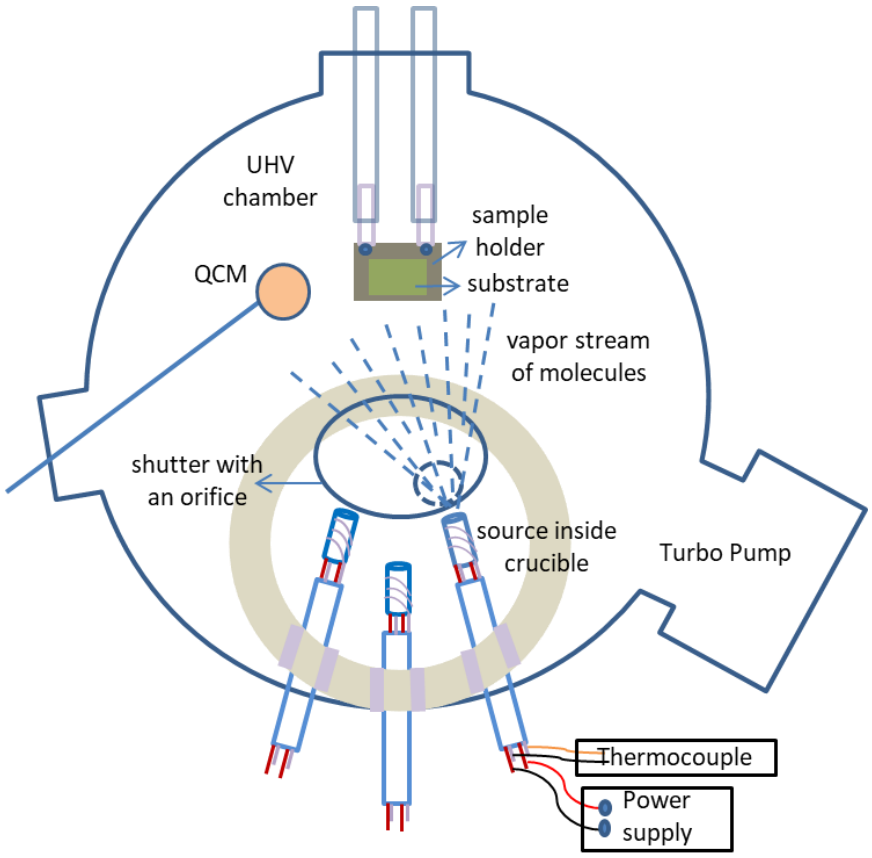

Figure 2.7: Schematic of the thermal evaporation deposition in UHV chamber. Organic molecules are stored in crucible. Heat is supplied via electric current to evaporate the molecules. The thickness of molecules deposited on substrate is measured by a quartz crystal microbalance.

2.4.2 Control of wavefunction orientation at interface

The primary objective of my thesis is to understand how wavefunction orientation of electron and hole at the interface affects exciton dissociation. Exciton dissociation will be studied mainly in two types of interfaces viz. (i) semiconducting organic – organic and (ii) semiconducting organic – TMD interfaces. Bound charge transfer excitons exist at these interfaces. The electron and hole wavefunction orientation and size will determine the fate of these excitons. The wavefunction orientation of electron and hole depends on the π-stacking direction of organic molecules, which in turn rely on the orientation of the molecules on the substrates. At the substrate-molecule interface, the two energetic interactions, substrate-molecule

($E_{S\text{-}M}$) and molecule-molecule ($E_{M\text{-}M}$) comes into play. The interplay between these two interactions determines the molecular arrangement in the initial stage of film formation.[36-37]

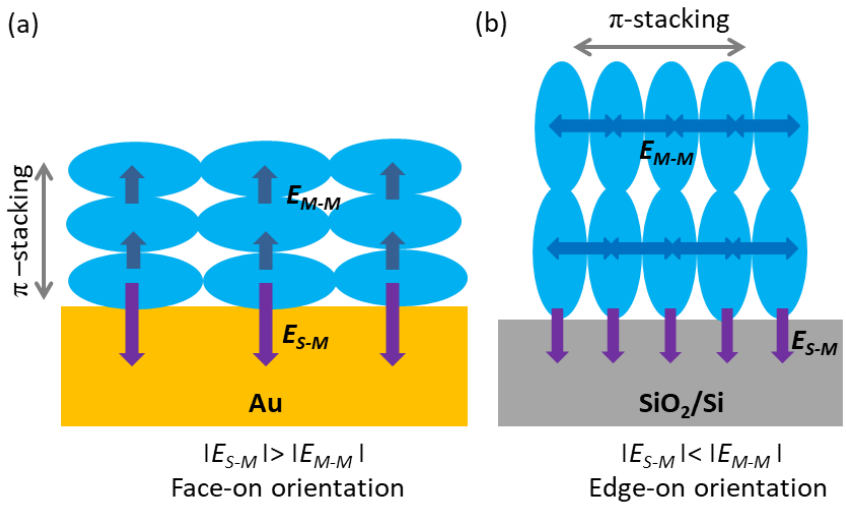

Figure 2.8: Schematic of molecular orientation (a) face-on orientation for $|E_{S\text{-}M}|>|E_{M\text{-}M}|$ and edge-on orientation for $|E_{S\text{-}M}|<|E_{M\text{-}M}|$

Molecules grow with face-on stacking if $E_{S\text{-}M}$ dominates over the $E_{M\text{-}M,}$ whereas the molecules grow with an edge-on orientation if $E_{M\text{-}M}$ is stronger than $E_{S\text{-}M.}$ For instance, for metallic substrate $E_{S\text{-}M} > E_{M\text{-}M,}$ and the molecules grow lying flat (face-on) to the substrate (Figure 2.8a)[38]. However, in SiO_2/Si substrate where $E_{S\text{-}M} < E_{M\text{-}M}$, results in edge-on orientation of the molecules (Figure 2.8b)[38]. Besides the substrate-mediated orientation, growth rate and substrate temperature are the other two controlled parameters for maintaining smooth morphology and desired orientation of the film[37]. Likewise, phthalocyanine (Pc) molecules maintain face-on orientation on TMDs. The molecular orientation can be confirmed from both the IP values measured by UPS and the diffraction pattern measured by the LEED. The results from characterization techniques will be discussed in later chapters.

Based on the molecular orientation, Figure 2.9 shows the schematic of delocalized wavefunction of electron and hole at various interfaces. For F_8ZnPc – ZnPc bilayer grown on

HOPG, both molecules have face-on orientation. Hence, the electron and hole wavefunction will be directed along the π-stacking direction, perpendicular to the interface of organic molecules (Figure 2.9a). On the other hand, in F_8ZnPc – ZnPc bilayer grown on SiO_2, the electron and hole wavefunctions will be parallel to the interface (Figure 2.9b). In the ZnPc – MoS_2 heterojunction, the hole wavefunctions is perpendicular while the electron wavefunction is parallel to the interface (Figure 2.9c). At the ZnPc – C_{60} interface grown on Au, the electron wavefunction in the acceptor is spread out in all possible directions whereas the hole wavefunction is parallel to the interface (Figure 2.9d). The spatial overlapping between the electron and hole wavefunction determines the strength of exciton binding energy. The more the overlapping of wavefunctions, the greater the binding energy is between the electron and hole. Thus, we expect faster dissociation for excitons in the system shown in Figure 2.9 (a) and (c) because the delocalized wavefunctions are least overlapped. However, in the system shown in Figure 2.9 (b) and (d), the increased overlapping between the two wavefunctions increases the CT exciton binding energy. Therefore, the exciton dissociation process can be slower.

Exciton Delocalization size

It is assumed that the larger delocalization size facilitates coherent transport and promotes exciton dissociation. Thus, it is important to quantify the delocalization size of the exciton. In our experiment, the delocalization size can be determined by varying the thickness of an acceptor layer. For example in ZnPc – C_{60} system (Figure 2.9d), we can vary C_{60} (acceptor) thickness and observe the quenching of delocalized electrons into Au. The delocalized electrons are generated via the CT from ZnPc to C_{60}. In thinner films of C_{60}, the delocalized electrons should quench quicker than in the thicker films. This allows us to determine the size of CT exciton. On the other hand, in F_8ZnPc – ZnPc on HOPG system (Figure 2.9a), dissociation of CT

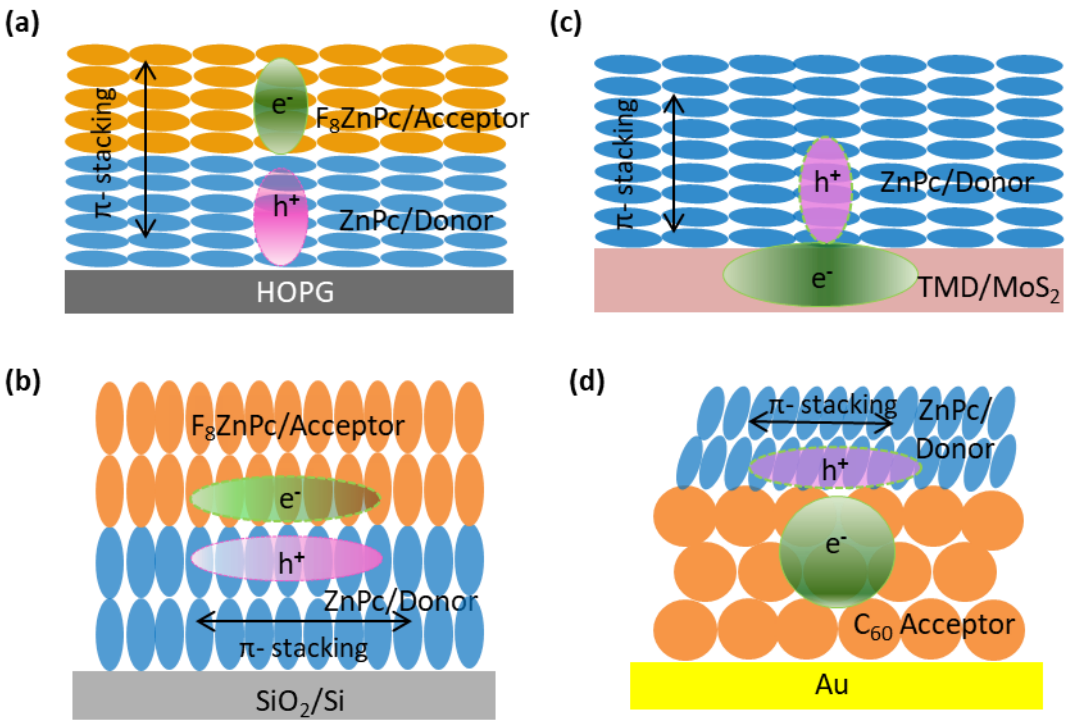

Figure 2.9: Electron and hole wavefunction orientation in (a) organic–organic heterojunction with face-on orientation (b) organic–organic heterojunction with edge-on orientation, (c) organic–TMD heterojunction with face-on of organic molecules and (d) organic–organic heterojunction for spherical orientation of acceptor and edge-on orientation of donor on top of it.

exciton can take place and the transport time for free electrons to reach the top of F_8ZnPc (acceptor) surface could be measured. Recall that the TPPE technique is surface sensitive and it can detect electrons only from the surface. Although both ZnPc and F_8ZnPc are excited in this system, free electrons are generated only in F_8ZnPc.

The next chapter will be focused on the relationship between the delocalization size, binding energy and temporal dynamics of charge transfer excitons at organic – organic interfaces. ZnPc – C_{60} on Au will be chosen as a model system and the techniques discussed above will be applied to resolve the hot and cold CT states and the delocalization size of these CT excitons.

3. Measurement of charge transfer state, delocalization size and temporal dynamics of charge transfer excitons at donor-acceptor interface

3.1 Introduction

At donor–acceptor interfaces, the charge transfer (CT) excitons often have a binding energy of ~ 0.1 – 0.5 eV, which is much larger than the thermal energy ~ 0.025 eV at room temperature. While the effective dissociation of these CT excitons is a critical process for generating photocurrent in photovoltaics and optoelectronic devices, the underlying mechanism of exciton dissociation mechanism remains unclear.[27, 39-41] Various mechanisms have been proposed to understand the charge separation at interfaces. Some recent theoretical[28, 42-46] and experimental studies[47-52] suggest that spatial delocalization of the electronic wavefunction would play a vital role in facilitating charge separation. The distance between electron and hole wavefunction in a delocalized CT exciton is large compared to that in a localized CT exciton. Hence, the exciton binding energy of delocalized CT exciton can be smaller than expected. These delocalized CT states can be populated by the CT process at the donor – acceptor interface and transition subsequently into free carriers without overcoming a large Coulomb barrier.[39] Therefore, whether effective exciton dissociation can occur at a particular interface is hinged on the presence of such delocalized and loosely-bound CT states.

In the light of the importance of exciton delocalization, an experimental method that can resolve both the spatial size and energy of CT excitons on the ultra-fast timescale is desired. Measuring the delocalization size that is less than a few nm with fs time resolution has remained a challenge. Some recent works have determined the delocalization size from quantities such as

the transient electro-absorption signal[47, 49] and the electron-hole recombination rate at extremely low temperatures.[48] Others compare the exciton dynamics in bulk heterojunctions with different compositions and fullerene aggregate sizes to estimate the delocalization size.[50] However, these techniques cannot spectrally-distinguish CT excitons with different binding energies and sizes. Because delocalized electrons and holes are not point charges, the exciton binding energy and the delocalization size do not follow a simple inverse-distance relationship.[28, 44-45] Therefore, how the exciton binding energy depends on the delocalization size and how the delocalization size evolves temporally during the relaxation of hot CT excitons are important questions that need to be addressed. We apply time-resolved two photon photoemission spectroscopy (TR-TPPE) to address these concerns.

In this work, epitaxial-grown ZnPc-C_{60} bilayer samples were used. The highly homogenous sample allows us to resolve distinct spectral features in the CT manifold at the ZnPc – C_{60} donor– acceptor interface by using the TR-TPPE method. The precise control of the C_{60} layer-thickness enables us to determine the spatial size of the CT excitons. For the ZnPc – C_{60} interface, it is found that the CT process initially populates delocalized CT states that have a delocalization size of ≈ 4 nm in the C_{60} layer. These CT excitons relax in the CT manifold to produce lower energy CT excitons (i.e., excitons with larger binding energies) with the electron density residing closer to the interface. These findings generally agree with the picture proposed by recent theoretical work.[28, 44-45]

3.2 Sample Preparation, Characterization and Method

The structure of the ZnPc–C_{60} interface used in this study is shown schematically in Figure 3.2a. Prior to deposition of organic molecules, the single crystal Au (111) surface was cleaned by standard sputtering and annealing cycles in an ultrahigh vacuum chamber (UHV) with a base

pressure < 5×10^{-10} Torr. The first complete layer of C_{60} was deposited at 300 °C. Subsequent C_{60} layers were deposited at 90 °C at a growth rate of 0.5 Å/min. At this temperature, only C_{60} molecules that were in direct contact with Au can be adsorbed on the surface. A deposition fluence above one monolayer (ML) was used to ensure a complete coverage for the first layer. Similar recipes were used previously to produce epitaxial growth of C_{60} thin films via a layer-by-layer growth mode.[53-54] Figure 3.2b is the LEED pattern for 4 nm C_{60} on Au, which shows that the C_{60} thin film is a single-crystal film. The atomic force microscope (AFM) image of the 4 nm C_{60} film is shown in Figure 3.1c. The surface is smooth, and steps from the C_{60} terraces (triangular-shaped features) can be identified. The height profiles along line 1 – line 5 on the image is plotted in Figure 3.2d. Profiles 1 and 2 show a step height of ~ 0.8 nm, which corresponds to the height of a single C_{60} layer. Profiles 3 – 5 show a step height of ~ 0.2 – 0.3 nm, which corresponds to the step height of the underlying vicinal Au surface. This indicates that C_{60} molecules form a conformal film on Au with a uniform thickness. Then ZnPc molecules were deposited on top of the C_{60} layer at a growth rate of (0.8 – 1.0) Å/min. Figure 3.2e shows the AFM image of a 1 nm ZnPc film deposited on 4 nm C_{60}. The rectangular ZnPc islands align with the crystallographic direction of the C_{60} surface, which forms the triangular pattern. Hence, ZnPc molecules grow epitaxially on the C_{60} single crystal. The measured step height of the ZnPc layer is around 1.3 – 1.4 nm,[55] indicating that the molecules have an edge-on orientation. This molecular orientation agrees with previous studies on the CuPc – C_{60} interface.[56-58] The molecular orientation can be further confirmed from the ionization potential (IP). Typically, the IP for molecules with a face-on orientation is ≈ 0.5 eV larger than that for molecules with an edge-on orientation.[59-60] For the ZnPc molecules, IP is ~ 4.8 eV ~ 5.25 eV respectively for edge-on and face- on orientation respectively.[59, 61] The IP value of the ZnPc layer measured by our

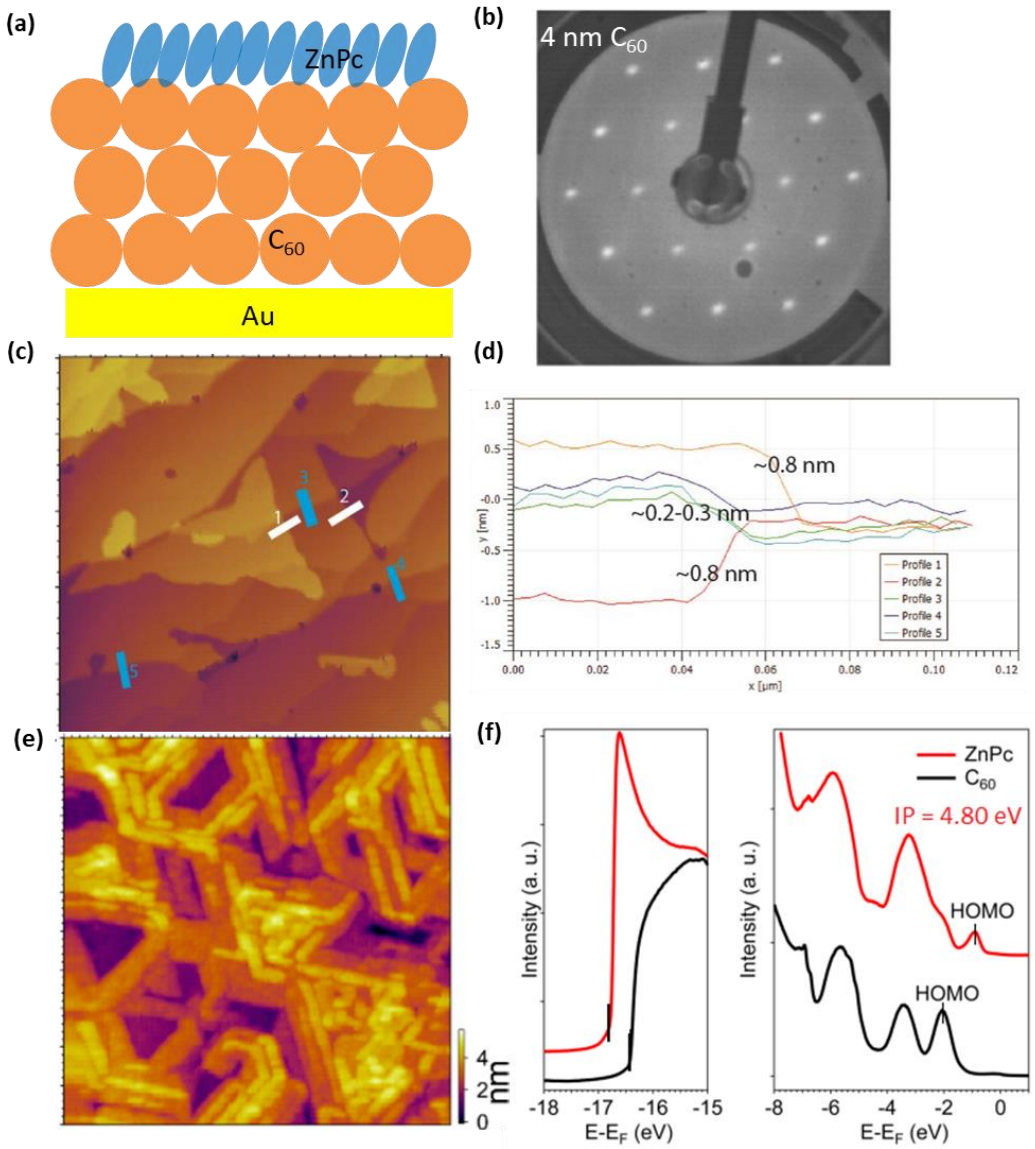

Figure 3.1: (a) Schematic of the ZnPc – C_{60} film deposited on Au (111) crystal. ZnPc molecules grown on C_{60} has edge-on orientation. (b) LEED image of 4 nm C_{60} on Au shows that C_{60} molecules form a single crystal. (c) AFM image of 4 nm C_{60}. (d) The plot of height profiles along line 1 – line 5 indicated on (c). (e) AFM image of 1 nm ZnPc on 4 nm C_{60} sample. (f) UPS spectra of 4 nm C_{60} (black trace) and 1 nm ZnPc on 4 nm C_{60} (red trace) near SECO region (left) and HOMO region (right) collected with He I = 21.22 eV. The HOMO positions are marked with vertical bars. The calculated ZnPc's IP value is 4.80 eV in agreement with edge-on orientation.

UPS (He I = 21.22 eV) is 4.8 eV, which further supports that ZnPc molecules have an edge-on orientation on C_{60}.[59, 62]

After the deposition, the sample was transferred to the main chamber with a base pressure $< 1 \times 10^{-10}$ Torr, where TR-TPPE and UPS experiments were performed. In the TR-TPPE experiment, the pump laser pulse, with photon energy centered at 1.77 eV (~ 25 fs), excited the sample. Note that the optical resonance (S_1 state) of ZnPc is at 1.77 eV. This energy resonantly excited the S_1 state of the ZnPc film, but the energy was too low to excite the C_{60} layer (optical band gap ~ 2.6 eV). Then, the photoexcited electrons were ionized by a probe beam with photon energy of 4.68 eV (~ 60 fs). The details of TR-TPPE set-up can be found in section 2.3 of Chapter 2. The laser fluence was low enough to avoid exciton–exciton interaction processes as evidenced from the previous study in our lab[63] and the dynamics was independent of the pump fluence[55]. The probe photon energy was varied to ensure that peaks in the spectra correspond to intermediate states induced by the pump pulses. The UPS experiment was done with a standard UV lamp of photon energy equal to 21.22 eV.

3.3. Experimental results and discussions

Before discussing the results, we would like to highlight two major advantages provided by TR-TPPE method. First, multiple CT states at an organic – organic interface can be resolved spectrally. Second, by subtracting the CT state energies from the LUMO energy (2.60 eV) of C_{60} reported in inverse photoemission spectroscopy studies,[64] we can estimate CT exciton binding energies. In the model system ZnPc – C_{60} on Au, a 4 nm C_{60} film corresponds to 5 monolayers (ML) of C_{60} molecules (0.8 nm/ML). We note that the spectrum remains essentially the same with a further increase in the C_{60} thickness. Hence, the result shown in Figure 3.2 represents the "bulk C_{60}" regime in which the C_{60} layer is thick enough so that the dynamics is not affected by the substrate or the confinement in the C_{60} thickness. Moreover, the ZnPc molecules have an edge-on orientation and the π-stacking direction is parallel to the surface. In this orientation, the

interaction along the surface normal direction is weak in the ZnPc film. Hence, the dynamics at the ZnPc – C_{60} interface observed with the 1 nm-thick (≈ 1 ML) ZnPc layer should be representative to the interface formed with a thicker ZnPc layer. In addition, the photoemission probe is surface sensitive.

3.3.1 Spectral resolution of hot and cold CT states

Figure 3.2a and b shows the TR-TPPE spectrum of a 1 nm ZnPc – 4 nm C_{60} on Au (111). The pseudocolor represents the TPPE intensity, which is resolved as a function of time (*x*-axis) and energy (*y*-axis). For convenience, the energy is referenced with respect to the ZnPc's HOMO i.e., 0 eV in the energy level corresponds to the ZnPc's HOMO. CT states with different binding energies (CT_h, CT_2, and CT_1 in Figures 3.2a and 3.2b) populated by the CT process are resolved spectrally in the TR-TPPE spectrum.

First, we observed the most intense feature at an energy ≈ 1.6 – 1.7 eV above the ZnPc's HOMO. This feature is short-lived (lifetime ≈ 150 fs) and its energy agrees well with the lowest optical absorption peak (≈ 1.7 – 1.8 eV) of ZnPc crystals.[65] Hence, we assign it to the singlet (S_1) state of ZnPc. The loss in the intensity is attributed to charge transfer from ZnPc to C_{60}. Peaks at lower energies appear at longer delay times (Figure 3.2b), we assign them to CT states (CT_1 and CT_2). Since CT_1 and CT_2 are lower in energy and long –lived, we also refer them as cold CT states. The CT_1 and CT_2 states are only apparent in samples with a 1 ML thick ZnPc, They disappear in films with a thicker ZnPc layer (see next section), which suggests that CT states are originated farther away from the surface, presumably in the C_{60}. layer. The intensities of the CT_1 and CT_2 states rise in a few ps after photoexcitation (Figure. 3.2b). This ps-intensity rise is attributed to the localization of CT excitons at the ZnPc – C_{60} interface. Note that the TPPE technique is surface sensitive because ionized electrons have a very limited escape depth

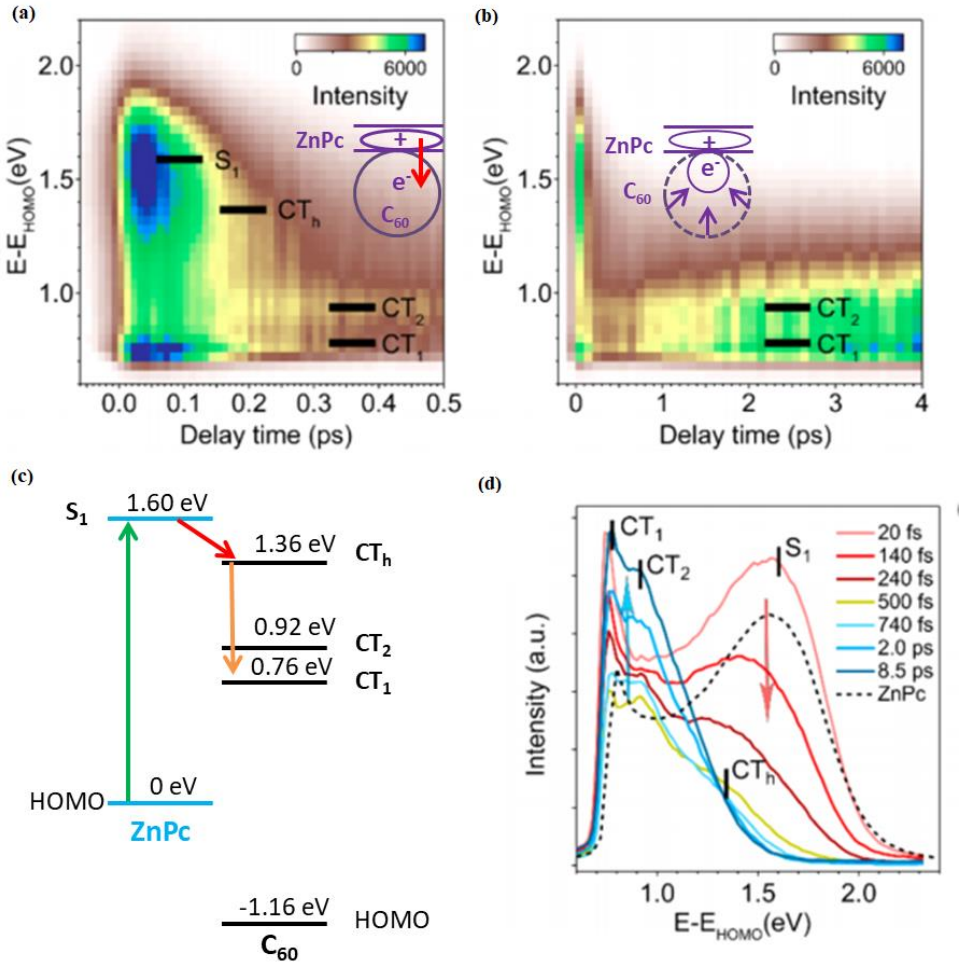

Figure 3.2: (a) and (b) shows the TR-TPPE spectrum of 1 nm ZnPc – 4 nmC_{60} on Au at two different time scales. CT states with different energies are resolved. The diagrammatic sketch in the inset of (a) represents the delocalization of electron wavefunction in the inital time after photoexcitation but it localizes within 2 ps as shown in the inset of (b). (c) The energy level diagram of the ZnPc – C_{60} interface. After photoexcitation (green arrow), charge transfer (red arrow) from ZnPc-S_1 to the CT_h state occurs. The orange arrow indicates the relaxation of CT_h state to the lower CT_1 and CT_2 states. (d) The TR-TPPE spectra at selected probe delay times as indicated in the legend. The intensity of CT_1 and CT_2 increases with time. The black dashed line is the spectrum for the 10 nm ZnPc flilm at $t = 0$ ps.

(a few nm).[55, 66-67] Hence, the localization of CT excitons, which draws the electron wavefunction closer to the surface (inset in Figure. 3.2b), can increase the overall TPPE signal. While the TPPE spectrum in Figure 3.2a-b shows that the decay of the S_1 state is followed by the build-up of the CT_1 and CT_2 intensity, the decay time of the S_1 state (≈ 150 fs) does not match with the rise time (a few ps) of the CT_1 and CT_2 states. A careful inspection of the spectrum in

Figure 3.2a shows a weak shoulder is emerged at an energy ≈ 1.3 – 1.4 eV and at times from few hundreds of fs to a few ps. This feature is labelled as the CT_h state. It bridges the two aforementioned timescales. Its kinetics will be analyzed in the next paragraph to support this fact. To further understand the charge transfer process from ZnPc to C_{60}, the TR-TPPE spectra at various pump-probe delay times are plotted in Figure 3.2d accompanied by the energy level diagram to its left (Figure 3.2c). The three red lines, from the light to the dark color, are spectra taken at t = 20 fs, 140 fs, and 240 fs respectively. The spectrum at t = 20 fs (pink line) is similar to the spectrum obtained from the thick (10 nm) ZnPc film (black dashed line), which indicates that the ZnPc's S_1 is the primary excitation found right after photoexcitation. Compared with the ZnPc spectrum (black), additional intensities can be found in the ZnPc – C_{60} spectrum (pink) at energies below 1 eV. This additional intensity component is attributed to optically-excited CT excitons. The S_1 state decays in the first few hundreds of fs after excitation (the red arrow). Then, a set of peaks emerge at lower energies. At t = 500 fs (yellow line), two peaks at 0.76 eV (CT_1) and 0.92 eV (CT_2), and a shoulder at 1.36 eV (CT_h) can be identified. Around this delay time, the total intensity of the spectrum reaches a local minimum. At longer delay times, the CT_h shoulder diminishes while the CT_1 and CT_2 peaks increase in intensity. This is shown by the series of blue spectra, from the light to the dark color, obtained at t = 0.74, 2.0 and 8.5 ps respectively. We will refer to the CT_h feature as the hot CT states due to its short lifetime and high energy as compared to the CT_2 and CT_1 states. The energy level diagram in Figure 3.2c summarizes all these assigned states, together with the HOMO of the ZnPc and C_{60} obtained from UPS.

To verify the time gap between the S_1 decay and rise of CT_1 and CT_2 states, the decay kinetics of CT_h shoulder is analyzed. The inset in Figure 3.3a compares the spectral shape of the spectra at t = 0.6 ps, 20 ps and 100 ps by normalizing the intensity near the CT_1 and CT_2 peaks.

Beyond t = 20 ps, the spectral shape remains similar and only a decrease in the overall intensity is observed. At t = 0.6 ps, an additional shoulder is visible in the spectrum at ≈ 1.3 – 1.4 eV. The shoulder diminishes gradually in a period of few ps (see Figure 3.2d). To isolate this shoulder, the raw spectrum at 0.6 ps is subtracted by the re-scaled spectrum at a longer delay time, i.e. the 20 ps spectrum shown in the inset of Figure 3.3a. The same procedure is used to subtract spectra at other delay times. Thus subtracted 2D plot of TR-TPPE spectrum is shown in Figure 3.3a. The residual intensity represents how the spectra at different times deviate from the spectral shape of the relaxed CT_1 and CT_2 states. Note that we have not performed a global fitting to the data because the spectral shape for an individual state (e.g. S_1 state in Figure 3.2a) changes continuously in early delay times via processes such as intraband relaxation and reorganization. This continuous change in the spectral shape is commonly observed in TR-TPPE spectra[68-71] because the technique is sensitive to the excess energy possessed by hot excited states. Moreover, the hot CT states are a manifold of states instead of a single discrete state. Both of these factors preclude an unambiguous global analysis.

In the first few hundreds of fs, the residual intensity is dominated by the S_1 state. The peak position decreases as a function of time (open circles) primarily because of the intensity decay of the higher energy S_1 state. Beyond 0.5 ps, the peak position remains steady at ≈ 1.36 eV, which is labelled as the CT_h state. The CT_h state is different from the S_1 state in the ZnPc film because it has lower energy peak. For reference, a black dashed line indicates the energetic position of the S1 peak. For t > 0.5 ps, the spectral shape of the CT_h state in the residual spectrum remains similar while its intensity decreases as the delay time increases.

Figure 3.3b shows the kinetics of the integrated intensity of the residual spectrum shown in Figure 3.3a. The data is fitted by a bi-exponential decay function (red line). The two time

constants obtained are 0.15 ps and 2.2 ps. The fast decay component is assigned to the transition from the S_1 to the CT_h state. Because the CT_h state is located farther away from the surface (see

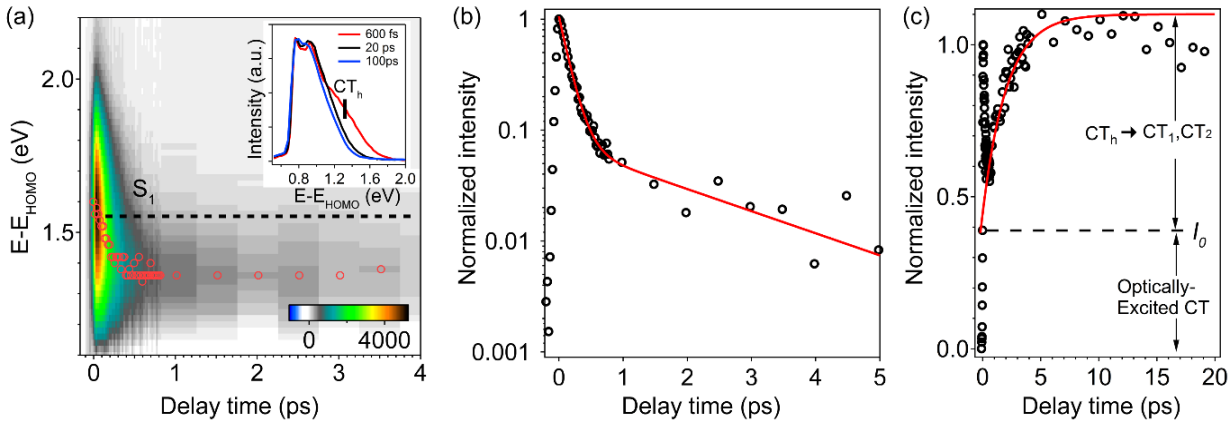

Figure 3.3: (a) Pseudocolor representation of the subtracted TR-TPPE spectrum of the 1 nm-ZnPc – 4 nm-C_{60} film in which the spectral components from the CT_1 and CT_2 states are removed. The dashed line represents the position of the S_1 state. The open circles represent the peak positions, which are located below the S_1 state at large delay times because of the S_1 → CT_h transition. The inset shows the normalized spectra at t = 0.6, 20 and 100 ps. (b) The kinetics of the integrated intensity of the peak shown in (a). The red line is a fit to a bi-exponential decay function. (c) The kinetics of the intensity from a spectral range that includes the CT_1 and CT_2 states for the 1 nm- ZnPc – 4 nm-C_{60} sample. "Figure reproduced with permission from reference [55].[55] Copyright (2017) American Chemical Society."

inset of Figure 3.2a), the photoemission probe is less sensitive to the CT_h state. The slower decay time constant (2.2 ps), which corresponds to the diminishing of the CT_h shoulder, is assigned to the intensity decay of the CT_h state via the relaxation to the lower energy CT_1 and CT_2 states.The CT_h → CT_1/CT_2 transition can be verified independently by analyzing the CT_1 and CT_2 peak intensities as a function of time. The temporal evolution of the integrated intensity over the spectral range (0.68 – 1.0 eV, see Figure 3.2b, d) that encompasses the CT_1 and CT_2 states is shown in Figure 3.3c. The initial intensity spike near time zero is due to the spectrum overlapping with the S_1 state, which decays within the 100-fs timescale. Then, the intensity rises on the ps timescale. Neglecting the initial spike, the rise time of the signal can be determined by a simple exponential fit. The rise-time obtained from the fit is 2.1 ps, which agrees well with the

decay time of the CT_h shoulder (2.2 ps). A constant intensity offset (I_0 in Figure 3.3c) is added to the exponential term in order to fit the data probably. This offset can be attributed to optically-excited CT_1 or CT_2 states, which are populated promptly after photoexcitation.

Results from thicker ZnPc films and C_{60} standalone

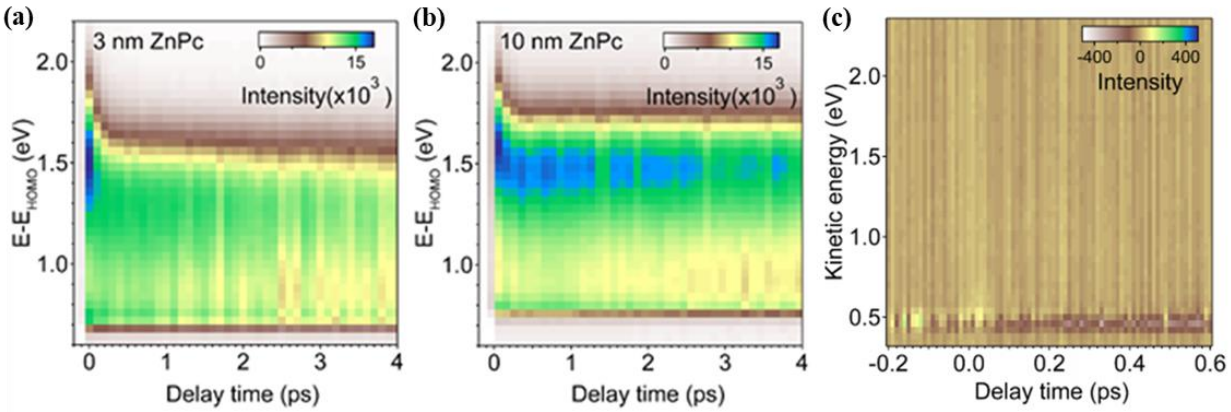

Figure 3.4: TR-TPPE spectra of (a) 3 nm ZnPc and (b) 10 nm ZnPc on 5 nm C_{60} film. (c) TR-TPPE spectra of standalone 4 nm C_{60} film on Au. "Figures adapted with permission from reference [55].[55] Copyright (2017) American Chemical Society."

Figure 3.4 (a) and (b) are TR-TPPE spectra of 3 nm and 10 nm ZnPc respectively on a fixed 5 nm C_{60} film. Unlike the quenching of the S_1 state originated from CT and the rising of the CT_1 and CT_2's intensities observed in 1 nm ZnPc film (see Figure 3.2 a and b), the S_1 state for 3 nm ZnPc has a much longer lifetime and the pair of CT states are not visible. Furthermore, the spectrum in (a) is similar to the spectrum in (b) that is obtained from a 10 nm-ZnPc sample. Because photoemission is a surface sensitive technique, it is less sensitive to the buried interface features as the ZnPc layer becomes thicker. Therefore, these results confirm that the dynamics observed in Figure 3.2 is originated from the interface. The disappearance of a clear CT_1 and CT_2 peaks in the 3 nm-ZnPc spectrum is consistent to their assignment of CT excitons. This is because the electron in these CT exciton is located in the underneath C_{60} layer, which results in a weaker photoemission signal. The longer lifetime of S_1 state (order of ps) in the 3 nm ZnPc

sample compared to 1 nm ZnPc sample (150 fs) indicates that S_1 excitons in the top of the 3 nm ZnPc layer do not participate directly in the charge transfer. This is consistent to the weak inter-layer coupling in the ZnPc crystal with an edge-on orientation. However, the S_1 excitons in the top ZnPc layer can diffuse to the bottom ZnPc layer via slow incoherent hopping (on the ps timescale). The excitons will then be quenched at the ZnPc – C_{60} interface via charge transfer to C_{60}. The longer diffusion length in the 10 nm-ZnPc sample than that in the 3 nm-ZnPc sample explains the even longer S_1 lifetime found in the 10 nm sample.

The TR-TPPE spectra of standalone 4 nm C_{60} film on Au is shown in Figure 3.4c. Controlled measurement was performed. No pump-induced signal was observed in the spectrum. This is expected because the 1.77 eV pump energy is smaller than the C_{60} bandgap. Therefore, the result confirms that the CT_1 and CT_2 peaks observed in ZnPc – C_{60} is originated from the bilayer sample, but not from the optical excitation of the C_{60} thin film.

Here is a summary of the above-discussed observations. CT from ZnPc to C_{60} in the first few hundreds of fs populates a delocalized CT state (CT_h) that has the electron density in C_{60} locating farther away from surface (Figure 3.2a). Since photoemission is a surface sensitive technique, this CT process causes a drop in the total photoemission intensity. This agrees with the result shown in Figure 3.2b, in which the overall intensity reaches a minimum at $t \approx 500$ fs. Then the decay of the CT_h shoulder occurs within a few ps, that coincides with the rise time of the CT_1 and CT_2's intensity. We propose that these lower energies CT_1 and CT_2 states are more localized states locating closer to the interface (inset of Figure 3.2b). The CT_h populates the cold CT states, CT_1 and CT_2 states, via energy relaxation. The localization process draws the electron density closer to the surface, which causes the reemerging of the overall photoemission intensity.

Thus, TR-TPPE technique enabled us to spectrally resolve the hot and cold CT states at donor – acceptor interfaces.

3.3.2 Determination of hot CT exciton delocalization size

Delocalization size of CT excitons is determined by measuring the CT kinetics for different thicknesses of C_{60} layer. We expect a change in the CT exciton dynamics when C_{60} thickness is varied. For instance, if the C_{60} thickness is lesser than the delocalization size of the CT_h exciton, the electron in the CT_h exciton can transfer to the Au substrate in an ultrafast timescale. This will quench the CT_h population before the CT_1 and CT_2 states are populated. The temporal-evolution of the integrated intensity covering the spectral range of the CT_1 and CT_2 states for samples with different C_{60} thicknesses is plotted in Figure. 3.5a. Earlier, we have shown that the intensity rise of the CT_1 and CT_2 states in ~ 2 ps is attributed to the $CT_h \rightarrow CT_1/CT_2$ transition (Figure 3.2b). For C_{60} thickness > 4 nm, the dynamics is independent of the C_{60} film thickness. This can be attributed to the ~ 2 ps rise dynamics for all thicker films via spatial localization of the CT_h excitons to populate cold CT states in all thicker films (Figure 3.5b, top). However, when the C_{60} thickness is < 4 nm, the 2 ps intensity-rise component diminishes as the C_{60} thickness decreases. This can be attributed to the larger CT_h delocalization size than the C_{60} film If the electron delocalization size is bigger than the C_{60} thickness, the electron in the delocalized CT_h exciton can transfer directly to Au (Figure 3.5b, bottom). This annihilates the CT_h exciton prior to the $CT_h \rightarrow CT_1/CT_2$ relaxation. As a result, CT_1/CT_2 excitons cannot be formed from the relaxation of the hot CT_h exciton, which leads to the vanishing of the ps-rise component. Since the ps-rise component begins to diminish for thicknesses < 4 nm, the size of the delocalized CT_h exciton in ZnPc – C_{60} system should be ≈ 4 nm.

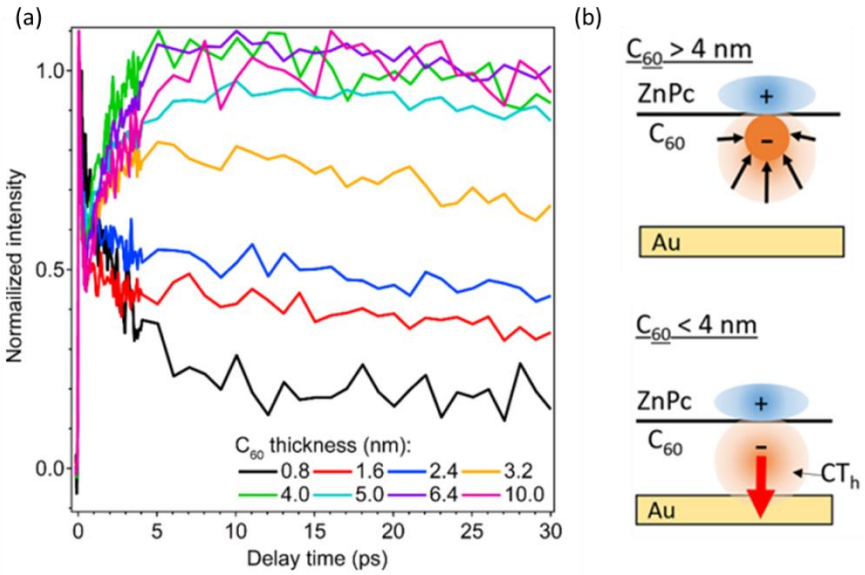

Figure 3.5: (a) The total intensity of the CT_1 and CT_2 states as a function of time for different C_{60} thicknesses. (b) Schematics show that with a thin C_{60} layer (bottom), the electron in the CT_h state can transfer directly to Au. For a thick C_{60} layer (top), relaxation of the CT_h state to more localized CT_1 and CT_2 states can occur. "Figures adapted from reference [72].[72] Copyright (2018) Institute of Physics Publishing."

3.3.3 Comparison of Cold CT excitons (CT_1 and CT_2) dynamics and delocalization size

Earlier we discussed that the hot CT_h state populated by the CT process relaxes into a combination of cold CT states, CT_1 and CT_2 states, with larger exciton binding energies. The cold CT excitons are comparatively long-lived. In order to investigate the cold CT exciton dynamics, the TR-TPPE spectra for samples with different C_{60} thicknesses are plotted in Figure 3.6 at a longer timescale up to 300 ps. For C_{60} thickness $\geq$ 4 nm, the decay dynamics of CT_1 and CT_2 states is independent of the film thickness. In these relatively thick samples, both the CT_1 and CT_2 states show a similar decay rate (Figure 3.6 e, f). Interestingly, the CT_2 state coexists with the lower energy CT_1 state instead of being converted into the CT_1 state. Because of the relative strong electronic coupling between C_{60} molecules in these pi-conjugated crystals, we propose that the CT_1 and CT_2 states can be interconverted from each other and the CT_1 and CT_2 populations maintain a dynamic equilibrium at the interface.

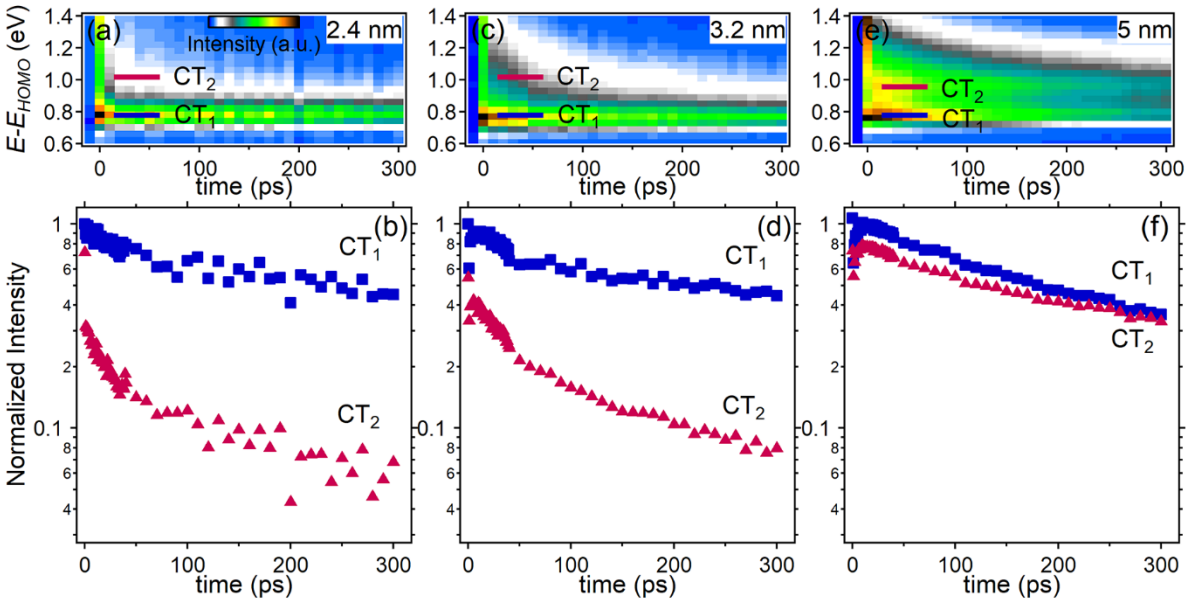

Figure 3.6: The TR-TPPE spectra for the 1 nm-ZnPc/*x* nm-C_{60}/Au(111) samples - (a) *x* = 2.4, (c) *x* = 3.2, and (e) *x* = 5. (b), (d), and (f) The temporal evolution of the photoemission intensity of the CT_1 and CT_2 states. The intensity is normalized by the intensity of the CT_1 state at *t* = 0. "Figure adapted from reference [72].[72] Copyright (2018) Institute of Physics Publishing."

This equilibrium is disturbed when the C_{60} thickness is reduced to 3.2 nm. As seen in Figure 3.6c, the CT_2 state becomes less apparent in the spectrum at larger delay times (> 50 ps). The temporal evolution of intensities of the CT_1 and CT_2 states (normalized by the intensity of the CT_1 state at *t* = 0) are shown in Figure 3.6d. The CT_2 state has a faster population decay rate as compared to the CT_1 state. The CT_2 population is likely to be quenched by the Au substrate, which implies that the CT_2 exciton is more delocalized than the CT_1 exciton. The quenching of the CT_2 state is on the 10–100 ps timescale, which is an order of magnitude slower than the quenching of the CT_h state discussed in section 3.3.1. Because the CT_1 state is lower in energy (i.e., increased binding energy), the CT_1 exciton can be trapped in thinner film regions. They cannot convert back to the CT_2 state because of the spatial confinement. The CT_2 excitons cannot

exist at these thinner regions because of its comparatively larger exciton size. The above scenario is consistent with the experimental result, which shows that the decay of the CT_2 population

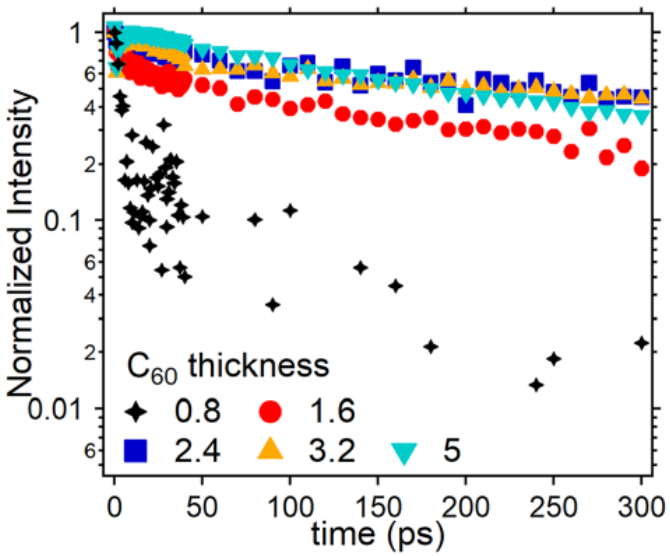

Figure 3.7: The intensity decay of the CT_1 state for the 1 nm-ZnPc/*x* nm-C_{60}/Au (1 1 1) samples. The thickness of the C_{60} layer, *x*, is indicated in the figure legend. "Figure adapted from reference [72].[72] Copyright (2018) Institute of Physics Publishing."

becomes faster, but the decay dynamics of the CT_1 population is essentially unchanged as the C_{60} thickness is decreased. For the C_{60} thickness equal to 2.4 nm, the CT_2 state is barely visible (Figure 3.6a and b) because the CT_2 excitons are more likely to be quenched by Au.

The delocalization size of the CT_1 exciton appears to be smaller than that of the CT_2 exciton. Figure 3.7 compares the intensity decay of the CT_1 peak for samples with different C_{60} thicknesses. No significant change in the decay rate is observed until the C_{60} thickness reaches 0.8 nm, i.e. 1 ML of C_{60} molecules. This indicates that the electron in a CT_1 exciton is localized within a single layer of C_{60} molecules with the exciton size ~ 0.8 nm. Overall, our result shows that delocalized CT excitons (CT_2) coexist with localized CT excitons (CT_1) even after the cooling of hot CT states. This is in contrast to the common assumption that only the

lowest energy CT exciton will remain after the hot CT exciton relaxation. The localized size of CT_1 and CT_2 exciton is determined to be ~ 0.8 nm and ~ 2.4 nm respectively.

3.3.4 Hot delocalized CT exciton promotes charge transfer

In previous section, we determined the delocalization size of CT_h exciton. Here, we will investigate its effect on the initial CT rate using thin C_{60} films (≤ 2.4 nm). By decreasing the C_{60} thickness, we spatially confine the CT_h delocalization size and measure the S_1 decay rate. The decay rate of S_1 state in ZnPc should correspond to the CT rate. Figure 3.4a-c shows the TR-TPPE spectra collected from 1 nm-ZnPc – x-nm C_{60} samples (x = 0.8, 1.6, and 2.4). For these C_{60} thicknesses, the CT state has a relatively sharp peak (located at ~ 0.8 eV; i.e. energy of the CT_1 state) because more delocalized CT excitons (CT_h and CT_2) are quenched by the Au substrate (see previous section). To determine the initial CT rate from ZnPc to C_{60}, we plot the temporal evolution of the intensity at energies around 1.6 eV (i.e., the spectral range of the ZnPc-S_1 state). Charge transfer from ZnPc to C_{60} decreases the population of the ZnPc-S_1 state and the signal decay rate represents the CT rate. The intensity evolution is shown in Figure 3.5d. Interestingly, the signal decays at a slower rate for samples with a thinner C_{60} layer. In particular, for the sample with a 1 ML-thick C_{60} (~ 0.8 nm) film, a residue S_1 peak can be observed even up to a few ps (Figure 3.5a). The residue S_1 peak is at an energy slightly lower than that of the S_1 peak at t ~ 0, which can be caused by exciton relaxation[71] or trapping. [70] For C_{60} thickness ≥ 2.4 nm, the dynamics is independent of the thickness. The dotted line shows the result for 10 nm C_{60} film, which is similar to 2.4 nm thick (blue trace). The longer S_1 lifetime found in the sample with a thinner C_{60} layer is counterintuitive. For a ML-thick C_{60} layer, one would argue that the state represented by the S_1 peak in Figure 3.8(a) is originated from a hybridization between the

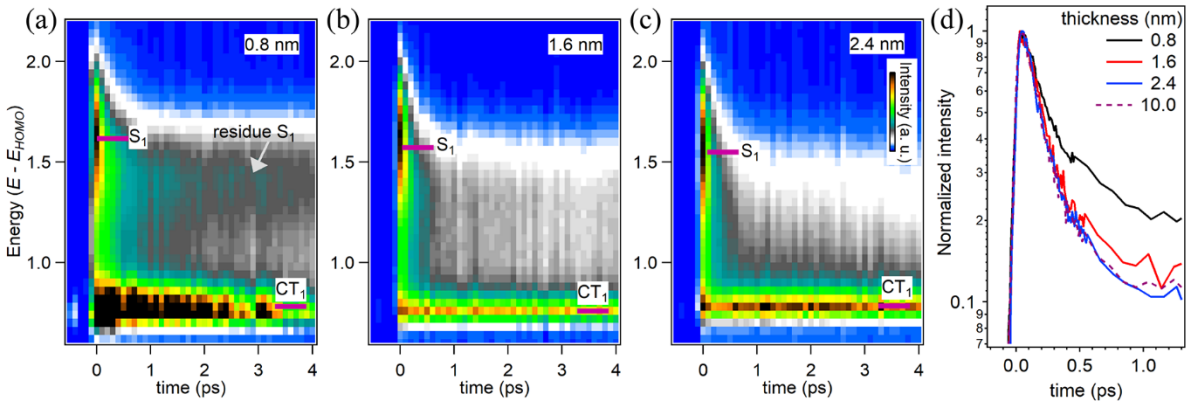

Figure 3.8: The TR-TPPE spectra for the 1 nm-ZnPc/*x* nm-C_{60}/Au(111) samples: (a) *x* = 0.8, (b) *x* = 1.6, and (c) *x* = 2.4. (d) The temporal evolution of the photoemission intensity around the ZnPc-S_1 state shown in (a)-(c) and the dotted line is for 2 nm ZnPc/10 nm C_{60}. "Figure adapted from reference [72].[72] Copyright (2018) Institute of Physics Publishing."

molecular state and the Au unoccupied states instead of a pure ZnPc's S_1 state. However, these mixed-states at metal-molecule interfaces often have lifetimes on the order of 100 fs.[54, 73-74] More importantly, if such hybridization exists, the lifetime should increase as C_{60} film thickness increases. Therefore, state-mixing cannot explain the increase in lifetime and the persistent S_1 population (the residue S_1 in Figure 3.8a).

One explanation is: The CT rate can slow down if one limits the availability of the high-energy CT states. Theoretical works propose that the initial CT first populates hot delocalized CT_h states because these states generally have smaller binding energies and are in resonance with the S_1 state.[28, 75] In the ML thick C_{60} film, with the absence of CT_h states that have energies close to the S_1 energy level, it can be expected that the initial CT will be slowed down. Similar slowing down in the CT process has been recently observed in bulk heterostructures with extremely small aggregate sizes[76]. Thus, the slower decay rate of ZnPc's S_1 in thinner C_{60} samples (smaller CT_h excton size) suggests the slower CT rate. This result demonstrates that not only delocalized CT states are first populated upon interfacial CT, they would also facilitate the CT across the interface.

3.4 Summary

The TR-TPPE techniques allow us to follow a series of interfacial electron transport processes that occur at organic semiconductor interfaces after photoexcitation. These processes include the CT across the donor–acceptor interface, the hot CT exciton formation and spatial localization of these excitons. In particular, this technique allows us to resolve the temporal evolution of the energy and coherent size of the interfacial CT exciton, which provides the long-sought information for understanding the exciton dissociation mechanism at organic interfaces. At the ZnPc – C_{60} interface where ZnPc has an edge-on orientation on top of C_{60}, we find that the hot CT exciton populated by the CT has an initial delocalization size of ~ 4 nm. The hot CT exciton facilitates the CT across the ZnPc–C_{60} interface. Then, it relaxes into lower energies CT states in ~ 2 ps. The cold CT excitons are not strictly localized, but they are an equilibration of both localized and delocalized CT states. This equilibration shifts towards the localized CT state as we spatially confine the CT exciton by decreasing the thickness of the C_{60} layer.

The results from the ZnPc-C_{60} interface shows that the hot CT_h state relaxes to the bound ones (CT_1 and CT_2) in ~ 2 ps, which makes electron extraction from the hot CT_h state very difficult if not impossible in practical devices. However, is this kind of hot to cold relaxation mechanism universal? In particular, organic crystals often have highly anisotropic structures. In the next chapter, we will discuss how the electron-hole wave function orientation resulting from the face-on orientation of the molecules results to a very different CT exciton dynamics compared to this edge-on orientation. Excitingly, we find that the reverse reaction direction, the conversion from the cold to hot CT excitons can occur on the few ps timescale.

4. Electron and Hole Wavefunction Orientation Dependence Charge Transfer Exciton Dynamics at Organic – Organic Interface

4.1 Introduction

The ultimate process for the functioning of donor–acceptor OPV devices is generation of free charge carriers. These free charge carriers are generated from CT exciton, an electron-hole pair, in which electron resides in donor and hole in acceptor, and are still Coloumbically bound. However, the low efficiency, nearly 16%[77] till the date, indicates that they cannot effectively generate free charge carriers at the interface. Researchers are making efforts to understand how the bound CT excitons can be effectively separated at the donor-acceptor interface over the past decade, but the issue remains.[78-81] Various perspectives such as entropy,[20, 79, 82-83] vibronic coupling,[84] dielectric enivironment,[85] energy gradient at the interface and electric field have been explained as a driving force for exciton dissociation. In fact, these different explanations had correlation with a variety of donor–acceptor morphology, which could affect the photovoltaic performance. Among various morphological factors, molecular orientation at the interface could significantly affect the OPVs efficiency.[28] Because the donor–acceptor molecular orientation can cause dipole formation that changes interfacial energetics, it can have a direct influence on CT and dissociation process hence, control of molecule orientation is crucial. Nevertheless, previous studies that reported the ultrafast charge separation dynamics were mainly investigated from the bulk heterojunction sample, in which the characterization of the molecule orientation becomes difficult. In addition, the signal comes from an ensemble of many interfaces with different molecular orientations. On the device level, the effect of the orientation was distinguished by measuring its efficiency; however, such measurements cannot track the CT events and dynamics.

Instead, it incorporates charge transport and collection events, which obscures the actual effect of molecular orientation on exciton dissociation.

While the search for understanding the exact exciton dissociation process continues, some recent works have illustrated the importance of spatial delocalization of electron wavefunction.[28] The larger the delocalization size, the smaller is the exciton binding energy. Hence, it can facilitate the exciton dissociation process. Advancement to this concept would be enabling the delocalized wavefunction in a preferred orientation, which favors the exciton dissociation. For example, in face-on orientation of conjugated organic molecules delocalized wavefunction orients in orthogonal direction (π-stacking direction), along which the charge transport is favored. On the other hand, there are studies that support the spatial localization of excitons to the cold CT states before the dissociation event. Furthermore, effective exciton dissociation has been reported in non-fullerene OPVs despite of small energy offsets (energy difference between HOMO of donor and LUMO of acceptor) at interface in contrast to the prevailing notion of large energy offset requirement for exciton dissociation. In addition, exciton dissociation has been observed at some interfaces with sub-band gap excitations. From these discussions, we can infer that the argument for exciton dissociation mechanism stems from the difference in interfacial morphology/geometry of the donor-acceptor materials. Therefore, the right choice of materials with a design of geometric structure that favors the exciton dissociation process would be a crucial step for building efficient OPV devices.

We investigated the wavefunction orientation dependent exciton dynamics on three different hybrid systems with two distinct molecular orientations: face-on (F_8ZnPc – ZnPc on HOPG) and edge-on (F_8ZnPc – ZnPc on SiO_2/Si and ZnPc – C_{60} on Au). Note that the use of non-fullerene acceptor (F_8ZnPc) material can provide the advantage of tailoring its optical and

electronic properties, if required, unlike fullerenes. Moreover, the orientation can be precisely controlled on the planar molecules (ZnPc and F_8ZnPc) compared to the spherically symmetric C_{60}. Despite of the type II band alignment in all the systems, an uphill energy process, spontaneous (SED), was observed within ps timescale in face-on orientation system whereas cold excitons, a downhill energy process was observed in the edge-on orientation system. We hypothesize that the SED is driven from the entropic force resulting from the relative orientation of the electron and hole wavefunction at the interface. Furthermore, based on our results we attempted to provide a fresh perspective on exciton dissociation pathway in contrast to the prevailing "hot" or "cold" pathway.

4.2 Sample Preparation, Characterization and Method

C_{60}, ZnPc and F_8ZnPc molecules (purity > 99%, sublimed) were purchased from the commercial vendor and were used as received. These molecules were deposited on different substrates in an ultrahigh vacuum (UHV) ambient with a base pressure of 1×10^{-9} Torr.

F_8ZnPc – ZnPc on HOPG: A 10 nm ZnPc film was first deposited on highly oriented pyrolytic graphite (HOPG) substrate, which was followed by sequential deposition of F_8ZnPc film (1 nm – 20 nm). The growth rate was 0.7–0.8 Å/min and the substrate was kept at room temperature (RT). Prior to the deposition, the outer surface of the HOPG substrate was peeled off by using a scotch tape and it was annealed at 400 °C for 12 hours in an UHV ambient with a base pressure of 1×10^{-9} Torr. Both molecules maintained face-on orientation.[56]

F_8ZnPc – ZnPc on SiO_2/Si: At first, 10 nm ZnPc film was deposited at a faster growth rate of 2.5 – 3.0 Å/min followed by sequential deposition of F_8ZnPc film (1 nm – 12.5 nm) at a rate of 0.7–0.8 Å/min. The Si substrate was kept at RT. Prior to the deposition, the substrate was ultrasonically cleaned and annealed at 400 °C for 12 hours in an UHV ambient with a base

pressure of 1×10^{-9} Torr. Similar procedure was applied in previous work.[56] Both molecules maintained edge-on orientation.

ZnPc – C_{60} on Au: The deposition for this system has been discussed in section 3.2 of Chapter 3. C_{60} had spherical orientation on Au while ZnPc maintained edge-on orientation on C_{60}.

After deposition, the sample was transferred *in-situ* to the main UHV chamber with a base pressure $< 1 \times 10^{-10}$ Torr, where ultraviolet photoemission spectroscopy (UPS) and time-resolved two photon photoemission spectroscopy (TR-TPPE) measurements were performed.

Photoemission experiment

The UPS measurement was done using He-I emission line (21.22 eV) generated from a UV discharge lamp. In the TR-TPPE measurement, we used a pump laser pulse (1.77 eV, 25 fs) and a probe laser pulse (4.68 eV, 65 fs). Any changes in the experimental conditions will be mentioned while discussing the experimental data. Details of the UPS and TR-TRPPE technique can be found in section 2.2 of Chapter 2.

Characterization of face-on and edge-on orientation from ionization potential

Before discussing the results, we will confirm the orientation of the molecules. Since the IP value of the phthalocyanine (Pc) molecules for face-on and edge-on orientation significantly differs (~ 0.5 eV difference),[56, 62, 86] we can characterize the molecular orientation by determining their IP value. For example, the IP of CuPc, ZnPc, H_2Pc molecules with a face-on orientation are ~ 0.4 eV higher than that with an edge-on orientation. However, the opposite holds for fluorinated-Pc (e.g. F_8ZnPc)[59], i.e. the face-on orientation has a smaller IP than the edge-on orientation. This is because the H-atoms, which have a low electronegativity, on the peripheral of the planar molecule, are replaced by F-atoms, which have a high electronegativity. Figure 4.1a

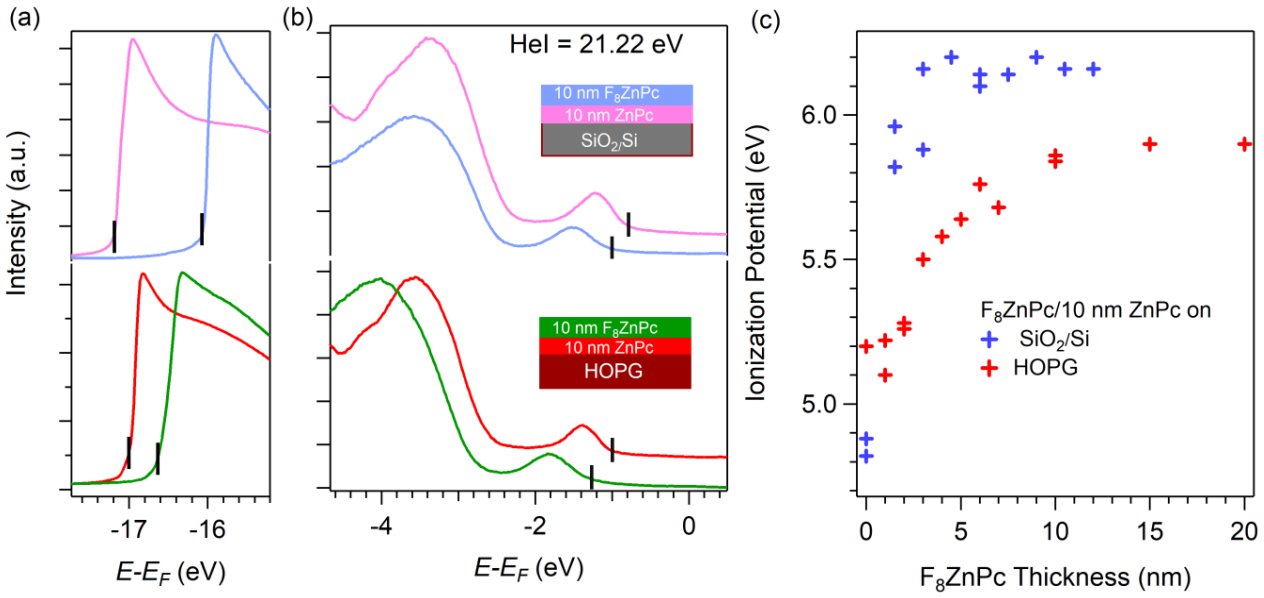

Figure 4.1: UPS spectra of 10 nm ZnPc, and 10 nm-F_8ZnPc – 10 nm-ZnPc films grown on HOPG (lower) and SiO_2/Si (upper). Panel (a) shows the UPS spectra near SECO region and panel (b) shows the same set of spectra near HOMO region. The spectra were collected with He-I emission line (photon energy = 21.22 eV). (c) The IP value as a function of F_8ZnPc thickness on a 10 nm ZnPc layer on the two different substrates, HOPG and SiO_2/Si, are shown in blue and red symbols, respectively. The data point at 0 nm corresponds to the IP value of 10 nm ZnPc.

and 4.1b show the UPS spectra of 10 nm-ZnPc and 10 nm-F_8ZnPc – 10 nm-ZnPc films deposited on SiO_2 (upper) and HOPG (lower) near the secondary electron cut off (SECO) and highly occupied molecular orbital (HOMO) region respectively. The IP value is calculated from the above spectrum by subtracting the energy difference between the two onsets from the He I photon energy (see section 2.2 of chapter 2 for IP calculation). F_8ZnPc always has a higher IP than ZnPc, which is expected due to more electronegativity of F-atoms.[87]

The calculated IP value is 5.20 eV (red marker) and 4.82 eV (blue marker) for the 10-nm ZnPc film deposited on HOPG and SiO_2/Si, respectively. These values are labelled in Figure 4.1c where 0 nm in the x-axis plot refers to 10 nm thick ZnPc layer. These values are consistent with the IP for phthalocyanine (Pc) molecules having face-on and edge-on orientation respectively.[56] Indeed, it is well-known that Pc molecules grow on HOPG and SiO_2 with face-on

and edge-on orientation, respectively.[56, 59] We further characterize the orientation of F_8ZnPc grown on top of ZnPc. Figure 4.1c shows the IP value of different thicknesses of F_8ZnPc grown on top of the 10 nm ZnPc on HOPG (red) and SiO_2/Si (blue). The IP transitions to higher value as the F_8ZnPc film becomes thicker. For thicknesses > 10 nm, the IP becomes steady and we use this value to determine the orientation of F_8ZnPc molecules. The calculated IP value of the 10 nm-F_8ZnPc – 10 nm-ZnPc on HOPG sample is 5.84 eV while that of 10 nm-F_8ZnPc – 10 nm-ZnPc on SiO_2 is 6.16 eV. Here, the higher IP value of F_8ZnPc molecule with an edge-on orientation is due to the opposite (downward pointing) surface dipole originated from the intramolecular C – F bond in contrast to the upward pointing surface dipole in edge-on ZnPc originated from intramolecular C – H bond.[59, 86] This difference in the IP value for edge-on metal Pc's (MPc's) and fluorinated MPc's agrees well with previous works.[56, 59, 62, 86] In summary, our results show that both ZnPc and F_8ZnPc molecules have a face-on orientation on HOPG whereas edge-on on SiO_2.

4.3 Experimental results and discussions

The data obtained from TR-TPPE for face-on and edge-on molecular orientation will be compared. We will show how these two different molecular orientations affect the evolution of exciton dynamics and hence the charge separation First, we will describe the spontaneous exciton dissociation (SED) observed on face-on orientation. Later, this result will be compared to CT exciton dynamics observed on edge-on molecular orientation.

4.3.1 Face-on Molecular Orientation (F_8ZnPc – ZnPc on HOPG)

(a) Scheme and the energy level diagram

The schematic of the F_8ZnPc – ZnPc on HOPG is shown in Figure 4.2a. The molecular structure of ZnPc and F_8ZnPc is similar. 8 F-atoms in F_8ZnPc is formed by replacing 8 H-atoms

of ZnPc and the presence of F-atoms increases the electronegativity of F_8ZnPc. As evidenced from the IP value discussed earlier, ZnPc has face-on on HOPG and F_8ZnPc maintains the same orientation on top of ZnPc. Because of the face-on orientation, both electron and hole wavefunctions in the CT exciton delocalize along the direction that is perpendicular to the interface (Figure. 4.2a). The more details on electron-hole wavefunction orientation can be found in the section 2.4.2 of Chapter 2. The HOMO positions of ZnPc and F_8ZnPc of our sample are determined using UPS. The UPS spectra of 10 nm ZnPc and various thicknesses of F_8ZnPc films grown on top of 10 nm-ZnPc film are shown in Figure. 4.2b. The HOMO-offset ($E_{HOMO\text{-}ZnPc} - E_{HOMO\text{-}F\text{-}ZnPc}$) at the interface was found to be ≈ 0.45 eV and the HOMO shifts to a slightly lower energy as the F_8ZnPc film thickness increases. The HOMO positions, together with the excited-states energy, as a function of the F_8ZnPc thickness are shown in Figure 4.2c. Because the F_8ZnPc molecule has a larger IP value compared to the ZnPc and both have similar optical band

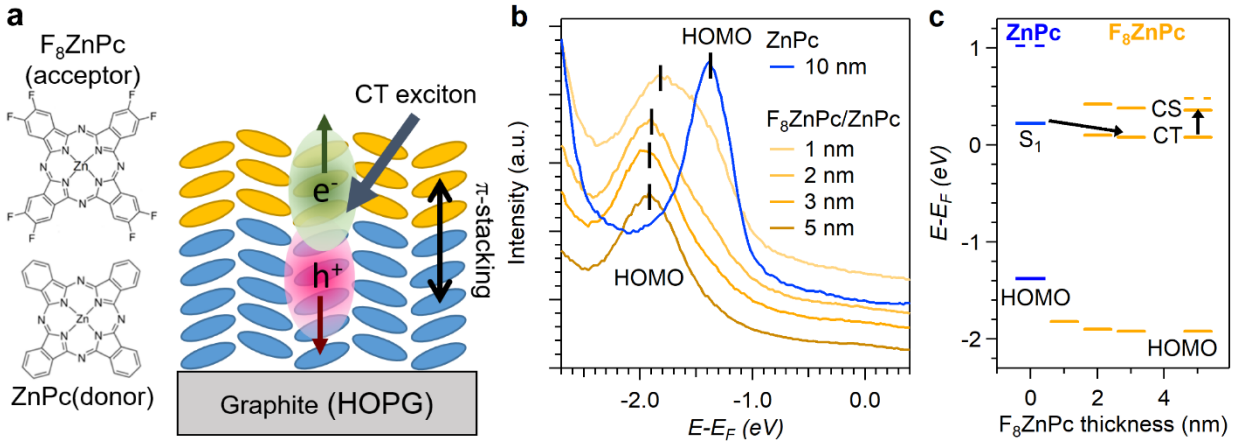

Figure 4.2: (a) A schematic diagram of F_8ZnPc–ZnPc interface on HOPG. Both F_8ZnPc and ZnPc molecules grow on the HOPG substrate with a face-on orientation. As a result of this orientation, the electron and hole wavefunctions within the CT exciton are delocalized in a direction that is perpendicular to the interface. (b) UPS spectra of 10 nm-ZnPc sample and various F_8ZnPc thicknesses on top of it. The HOMO peak positions for ZnPc and F_8ZnPc are marked by the vertical bars. (c) Energy level diagram at the F_8ZnPc – ZnPc interface. The positions of the HOMO and the CS/CT states are determined by our UPS and TR-TPPE experiments, respectively. The dashed lines indicate the positions of the LUMO-edge state reported in the literature. [88]

gap,[87] the F_8ZnPc – ZnPc interface has a type-II band alignment with the F_8ZnPc and the ZnPc acting as an electron acceptor and donor respectively. The energies for the S_1, CT and charge separated (CS) states are measured by the TR-TPPE and will be discussed in the next paragraph.

(b) Observation of spontaneous exciton dissociation (SED)

The TR-TPPE spectrum for a bilayer 5 nm-F_8ZnPc – 10 nm-ZnPc sample is shown in Figure 4.3a. The pseudocolor represents photoemission intensity. The excited state energy, in *y*-axis, is referenced with respect to the F_8ZnPc's HOMO measured by the UPS. Since they have similar optical band gap, the pump photons excite the singlet (S_1) exciton in both ZnPc and F_8ZnPc. However, only excited electrons near the surface of the F_8ZnPc film is probed by the photoemission because of the limited escape depth (~ a few nm) of photoelectrons.[89] The intense signal near the temporal overlap of pump-probe pulses (time-zero) is attributed to the photoexcited S_1 exciton in F_8ZnPc. As shown in Figure 4.3b, a similar spectral feature near the time-zero is also observed in the standalone 15 nm F_8ZnPc on HOPG sample. Similar to the S_1 exciton in ZnPc[55, 63] the photoexcited S_1 exciton in F_8ZnPc is expected to relax in energy within hundreds of fs. From our previous studies on ZnPc[55, 63], the relaxed F_8ZnPc's S_1 exciton should have a peak centered at ~ 1.6 eV relative to its HOMO level (or ~ 4.8 – 4.9 eV below the vacuum level). However, this energy level falls short of the spectral range that can be detected by our 4.68 eV probe photons. Hence, the signal becomes much weaker because the S_1 peak is away from the detectable spectral range of the probe pulse. This explains the rapid intensity decay in the first few hundreds of fs after the pump excitation.

One distinct observation between the spectra of the bilayer, F_8ZnPc – ZnPc and the standalone, F_8ZnPc samples is: The long-lived signals (> 1 ps) in the spectral range of ~ 1.9 – 2.5 eV above the F_8ZnPc's HOMO exists in the bilayer sample, but not in the F_8ZnPc sample (see in

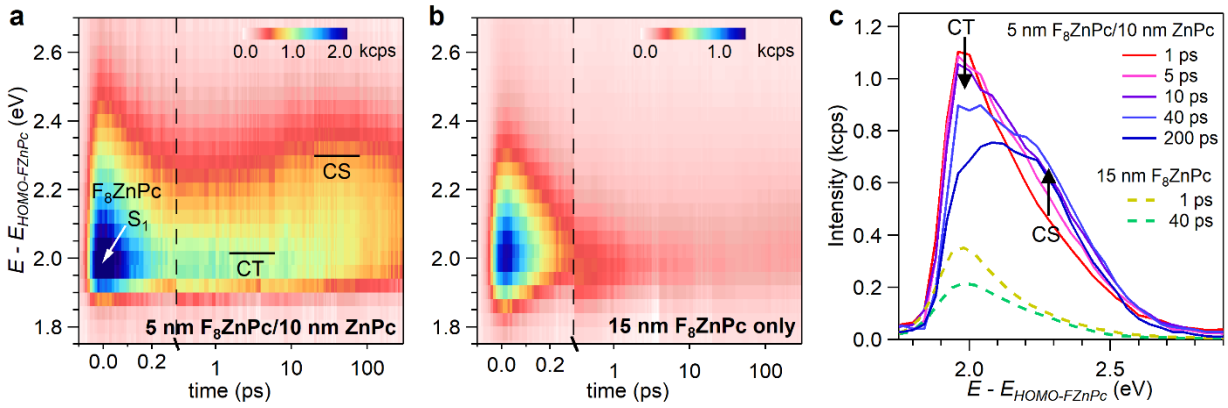

Figure 4.3: The TR-TPPE spectra for a (a) bilayer film, 5 nm-F_8ZnPc on 10 nm-ZnPc and (b) standalone 15 nm-F_8ZnPc film. The plot is splitted by the vertical dashed line to show the dynamics on two different timescales. (c) The TR-TPPE spectra at selected pump-probe delay times for the two samples. For the F_8ZnPc–ZnPc sample, the intensity of the bound-CT state (lower in energy) decreases while that of the charge separated (CS) state (higher in energy) increases with time. These states are not observed in the standalone F_8ZnPc (dashed lines).

the right side of Figure 2a, b). For a better visualization, the spectra at selected pump-probe delay times are plotted in Figure 4.3c. Two states at ~ 2.0 eV and ~ 2.3 eV can be identified for the bilayer (solid line traces) whereas the standalone film shows only the lower energy state (dashed line traces). Because these strong photoemission signals at higher energy regime in the spectrum show up only in the bilayer sample, they must be originated from the CT at the donor-acceptor interface. The lower energy state has an energy ~ 2.0 eV, which is higher than that of the F_8ZnPc's S_1 state (~1.7 eV). It is assigned to an interfacial CT state because CT excitons have a reduced exciton binding energy (hence, a higher electron energy) as compared to the self-exciton in F_8ZnPc. The higher energy peak position (2.3 eV) is very close to the position of the edge of the F_8ZnPc's LUMO measured by inverse photoemission spectroscopy (IPES) studies (~ 2.4 eV above the HOMO peak position[88]) and we assign it as charge separated (CS) state.

In Figure 4.3c, it is apparent that the intensity of the CS state increases with time while the intensity of the CT state decreases. Hence, the overall spectral weight shifts towards a higher energy. Similar energy upshift is not observed in the spectra of the standalone F_8ZnPc sample

(dashed line in Figure 4.3c). The shifting of the overall spectral weight to a *higher* energy is a surprising observation because excited electrons usually relax to lower energy states on these ultrafast timescales (the Kasha's rule). Our result indicates that CT excitons are dissociated spontaneously, instead of relaxing to a lower energy state, after its creation. Because the initially Coulomb binding energy of CT exciton is transferred to the free electrons generated after exciton dissociation, CS state has higher energy. Similar CT and CS peaks can also be identified in spectra for samples with other F_8ZnPc's thicknesses, although the CT (CS) state is less apparent

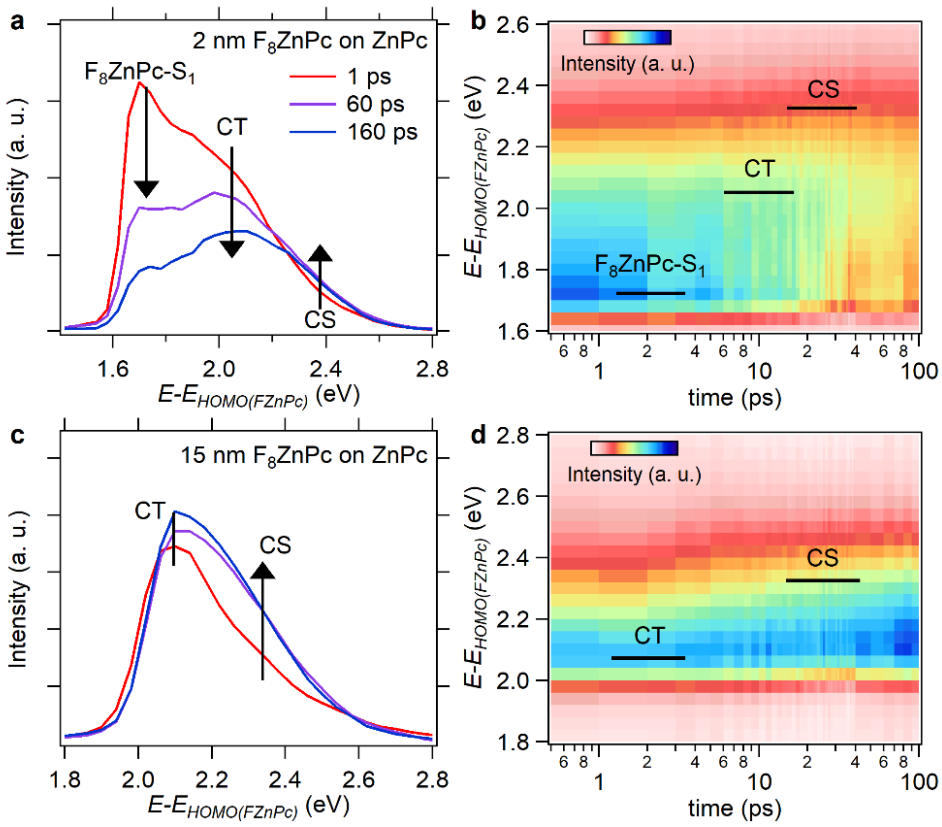

Figure 4.4: (a) TR-TPPE spectra of the 2 nm-F8ZnPc – 10 nm-ZnPc sample at selected delay times and the corresponding (b) TR-TPPE 2D plot of the same sample. (c) TR-TPPE spectra of the 15 nm-F_8ZnPc – 10 nm-ZnPc sample at selected delay times and the corresponding (d) TR-TPPE 2D plot of the same sample.

in spectra obtained from samples with a thicker (thinner) F_8ZnPc layer (Figure 4.4). For the 2 nm-F_8ZnPc – 10 nm-ZnPc sample, the overlaying F_8ZnPc layer is thin. The signal is dominated

by that originated from the interfacial CT state. The intensity growth of the CS state is not pronounced (Figure 4.4a, b), which indicates that the ultrathin F_8ZnPc layer can prohibit charge separation by limiting the electron-hole separation. On the contrary, the intensity growth of the CS state is more pronounced in the 15 nm-F_8ZnPc – 10 nm-ZnPc sample (Figure 4.4c, d). Despite of the pronounced CS state in the latter sample, we would like to point out that the absolute intensity is much weaker for the 15 nm sample as compared to the 2 nm sample (see Figure. 4.6c in next section). Our results indicate that the CT exciton populated by the interfacial energy transfer can transform directly into CS state without first relaxing to a lower energy CT state. We term this process as spontaneous exciton dissociation (SED) to describe the uphill energy process.

Furthermore to confirm this claim, measurement for the bilayer sample at low temperature (LT) was performed. The spectrum obtained from LT (165 °K) measurement is plotted in Figure 4.5a. Similar to the spectra (Figure 4.3c) taken at RT (300 °K), both the CT and CS states are identified. In order to compare the CS yield at RT and LT, the normalized time

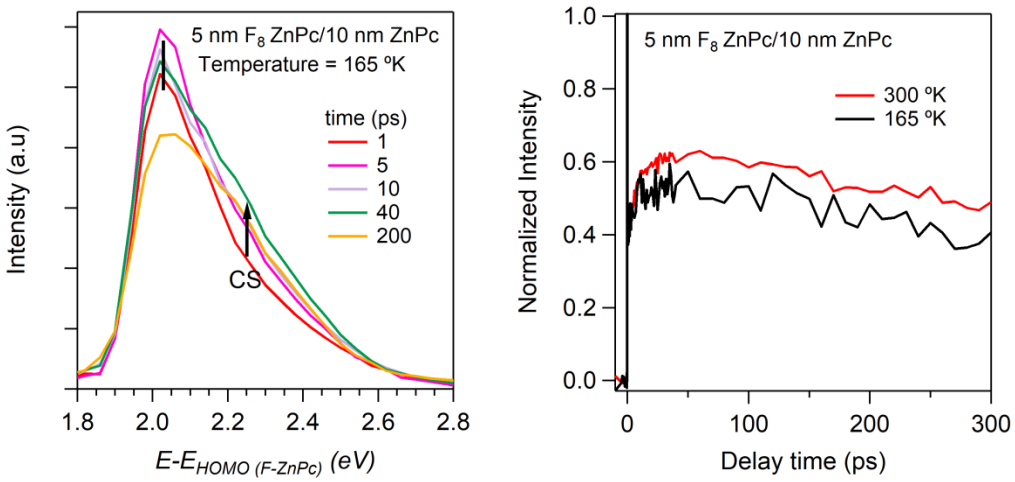

Figure 4.5: (a) TR-TPPE spectra taken at low temperature (LT) for 5 nm F_8ZnPc–10 nm ZnPc at selective delay times. The upward arrow indicates increase in intensity around the CS spectral energy range, indicated by the horizontal bar. (b)Normalized time dynamics of the same CS spectral range at low temperature (black) plotted against CS dynamics at room temperature (red).

dynamics of the intensity at the spectral range corresponding to the CS state is plotted in Figure 4.5b. An increase in the CS intensity at LT is observed too, though the intensity is somewhat weaker compared to the RT. Thus, we conclude that the SED process can still occur at LT but with a lower yield.

(c) CS intensity and translational time (τ_{trans})

In order to understand the temporal evolution of CS dynamics, integrated intensity of CS spectral range for different F_8ZnPc film thickness were analyzed. For clarity, only the traces for selected F_8ZnPc film thickness (2, 5 and 10 nm) are plotted in Figure 4.6a. The maximum of integrated intensity is normalized to 1. It is observed that the intensity of CS carriers for 2 nm (red trace) plateaus quickly whereas it takes longer time for 20 nm (yellow trace). Such dynamics was expected. Since our photoemission technique is surface sensitive, it can detect only those separated electrons that reach the surface region of the F_8ZnPc. Thus, we expect a longer time

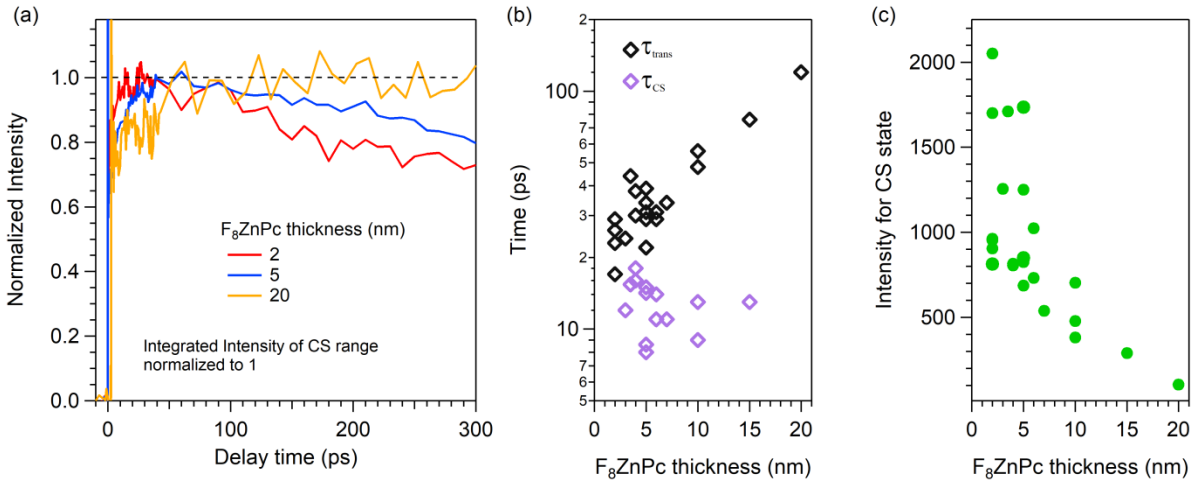

Figure 4.6: (a) Temporal evolution of the maximum intensity of CS spectral range for various F_8ZnPc film thickness. The intensity is normalized. (b) The plot of translational time (τ_{trans} black) and the exciton dissociation time (τ_{cs} purple) as a function of F_8ZnPc film thickness. (c) The plot of the maximum photoemission intensity of CS spectral range as a function of F_8ZnPc film thickness.

for the separated charge carriers in the thicker F_8Znc films to reach the surface because it has to transport from the buried interface. We refer this time as translational time (τ_{trans}), the time taken for the separated charge carriers to reach the top surface from the F_8ZnPc – ZnPc interface. Likewise, the intensity of the separated charge carriers should decrease for thicker films because these carriers diffuse across the thicker films. To quantify this, two tangents were drawn along the either side of the CS intensity plateau (not shown in the figure). The point of intersection of the two tangent lines gives the translational time (x-axis) and maximum intensity of CS carriers (y-axis). Thus obtained time as a function of thickness is plotted in Figure 4.6b (black markers). Two or more values for the same thickness are the data obtained from different sets of experiment. While 2 nm takes the least τ_{trans} (around 20 ps), we observed a general trend of increase in time as F_8ZnPc film becomes thicker. Likewise, the concentration of CS carriers as a function of F_8ZnPc film thickness is plotted in Figure 4.6c. As expected, the intensity of separated charge carrier decreases as F_8ZnPc film thickness increases for the same reason discussed earlier. Hence, our results confirm that the separated charge carriers are originated from the buried F_8ZnPc – ZnPc interface.

(d) Exciton dissociation time (τ_{cs}) from global fit

The quantitative information on exciton dissociation time (τ_{cs}) could be a fundamental in understanding the exciton dissociation/charge separation mechanism at organic based donor – acceptor system. To determine τ_{cs}, it is essential to understand how CS spectral shape evolves with time. However, the CT and CS states in our experimental data are in vicinity to each other. In fact, the CS level evolves just above the CT energy level; hence, they are spectrally convoluted. Deconvolution of these two states is essential to determine the evolution of CS

spectral shape and hence the τ_{cs} time.

A fit equation $I(t) = A_1*f_1(x) + A_2*f_2(x)$ was used for the global fit of TR-TPPE spectrums at successive delay times, where the function $f_1(x)$ and $f_2(x)$ are modelled to define the shape of a typical CT and CS spectrum respectively. Hence, at first, representative CT and CS spectra were identified, which usually occurs within ~ 1 ps and ~ 200 – 300 ps timescale respectively. In order to achieve a more precise representative spectral shape, an average of the spectrums near the aforementioned time scales was taken. A_1 and A_2 are the time dependent fitting parameters to be determined such that $A_1 = 1$, $A_2 = 0$ in the above equation for I(t) gives the initial representative CT spectrum while $A_1 = 0$, $A_2 = 1$ returns the final representative CS

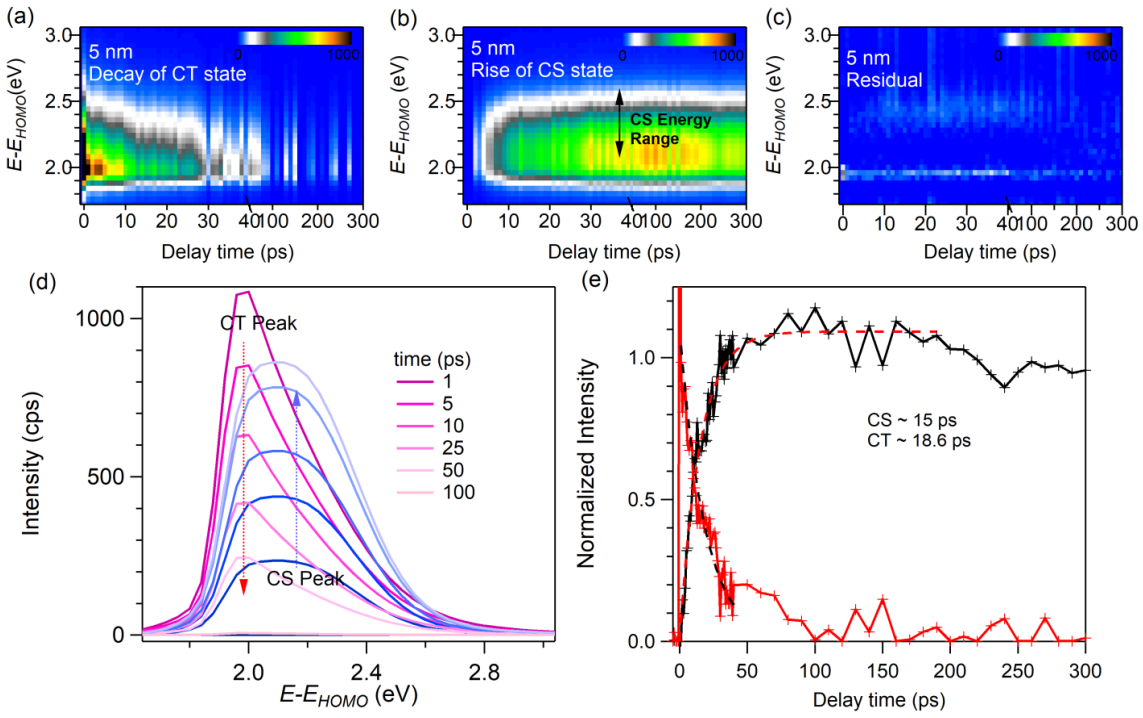

Figure 4.7: Global fitting for deconvolution of CT and CS state in the TR-TPPE spectrum of 5 nm F_8ZnPc. 2D image of the deconvoluted (a) CT state and (b) CS state. (c) Residual of the fit (d) Spectrum obtained from the fit at selected delay times. (e) Temporal evolution of CS and CT state obtained from the fit.

spectral shape. Hence, the plot of A_1 and A_2 value gives the evolution of CT and CS state respectively.

Figure 4.7 (a) and (b) are the deconvoluted 2D images of the CT and CS state respectively obtained from the fit. The fit residual (Figure 4.7c) is below 5% of the experimental data with a slightly greater value around CT and CS region, thus our model is a good fit. The two peaks are labelled as "CT" and "CS", even though we note that the "CS" peak would represent a mixture of CT excitons and CS electrons that are in dynamical equilibrium at large delay times. The CT bound state is at the lower energy regime, nearly 2.0 eV referenced to HOMO of F_8ZnPc, where the intensity decays gradually (Figure 4.7a). This value agrees well with the experimental data. Simultaneously, the CS state peak rises at higher energy regime, nearly 2.25 eV (Figure 4.7b). This CS peak value is slightly lower than the experimental data because the intensity contributed from the CT region is removed after deconvolution. The spectrum plot of CT state (dark pink to light pink) at selected delay times and the corresponding rise of the CS state (dark blue to light blue) are plotted in Figure 4.7d. It is observed that the CS state rises (up arrow) simultaneously with the decay of CT state (down arrow). The intensity coefficients, A_1 and A_2, obtained from the fit results are plotted against its corresponding time (Figure 4.7e). Fitting the evolution of the CT/CS (A_1/A_2) intensity to a single exponential decay/rise function (solid lines in Figure 4.7e) yields time constants (CT: (18.6±1.9) ps / CS: (15±1.5) ps). These values are close within its range of standard deviation and our residual error that stems from the limitation of the fit model in perfectly fitting the experimental data. This time constant quantifies how fast the electron gains its energy and it is attributed to the charge separation time, τ_{cs}. Overall, we see a long-lived CS state, unlike CT state which disappears eventually. The long-lived CS state is a characteristic feature of free charges.

Similar fitting procedure was applied to the spectra collected from samples with different F_8ZnPc thicknesses except for 15 nm and 20 nm samples in which the CT peak could not be clearly identified. The time constants τ_{cs} obtained from the exponential rise of the CS peak are plotted in Figure 4.6c (purple marker). Although we will not compare the magnitude of τ_{trans} and τ_{cs} directly, they show very different thickness dependences. Unlike τ_{trans}, τ_{cs} is less sensitive to the film thickness. Indeed, it has a somewhat smaller value for larger F_8ZnPc's thickness, which indicates that a thicker F_8ZnPc layer (i.e. more delocalization) favors the SED.

(e) SED from sub-bandgap photoexcitation

There exist arguments between the "hot" and "cold" exciton dissociation pathways. In the former case, the hot CT excitons decompose into free carriers without relaxing into cold CT excitons. However, there are also evidences of effective charge separation with sub-bandgap (pump excitation below the optical band gap) photoexcitation, which supports the latter case. Note that the direct optical excitation of CT state occurs in the latter case. To distinguish the difference between these two pathways, the bilayer 5 nm F_8ZnPc – 10 nm ZnPc was pumped with the wavelength below its optical band gap (740, 780 and 830 nm). Note that the optical band gap of ZnPc and F_8ZnPc is centered at ~ 700 nm. Figure 4.8a, b shows the 2D image of the TR-TPPE spectra obtained with pump 780 nm and 830 nm. The dotted vertical lines are drawn to separate the exciton dynamics in two different time scales. With pump 780 nm, we observed the results similar to 700 nm pump (see Figure 4.3a). Both the CT and CS states are observed in the 2D image obtained from the TR-TPPE. However, the CS signal is weak because the sub-band gap excitation energy 1.59 eV (780 nm) excites less signal compared to 1.77 eV pump (700 nm). The pseudocolor scale represents the photoemission intensity. A careful observation shows that the CT state is a little more pronounced for a few tens of ps, which is a good sign of direct

optical excitation of CT state in the F_8ZnPc film. The TR-TPPE spectra at selected probe delay times are shown in Figure 4.7c. The rise in intensity is observed in the spectral range from ~ 2.0 eV to 2.4 eV, an uphill energy conversion process similar to spectrum obtained with pump 700 nm. With the pump excitation energy 1.49 eV (830 nm), the CT signal is too weak (almost an order of magnitude lesser than 700 nm) and hence the CS intensity becomes even weaker to be

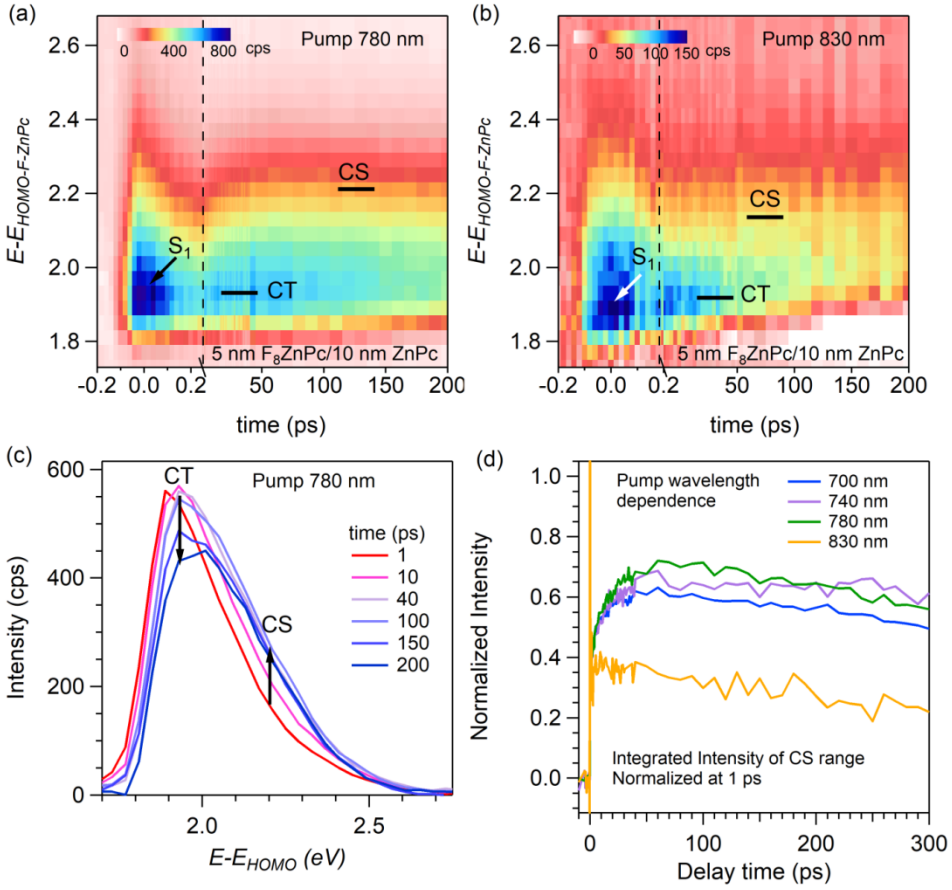

Figure 4.8: The TR-TPPE spectra for a 5 nm-F_8ZnPc on 10 nm-ZnPc bilayer film obtained with pump (a) 780 nm and (b) 830 nm. The plot in (a) is split by the vertical dashed line to show the dynamics on different timescales whereas the inset in (b) shows the dynamics at initial time scale. (c) The TR-TPPE spectra at selected pump-probe delay times for the same sample obtained with pump 780 nm. The CS states are observed similar to that obtained with its optical band gap excitation (see Figure 4.3).

detected by the analyzer (Figure 4.7b). Despite of the weak intensity, a trend of uphill energy conversion is still observed in the 2D plot. Figure 4.8d shows the pump wavelength dependence

temporal dynamics of the integrated intensity at the CS spectral range. The intensity was normalized after 1 ps because the spectral shift from CT to CS occurs after 1 ps. At first, a quick decay within 1 ps and then the rise in the CS intensity was observed for pump wavelengths 740 nm and 780 nm similar to 700 nm. For 830 nm, the rise of the CS intensity is not obvious. However, the signal at a higher energy regime persists for a longer timescale, which suggests the existence of CS state because the higher energy states are not populated in the system where SED is not favored. Instead, if SED is not favored, intensity decays slowly due to recombination and other decay channel occurs at 100's of ps timescale. Thus, we observed SED with both optical band gap and sub-band gap excitation. Our results indicate that the "hot" and "cold" pathway argument is irrelevant if the system favors the SED process.

4.3.2 Edge-on molecular orientation

We will discuss the exciton dynamics on two different systems with edge-on orientation: F_8ZnPc – ZnPc on SiO_2/Si and ZnPc – C_{60} on Au.

(a) Downhill energy process – (F_8ZnPc – ZnPc on SiO_2/Si)

The same bilayer F_8ZnPc – ZnPc was grown on SiO_2/Si at which both molecules maintained edge-on orientation. The deposition procedure for the bilayer and characterization techniques can be found in the section 4.2. The schematic of this structure along with the electron-hole wavefunction orientation is shown in Figure 4.9a. Since both wavefunctions are parallel to each other, they are more likely to be pinned at the interface because of the increased spatial overlapping of the two wavefunctions. Thus, it is less likely to reduce the exciton binding energy, which is a barrier for the exciton dissociation. The energy level diagram with the values measured from the UPS and TR-TPPE is shown in Figure 4.9b. The energy level is referenced

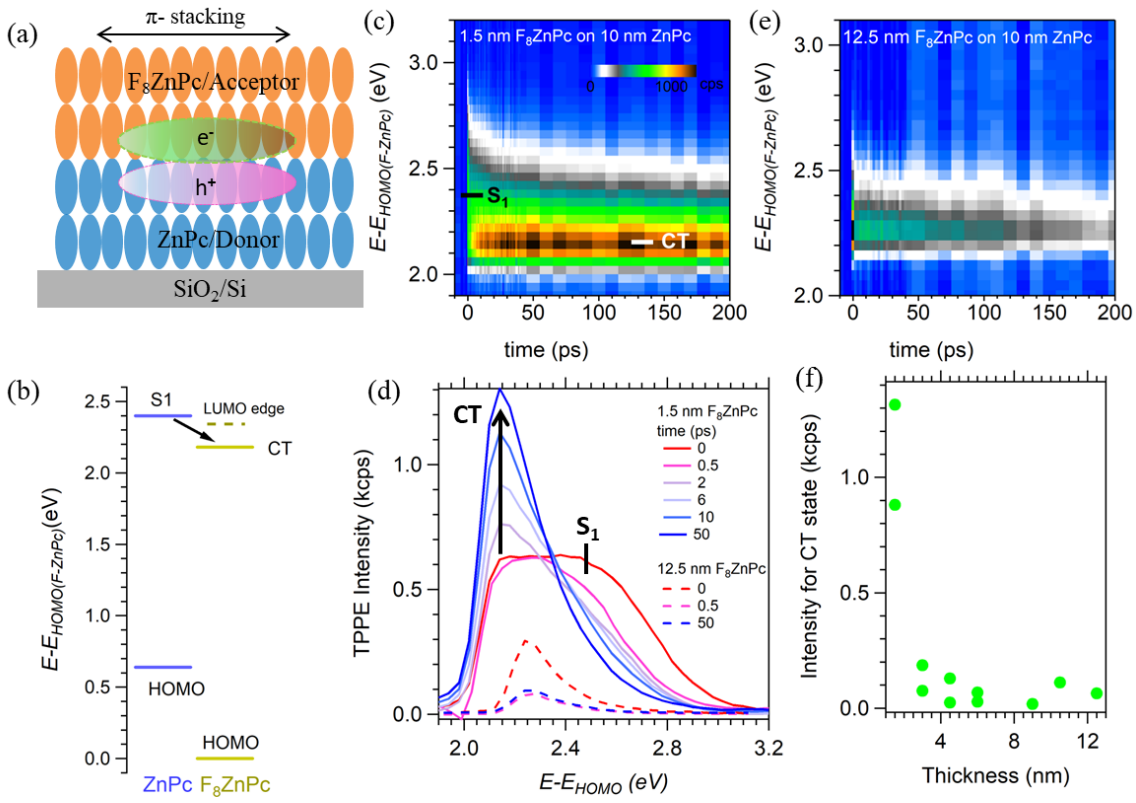

Figure 4.9: (a) A schematic showing the electron-hole wavefunction oientation at F_8ZnPc–ZnPc interface with edge-on orientation on SiO_2/Si (b) The energy level diagram of F_8ZnPc–ZnPc interface referenced with respect to the HOMO of F_8ZnPc. The 2D TR-TPPE spectrum of (c) 1.5 nm F_8ZnPc and (e) 12.5 nm F_8ZnPc on 10 nm ZnPc. (d) Their respective TR-TPPE spectra at selected pump-probe delay times. All the energy levels are referenced w.r.t. HOMO of F_8ZnPc. (f) The maximum CT intensity as a function of F_8ZnPc thicknesses on 10 nm ZnPc.

w.r.t. F_8ZnPc's HOMO. The LUMO edge of the F_8ZnPc (dashed line ~ 2.4 eV), measured by IPES technique, is the reported value in the literature.[88] It has a type II band alignment and hence the CT from ZnPc (donor) to the F_8ZnPc (acceptor) can be expected. The experimental conditions for the TR-TPPE were kept similar to the F_8ZnPc – ZnPc bilayer with face-on orientation discussed earlier.

Figure 4.9c shows the 2D TR-TPPE spectra of the bilayer 1.5 nm F_8ZnPc – 10 nm ZnPc on SiO_2/Si. Upon photoexcitation, energy state at ~ 2.45 eV is instantaneously populated. Although, S_1 excitons from both bilayers could be populated, F_8ZnPc's S_1 state (~ 4.9 eV below

vacuum level) falls outside of the spectral range that cannot be detected by our probe energy 4.68 eV. We note that HOMO position of the ZnPc is nearly 0.65 eV lesser than that of F_8ZnPc (not shown in the figure). The instantaneously populated signal agrees well with the ZnPc's S_1 position (~ 1.77 eV) when referenced to ZnPc's HOMO hence, the S_1 signal is mainly contributed from the ZnPc layer. However, the signal is weak due to the overlaying F_8ZnPc film. The S_1 signal decays quickly and the lower energy state at ~ 2.16 eV starts populating. The TR-TPPE spectra at selected probe delay times are plotted in Figure 4.9d. We observed the decay of S_1 state centered at 2.45 eV within a few ps. The decay of the S_1 signal indicates the CT to F_8ZnPc.We noticed that the S_1 state is relatively long-lived compared to face-on orientation, which suggests face-on orientation facilitates to CT. We refer the lower energy state at ~ 2.16 eV as the CT state. The CT state is more pronounced than the S_1 because the electrons in the CT state reside in the F_8ZnPc layer hence, they are more detectable due to surface sensitive photoemission technique. The CT state keeps populating for ~ 50 ps. After that, the intensity slightly decreases and becomes steady at ~ 100 ps. The peculiar difference of this edge-on system with face-on is; higher energy states (CS states) are not observed in the edge-on system. Unlike the SED, an uphill energy conversion process observed in face-on, the edge-on F_8ZnPc – ZnPc system showed downhill energy conversion process. This difference is explained by the two distinct wavefunction orientation on these two systems. The parallel orientation of electron-hole wavefunction at the interface in edge-on orientation system keeps the electron and hole closer to each other at the interace. Hence, the exciton binding energy does not decrease and the dissociation is less likely unlike the perpendicular wavefunction orientation in face-on system where electron and hole wavefunction tends to move apart from each other. Similar dynamics were observed for thicker films of F_8ZnPc but the signal got weaker with increasing thickness of

F_8ZnPc films. Figure 4.9e shows the 2D TR-TPPE spectrum of 12.5 nm F_8ZnPc and the spectrum at selected delay times are shown by the dotted lines in Figure 4.9d. The intensity is weaker than 1.5 nm F_8ZnPc because the underlying ZnPc no more contributes to the S_1 signal. The signal at the lower energy regime is weak and observed for a few tens of ps; eventually, the signal disappears. We like to recall here that the S_1 signal from standalone F_8ZnPc film disappears within a few ps (see Figure 4.3b). Thus, the signal at the lower energy regime in the 12.5 nm F_8ZnPc on 10 nm ZnPc must be originated from the interfacial CT. Similar dynamics were observed for other F_8ZnPc film thickness. The maximum CT intensity for various F_8ZnPc film thicknesses is plotted in Figure 4.9f. The CT intensity decreases as thickness increases. This was reasonable because our probe pulse cannot detect the interfacial CT exciton due to the limited escape depth of electrons.

(b) Hot CT exciton cooling dynamics (ZnPc – C_{60} on Au)

So far, our results on F_8ZnPc – ZnPc on HOPG and SiO_2/Si indicate that the SED is not a universal behavior though the CT occurs at both systems in an ultrafast timescale. Indeed, it is commonly observed or presumed that hot delocalized CT excitons first relax into bound ones in ultrafast (fs – ps) timescale. Then, the bound CT excitons dissociate through thermal activated processes. By using ZnPc – C_{60} on Au as a model system, we will show that hot CT exciton cooling instead of SED occurs at the ZnPc – C_{60} interface.[55, 72] 1 nm ZnPc was deposited on top of 4 nm C_{60} on Au. The deposition procedure and the characterization techniques have been discussed in section 3.2 of Chapter 2. Figure 4.10a shows the schematic of this system. At the interface, ZnPc molecules have an edge-on orientation relative to the interface hence, the hole wavefunction is oriented parallel to the interface whereas the electron wavefunction is spread out in all possible directions. Figure 4.10b shows the TR-TPPE spectrum at selective delay times for

the bilayer, 1 nm ZnPc – 4 nm C_{60} deposited on Au. The details on TR-TPPE have been discussed in section 3.3.1 of Chapter 3. The energy level diagram for the system is shown in Figure 4.10c. All the energy levels are referenced with respect to C_{60}'S HOMO. CT from ZnPc's S_1 state (~ 2.75 eV) to C_{60} is observed without much energy loss within 0.5 ps. Since the event

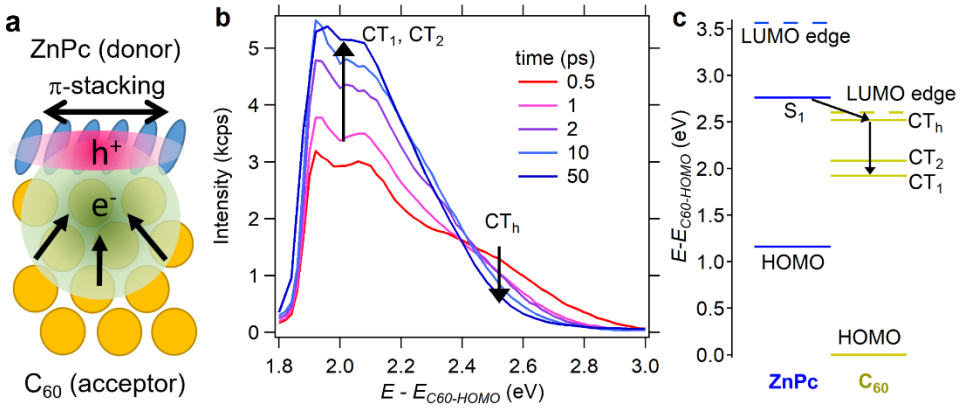

Figure 4.10: (a) A schematic diagram shows the orientation of molecules at the ZnPc–C_{60} interface used in our experiment. (b) The TR-TPPE spectra obtained from a 1 nm-ZnPc–4 nm-C_{60} sample at selected delay times. Unlike the F_8ZnPc–ZnPc interface, the intensity of the lower energy CT_1, CT_2 peaks increases as the intensity of the higher energy CT_h peak decreases. (c) The energy level diagram of the ZnPc–C_{60} interface showing the cooling of CT_h states to CT_1 and CT_2 states.

happens at an ultrafast timescale with minimum energy loss, we refer it as hot CT excitons (CT_h). The CT_h excitons are delocalized but short-lived. The downward arrow in Figure 4.10b shows the decay of CT_h excitons within a few ps. Interestingly, at ~ 2 ps timescale we see the rise in the intensity at lower energy states ~ 2 eV. These are labelled as CT_1 and CT_2 states. Since these states are long lived, they are generally termed as called cold CT states. Figure 4.10b shows the intensity rise (up arrow) of the cold CT states for a few tens of ps. The intensity rise can be explained from the viewpoint of delocalized size of electron wavefunction. In the CT_h state, the electron wavefunction is more delocalized and thus farther away from the interface to be detected. However, the localization of electron wavefunction occurs as it relaxes from higher energy to lower energy. This shifts the wavefunction center towards the interface hence, the

interfacial electrons are detected by the analyzer. Because the hole wavefunction is spread parallel to the interface, the electron wavefunction is more likely to be pinned towards the interface due to Coulomb interaction, which results to the localization of electron wavefunction. The CT_1 and CT_2 exciton size become stable once it attains thermodynamically equilibrium state. The details of the CT exciton dynamics have been discussed in chapter 3 and can be found in reference [55, 72] as well.[55, 72] Spectrally, the cooling process results in a downshift in the CT exciton energy (i.e. an increase in the exciton binding energy), which is reverse to the energy upshift observed in face-on orientation (Figure 4.3a, F_8ZnPc – ZnPc on HOPG). These cold excitons do not dissociate in the timescale accessible by our experimental set-up. However, in a different study done by our group using a time-resolved photoelectrical technique, it was found that these cold CT excitons can dissociate into free carriers in a few nanoseconds[72, 90] *via* a thermal activated channel. The detail of this experimental technique is beyond the scope of this thesis.

4.4 Rationale for SED vs hot exciton cooling

We observed SED and cold excitons formation for the same bilayer but with face-on (F_8ZnPc – ZnPc on HOPG) and edge-on (F_8ZnPc – ZnPc on SiO_2/Si) orientation respectively. Likewise, hot exciton cooling was observed in ZnPc – C_{60} on Au, in which ZnPc has edge-on orientation on C_{60}. Despite the type II band alignment for all three systems, we note that the cold exciton formation occurred only in edge-on orientation system and SED on face-on system. Here, we try to explore the ground for these two different exciton dynamics from the standpoint of delocalized electron-hole wavefunction orientation.

At the face-on molecular orientation, the electron-hole wavefunction orientation is perpendicular to the interface because of the π-stacking direction (see Figure 4.2a). Hence after

the excitation, the delocalized wavefunction moves in opposite direction to each other, i.e., electron wavefunction moves towards acceptor site and hole wavefunction to donor site. Thus, the increased distance between the two wavefunctions reduces the exciton binding energy and hence, higher energy CT manifolds (loosely bound CT states) are populated. SED is an uphill energy process. Thermodynamically, an uphill energy reaction can occur spontaneously if the number of final states is much larger than the number of initial states. This is referred to as the entropic driving force in the literature. Since face-on orientation facilitates in generating more number of loosely bound states compared to the initial bound CT states, SED is favored due to the entropy gain. On the other hand, the parallel orientation of electron and hole wavefunction in edge-on orientation (F_8ZnPc – ZnPc on SiO_2/Si) makes the two wavefunctions pinned to the interface (see Figure 4.9a). Likewise, the free hole in ZnPc always locates closer to the acceptor crystal in ZnPc – C_{60} on Au (see Figure 4.10a) and does not favor the separation with electron. Thus, we see that the geometric constraint imposed by the edge-on orientation will have more number of tightly bound CT states than the loosely bound CT states hence, it promotes the formation of cold CT excitons.

4.5 Summary

Two distinct molecular orientation systems: face-on (F_8ZnPc – ZnPc on HOPG) and edge-on (F_8ZnPc – ZnPc on SiO_2/Si and ZnPc – C_{60} on Au) were used to investigate the exciton dissociation dynamics. Despite of the type II band alignment in all the systems, SED was observed in face-on orientation system whereas cold excitons were formed in both the edge-on orientation systems. We found the relative orientation of the electron and hole wavefunction within the CT exciton plays an important role in determining whether the hot CT exciton will dissociate into a free electron-hole pair or relax to a tightly-bound CT excitons.

It is commonly assumed that bound CT excitons either dissociate through the charge extraction from hot CT excitons before its relaxation (pathway 1 in Fig. 4.11a) or *via* the thermal activated dissociation of cold CT excitons (pathway 2 in Figure. 4.11a). Evidences and arguments centered on the "hot" pathway or the "cold" pathway exists.[78-81, 91-92] Works that observe the ultrafast formation of free carriers or the presence of hot CT states are often used as evidences to support the "hot" pathway.[93-94] On the other hand, the observation of effective charge generation with sub-bandgap photoexcitation supports the "cold" pathway.[95-97] We note that the "hot" versus "cold" argument (Figure 4.11a) is based on an intrinsic assumption that hot CT excitons always relax spontaneously into cold CT excitons (the black arrow in Figure 4.9a).

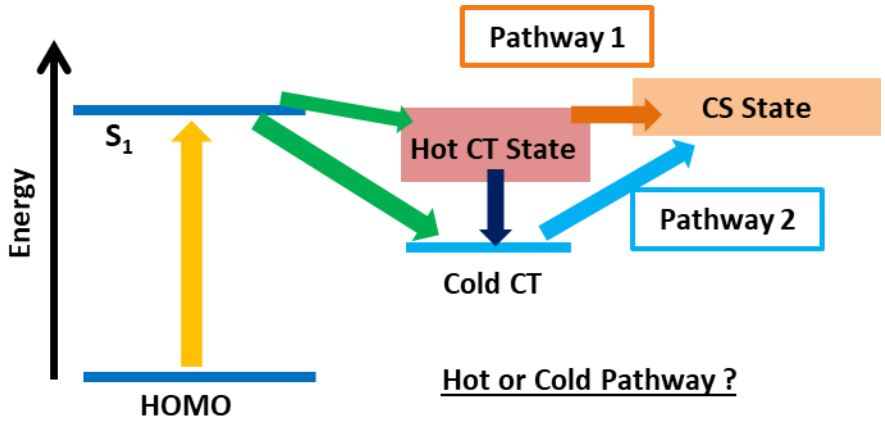

Figure 4.11: An energy level diagram illustrating the "hot" and "cold" exciton dissociation pathways that are commonly discussed in the literature. Significant efforts have been made to understand which pathway is dominant in the exciton process.

This prevalent assumption is probably originated from the Kasha's rule, which is well-known in the area of photochemistry. However, this assumption is not necessarily true because the change in entropy originated from the geometric configuration can provide the driving force to move the reaction in an energy uphill direction, i.e. the SED process. If the uphill SED is favored, it does not matter whether a hot or a cold CT state is populated initially because either of them would decompose spontaneously into free carriers. Now the question is: Which reaction direction, SED

or hot exciton cooling, dominates once the CT exciton (either cold or hot) is formed. This reaction direction can be determined by the relative orientation of the delocalized electron and hole wavefunctions, which in turn is determined by the geometric configuration of the system i.e., the molecular orientation. The relative orientation of the delocalized electron and hole wavefunctions affects the number of loosely bound or tightly bound CT manifolds, and hence the entropy. If the number of loosely bound CT states is more than the tightly bound CT states, then the entropy change would be sufficient enough to drive the reaction in uphill direction In our results, perpendicular wavefunction orientation favors this mechanism. In case of more tightly bound excitons (parallel wavefunction orientation in our case), the reaction would favor downhill direction. In brief, the exciton dissociation yield is expected to depend sensitively on the morphology of the donor-acceptor blend.

5. The Effect of Band Bending on Exciton Dissociation Dynamics at ZnPc –MoS_2 interface

5.1 Introduction

Organic – TMD heterostructures

After the discovery of graphene in 2004,[98] semiconducting TMDs have emerged as viable 2D layered materials because of their tunable optical band gap range (1.0 – 2.5 eV).[99] In addition, they have properties such as high mobility, strong spin-orbit coupling, valley selective optical pumping, and a unique property of stacking layers of different TMDs together due to their weak van der Waals interaction [100-103] however, defect free and large scale production of TMDs heterostructure is challenging. On the other hand, organic semiconductors are lightweight, flexible and excellent absorbers of light.[5-7] Their huge portfolio enables the selection of materials for a desired heterostructure configuration. Similar to the TMDs, organic heterostructures are bonded by van der Waals interaction. In addition, their band gap can be engineered[87] and the thickness can be controlled. However, diffused interface due to intermixing of molecules and their reluctant to pass charges quickly to the neighbors are its demerits. In the past few years, organic – TMDs heterostructures have emerged as a new class of hybrid system with a well-defined interface and improved transport properties.[104-105] The organic molecules can be grown on exfoliated or CVD grown TMDs either by thermal evaporation or spin/dip-coating of polymeric materials.[106] These two materials are combined *via* van der Waals interaction without the need of lattice matching in contrast to the conventional, epitaxial grown heterostructures. Furthermore, these heterostructures benefit with the advantage of both materials and even show up the new properties and functionalities, which neither material can provide.[106-109] They have

proven their successful applications in electronic devices, photonic devices, energy storing materials, photodetectors and sensors. For example, the gate tunable p-n junctions has been fabricated in a scalable form using organic – TMD hybrid heterostructures.[110-111] The increased mobility of MoS_2 has been reported by removing its defects when treated with organic molecules. [112-113] Likewise, high performance organic field effect transistior (OFETs) has been fabricated using 2D h-BN and thin films of ruberene.[114-115] Despite of such many applications organic – TMDs system is yet to be explored from a large library of organic molecules and TMDs, which can establish them as a promising flexible material in photovoltaic and optoelectronics fields.

Exciton dynamics at organic – TMD system

Because both organic and TMD semiconductors have low dielectric constant, excitons are created on these materials upon resonance optical excitation. Exciton dynamics depends on the interfacial band alignment and the morphology. In addition, it was demonstrated in Chapter 4 that geometric constrained imposed on the delocalized wavefunctions will also affect the CT excitons dynamics. Thus, the 2-D TMDs can result to a unique exciton behavior when they combine with 0-D organic molecules. Moreover, the out-of-plane electron transport in TMDs is stronger than the in-plane. For example, if TMD is excited in an organic – TMD hybrid system, where the organic molecule has face-on stacking, the delocalized electron wavefunction transports in an orthogonal direction to the interface. This would favor exciton dissociation process because there is less spatial overlapping of electron and hole wavefunctions. However, if organic molecule has edge-on orientation, delocalized electron wavefunction becomes parallel to the interface and hence exciton dissociation is less favored. Moreover, the controllability on thickness of organic molecule adds up an extra dimension to study exciton dynamics. Exciton

dynamics becomes more complicated when the spin lifetime comes into play. For example, TMDs have strong spin-orbit coupling[116-117] that can flip the spin of excited charge carrier whereas in organic materials excited charge carrier tries to remain in the same spin state for a longer time due to its weak spin-orbit coupling.

Some recent works have reported the charge transfer (CT) across the organic – TMD interfaces in an ultrafast time scale.[118-122] While these works can provide provide preliminary evidence for exciton dissociation, it assumes that the CT excitons can dissociate effectively into free electron-hole pairs after the CT event. However, various electron relaxation and recombination channels can occur prior to exciton dissociation, which can outweigh the device performance and in some cases, it does not guarantee exciton dissociation. Hence, a detail investigation of interfacial CT process that tracks subsequent evolution of energy, population and spatial size of CT excitons is critical. Understanding the correlation between these factors would allow one to design interfaces with effective exciton dissociation. On the other hand, most of the works on organic – TMD system is motivated from the prevailing notion that CT occurs in type II band alignment, which is usually confirmed from the measurements taken when participating materials are in free state (i.e., when two materials are not in contact). In general this is true however, the interfacial energetics of the system can change depending on the nature and thicknesses of the organic molecule deposited on TMDs. In particular, band bending has been observed in various heterojunctions.[123-124] The band bending changes energy landscape at the interface, which can play a crucial role in determining CT dynamics. Here we use zinc phthalocyanine (ZnPc) – MoS_2 (Molybdenum disulphide) interface as a model system to illustrate the role of interfacial energy landscape in CT and exciton dissociation process. Exciton dynamics will be compared between ZnPc – ML-MoS_2 and ZnPc – bulk-MoS_2 system. Despite

ZnPc's face-on orientation on bulk and ML, and type II band alignment at interface of both systems, they showed contrasting exciton dynamics though the ultrafast CT from ZnPc to MoS_2 occurred in both systems within sub-100fs timescale. In bulk system, the CT was subsequently followed by BET from MoS_2 to ZnPc to form triplet (T_1) excitons whereas in ML system, the CT excitons eventually separated into free charge carriers. This dissimilar dynamics for the similar system is due to the difference in the band bending (ZnPc on bulk had more band bending than that on ML) observed by our photoemission spectroscopy measurement, aided by the difference in spin lifetime of the charge carrier in ML and bulk MoS_2.[116-117, 125]

5.2 Sample Preparation, Characterization and Method

Sample Preparation and Characterization

Commercially available, high quality, CVD-grown ML-MoS_2 on SiO_2/Si was used for the study. The ML-MoS_2 layer had a continuous coverage confirmed from optical microscopy image.[126] For bulk-MoS_2, a cm-sized single crystal purchased from a commercial vendor was used. It was mounted on a Si substrate to provide the mechanical support. Before loading into the vacuum chamber, the surface of bulk MoS_2 was cleaved to expose fresh surface. Both MoS_2 samples were annealed at ~ 400°C for 12 hours in an ultrahigh vacuum chamber (UHV) with a base pressure of 1×10^{-10} Torr to outgas any adsorbed molecules on MoS_2. The quality of both samples was confirmed before ZnPc deposition. For the ML-MoS_2 sample, angle-resolved photoemission spectroscopy (ARPES) was used to characterize band structure of the material. Figure 5.1a shows 2D plot of the ARPES spectrum near Γ point. A clear band-dispersion was observed in the ARPES experiment indicating that the ML-MoS_2 has a continuous coverage, good crystallinity and a clean surface. Figure 5.1b shows the ARPES spectra at emission angles of 0° and 41°. These two emission angles correspond to the magnitude of the momentum *k*

vector at Γ and K points respectively. The plot shows the valence band (VB) edge at the K point is higher by ~ 0.06 eV than at the Γ point, which is a distinctive feature of ML-MoS_2.[127-128] The PL spectrum of the ML-MoS_2 is shown in Figure 5.1c. A single peak was observed at 663 nm, which is originated from emission of A-exciton in ML-MoS_2 and is consistent to the properties of ML-MoS_2.[129] For bulk MoS_2, low electron energy diffraction (LEED) was used to verify the surface cleanliness. Figure 5.1e shows clear diffraction pattern of the bulk MoS_2 single crystal measured by LEED prior to ZnPc deposition. Since LEED is a surface sensitive technique, the sharp diffraction pattern indicates that the MoS_2 surface is clean and has no significant molecular adsorbates. In addition, the UPS spectra show the sharp valence band edges (see next section) of MoS_2 which is in agreement with previous studies. After annealing MoS_2 samples, it was transferred *in-situ* to another UHV chamber with a base pressure of 1×10^{-9} Torr for ZnPc deposition. Quartz crystal microbalance monitored the film thickness. For thicknesses up to 4 nm, a slow deposition rate of 0.3 Å/min was used and the substrate was kept at room temperature to produce a uniform ZnPc films with molecules having a face-on orientation.[130] For films thicker than 4 nm, a faster growth rate of ~ 0.8 Å/min was applied. Ionization potential, measured form UPS spectrum, was calculated to confirm the face-on orientation of ZnPc molecules.[59-60] The IP of face-on molecules is ~ 0.5 eV higher than edge-on orientation of the same molecule. The UPS spectra near SECO and HOMO region for the 10 nm ZnPc on bulk-MoS_2 (black) and on ML-MoS_2 (red) samples are plotted in Figure 5.1d. To avoid the overlapping of these spectra, offset to the y-axis was applied. The vertical bars mark the onset position of SECO and HOMO position. Using the procedure mentioned in section 2.2, the calculated IP value is 5.14 eV and 5.28 eV for ZnPc on bulk and ML respectively. From our previous measurement, the edge-on ZnPc has IP ~ 4.7 – 4.8 eV,[56] thus we confirm ZnPc on both

MoS_2 samples has face-on orientation. In addition, the in-plane spacing between ZnPc molecules can be determined from the diameter of the diffraction ring in the LEED pattern. Figure 5.1f shows the LEED pattern for 1 nm ZnPc deposited on bulk-MoS_2 using electron beam energy of 14.2 eV. The calculated diameter of the smallest diffraction ring was found to be 13.2 Å, which agrees will with previous results of metal phthalocyanines on MoS_2.[130]

Photoemission Experiment (UPS, ARPES and TR-TPPE)

The UPS and ARPES measurement was done using He-I emission line (21.22 eV) generated from a UV discharge lamp. In UPS, the photoelectrons are collected along the normal direction to the sample surface. A detector (Phoibos 100, SPECS) measures the intensity of thus emitted electrons as a function of K.E. In ARPES, the energy and intensity of photoelectrons were measured at various emission angles. In the TR-TPPE measurement, we used a pump laser pulse (1.77 eV, 25 fs) and a probe laser pulse (4.68 eV, 65 fs). Any changes in the experimental conditions will be mentioned while discussing the experimental data. Details of the UPS and TR-TPPE technique can be found in the section 2.2 of Chapter 2.

Transient Absorption Measurement

The transient absorption spectroscopy measurement was done in collaboration with Ultrafast Laser Lab in Physics and Astronomy Department at KU. In this measurement, an 80-MHz Ti:sapphire oscillator produced ~100 fs pulses at about 840 nm. Part of this beam was focused to a BBO crystal to generate its second harmonic at 420 nm, which is used as the probe pulse. The rest of the 840-nm beam was coupled to a photonic crystal fiber to generate a broadband supercontinuum. A bandpass filter with a bandwidth of 10 nm was used to select the 710 nm component of the supercontinuum, which serves as the pump pulse. The two pulses are combined by a beam splitter and co-focused by a microscope objective lens to the sample surface

with a spot size of about 2 μm. We measured differential reflection of the probe as a function of the probe delay. The differential reflection is defined as $\Delta R/R_0 = (R-R_0)/R_0$, where R and R_0 are the reflection coefficient of the sample at the probe wavelength. To measure this quantity, the probe beam reflected by the sample was send to a silicon photodiode, whose output was detected by a lock-in amplifier. A mechanical chopper was used in the pump arm to modulate the pump intensity at about 2 kHz, for the lock-in detection. The time delay between the pump and probe pulses was controlled by changing the path length of the pump beam by using a linear stage. All measurements were performed with the sample at room temperature.

Photoluminescence Spectroscopy (PL)

The PL measurement was done in collaboration with Ultrafast Laser Lab in Physics and Astronomy Department at KU. For ZnPc on bulk-MoS_2, the PL was taken using a 1.95 eV HeNe laser. The spectra were collected by a spectrometer after removing the HeNe wavelength using a notch filter. A separate PL spectra taken under the same conditions for the respective bare substrate was subtracted from the initial measurements. The experiment was conducted at room temperature.

5.3 Experimental results and discussions

5.3.1 Energy level at the ZnPc – MoS_2 interface: ML vs Bulk

Electronic states at the interface of ZnPc – MoS_2 is crucial for charge transfer and exciton dissociation dynamics. Hence, we will first discuss the energy level alignment of ZnPc – bulk-MoS_2 and ZnPc – ML-MoS_2 obtained from UPS measurement. First, we note that ML-MoS_2 has a direct optical band gap (~ 1.9 eV) higher than the indirect band gap of their bulk counterpart (1.3 eV).[131-134] The energy of the valence band edge at Γ point increases with the number of MoS_2 layers because of the interlayer electronic coupling. Thus, the interlayer van der Waals

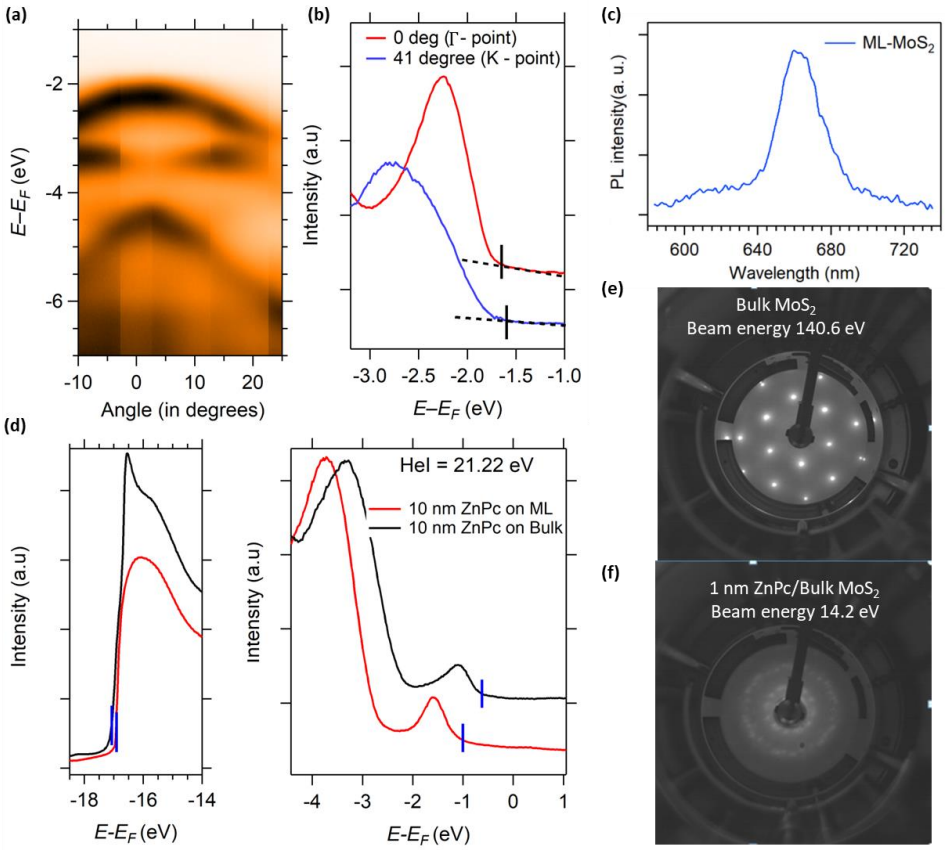

Figure 5.1: (a) ARPES spectrum for the ML-MoS_2 sample near the Γ point. (b) Comparsion of the spectra at emission angles of 0° and 41°. The two emission angles correspond to the magnitude of the momentum *k* vector at the Γ and K points respectively. (c) PL spectrum of ML-MoS_2 sample (d) UPS spectrum of 10 nm ZnPc on ML-MoS_2 (red) and bulk-MoS_2 (black) near SECO (left panel) and HOMO (right panel) region. (e) LEED pattern for the single crystal bulk-MoS_2 prior to ZnPc deposition. (f) LEED pattern for 1 nm ZnPc on MoS_2. The energies of the electron beam is shown in the figure.

interaction in bulk results to indirect transition from VBM (at Γ point) to CBM (at midway between Γ and K point). While the details of electronic band structure is out of the scope of this paper, we want to point out that VB edge at Γ point of bulk-MoS_2 is at least 0.6 eV higher than that of ML-MoS_2. The UPS spectrum of bare ML-MoS_2, bulk-MoS_2 samples and some selected thicknesses of ZnPc deposited on their top are plotted in Figure 5.2 (a) and (b) respectively. The binding energy in the UPS spectra is referenced with respect to the E_F. In the MoS_2 spectrum

(red line), the Mo-4d band (solid triangles) and the valence band edges (pink, vertical bars) can be identified.[135] For thin films of ZnPc on MoS_2, the spectral features from both MoS_2 and ZnPc are visible but MoS_2 feature slowly disappears for thicker ZnPc films while the ZnPc features become enhanced. The energy offset between the valence band edges of ML and bulk is found to be nearly 0.65 eV, which is in agreement with previous studies.[127-128] The short black vertical bars in the UPS spectrum indicate the positions of highly occupied molecular orbitals (HOMOs). A close look at the UPS spectrum shows that HOMO peak position gradually shifts away from the E_F (i.e. binding energy increases) with increasing ZnPc film thickness. We refer this shift as band bending of ZnPc's HOMO. The HOMO positions as a function of ZnPc thickness on the two systems are plotted in Figure 5.2c. The dashed in the y-axis separates the two systems for clarity. Band bending of ZnPc's HOMO is nearly 0.22 eV and 0.5 eV on ML and bulk system respectively is observed as thickness of ZnPc increases from 0.5 nm to 10 nm.

We note that both samples have similar workfunctions (ML: 4.55 eV; bulk: 4.65). Hence, a similar energy upshift (~ 0.60 eV) in their VB edges can be obtained if the energy is referenced with respect to a common vacuum level. Likewise, when ZnPc molecules are deposited on ML and bulk MoS_2, one would anticipate the energy difference (energy offset) of ~ 0.60 eV between ZnPc's HOMO and VB edge (E_{HOMO} - $E_{VB\text{-}I}$) for the two systems. However, as we will show, a very similar energy offset (in the range of 0.2 – 0.3 eV) was observed for thin ZnPc films at interface of both systems. In Figure 5.2a, the energy difference between the 0.5 nm ZnPc's HOMO (black vertical bar) and the MoS_2's VB-edge at the Γ-point (pink vertical bar) is 0.26 eV. In bulk system, the Mo-4d band shifts slightly towards E_F by nearly 0.26 eV when ZnPc films are deposited. An arrow in Figure 5.2b marks this feature. We assume that the same shift is incurred for the VB edge, although the VB edge cannot be easily identified in the 0.5 nm or the 1

nm spectra because it is obscured by the HOMO peak. With the new position of VB edge, the energy difference between this VB edge of bulk and 0.5 nm ZnPc's HOMO is 0.18 eV. Similarly, energy offsets for other film thicknesses are determined. The energy offset, E_{HOMO} - $E_{VB\text{-}\Gamma}$ as a function of ZnPc thickness is plotted in 5.2d. A very similar energy offset is observed for thin films of ZnPc despite of significantly lower VB edge at Γ point of ML (~ 0.6 eV low) compared to bulk.

Based on our results for the interfacial energetics discussed so far, similar energy offset, E_{HOMO} - $E_{VB\text{-}\Gamma}$ in both the systems for thin films and unequal band bending of ZnPc's HOMO in the two systems are the two key observations. The physical origin of the observed "pinning" in the VB-HOMO offset is not clear, but we speculate that it would be resulted from the orbital mixing between MoS_2 and ZnPc considering that the MoS_2 orbital at the Γ-point has a strong out-of-plane character.[127] Based on this offset, the band alignment for the both interfacial systems are plotted in Figure 5.2 (e) and (f). 1 nm thick ZnPc is chosen because it has the spectral features of both ZnPc and MoS_2. The energy level is referenced with respect to the HOMO of ZnPc. Positions of the conduction band minimum (CBM) are assigned based on reported transport gaps of ML and bulk MoS_2.[127, 136] The ZnPc's S_1 state is measured from the TR-TPPE and is at 1.74 eV above its HOMO peak. Both ML and bulk MoS_2 interfacial system show type-II band alignment, which is consistent with other reports on the metal-Pc – ML-MoS_2 interface.[137-140] However, the S_1 – CBM energy offset is lesser in ML system compared to the bulk system. The other key difference is; there is a much stronger band bending in the ZnPc film deposited on bulk-MoS_2 than on ML-MoS_2. Earlier we discussed that ZnPc molecules have a face-on orientation on MoS_2. For this orientation, our previous studies[61] found that the position of the HOMO peak is in the range of 1.2 – 1.5 eV below the E_F and the workfunction is in the

range of 4.3 – 4.5 eV. For the ZnPc – bulk-MoS_2 interface, the aforementioned energy offset "pinning" would make the E_F of ZnPc much higher than that of bulk-MoS_2. Thus, ground state electron transfer from ZnPc to bulk-MoS_2 needs to occur in order to produce the observed energy level alignment. The expected ground state electron transfer is indeed consistent with the strong band bending observed in ZnPc deposited on bulk-MoS_2. The direction of the band bending indicates that net positive charges are accumulated in the ZnPc layer.[141] The different amount of the band bending and S_1 – CBM offset for ZnPc – ML-MoS_2 and ZnPc – bulk-MoS_2 interfaces should have a strong influence on the CT and exciton dissociation dynamics.

The type II band alignment of ZnPc – MoS_2 heterostructure and the face-on orientation of ZnPc molecules should facilitate the CT of optically excited electron from ZnPc's S_1 state to the CBM of the MoS_2 crystal. To verify the occurrence of CT from ZnPc to MoS2, we did PL measurements for 2 nm ZnPc film grown on SiO_2 /Si and MoS_2 substrates. In the PL experiment, an excitation wavelength of 633 nm (∼1.96 eV) was used. The PL spectra for the two samples are shown in Figure 5.2g. For the ZnPc on the SiO_2/Si sample, a PL peak at ∼ 680 nm (yellow trace) is observed, which corresponds to the energy of the ZnPc's S_1 exciton. However, the peak disappears for ZnPc – MoS_2 interface (blue trace). Because the ultrafast CT at the ZnPc − MoS_2 interface can quench the S_1 population in ZnPc, it results to the disappearance of the PL peak. Results show that the PL intensity is quenched at least by a factor of 10 in the ZnPc−MoS2 sample.

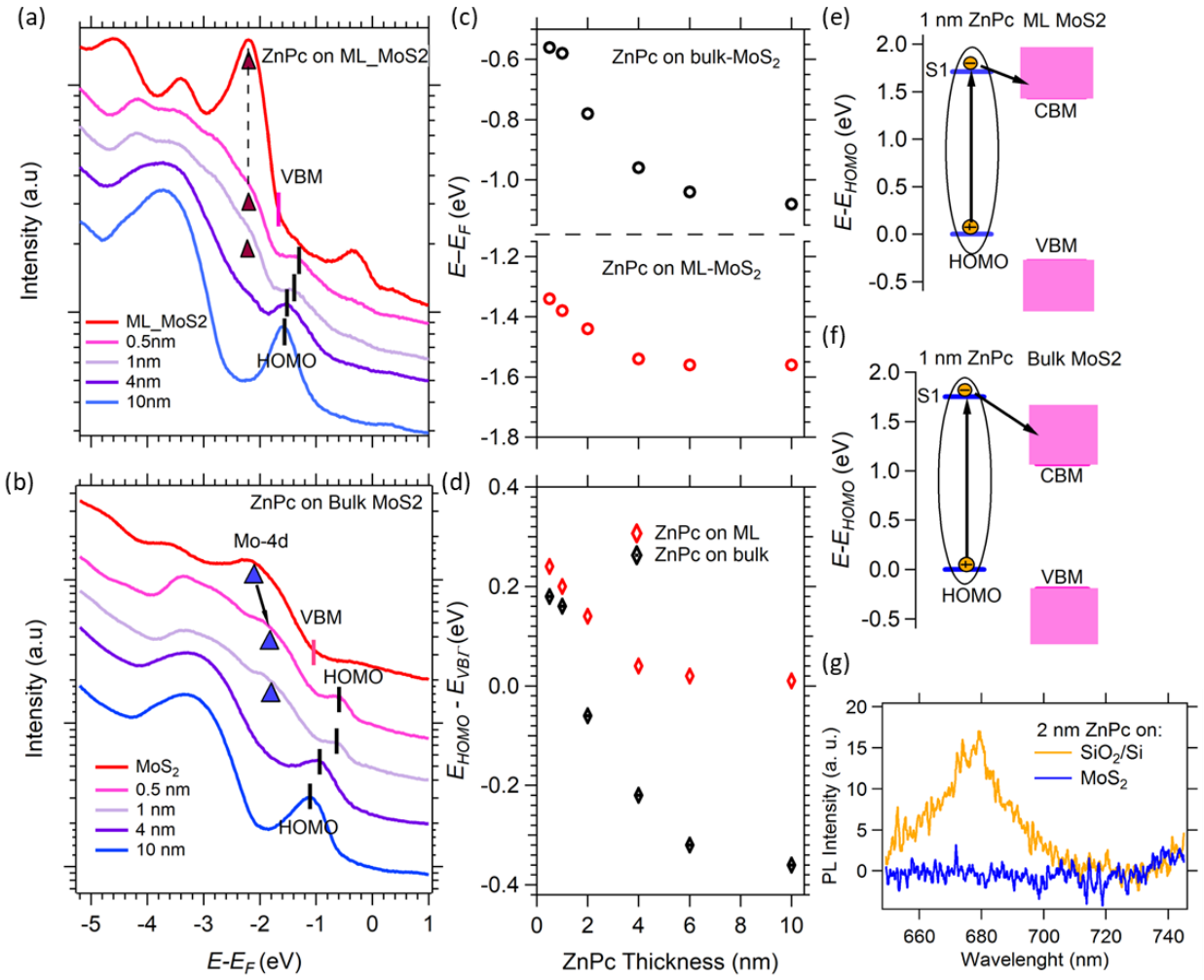

Figure 5.2: UPS spectra for the bare MoS_2, and varying thicknesses of ZnPc on (a) bulk-MoS_2 and (c) ML-MoS_2. The solid triangles and the red vertical bar represent the MoS2's Mo-4d band and VBM, respectively. Blue vertical lines indicate the position of the ZnPc's HOMO. Energy level diagram at the (e) ZnPc – ML- MoS2 and (f) ZnPc – bulk- MoS2 interface. (g) PL spectra for 2 nm ZnPc films grown on SiO_2 (300 nm)/Si and MoS_2 substrates.

5.3.2 Charge transfer, spin flipping and back electron transfer on ZnPc – bulk MoS_2

TR-TPPE measurements were performed to study the interfacial CT dynamics. A pump pulse, with a photon energy centered at 1.77 eV chosen to match the S_1 energy of ZnPc, is used to excite the sample and a probe pulse of 4.68 eV ionized the excited signals. Figure 5.3a,b shows the TR-TPPE spectrum for 1 nm ZnPc deposited on bulk-MoS_2 on two different timescales. The pseudocolor represents the intensity of the photoemitted signals. The energy

level is referenced with respect to ZnPc's HOMO. In Figure 5.3a, a peak at $E\text{-}E_{HOMO}$ ~ 1.75 eV can be found at the temporal overlap of pump and probe pulses (t = 0). This energy agrees with the S_1 energy measured by optical absorption spectroscopy.[65] Hence, it is assigned to the optically excited S_1 state in ZnPc. This state has a very short lifetime (< 100 fs). This CT time is comparable to those found in organic-graphene interfaces.[142-143] As we will explain, the disappearance of the S_1 signal can be attributed to the CT from ZnPc to MoS_2. At larger delay times (Figure 5.3b), a peak at lower energy regime ~ 1.15 eV emerges in the spectrum. Later we will show the intensity of this peak continues to rise for a few hundreds of ps timescale. Since this peak is long-lived and ZnPc's has a T_1 state at ≈ 1.1 eV above HOMO,[144] this peak is assigned to the ZnPc's T_1 state. The T_1 state can be populated by spin-flipping and subsequent back electron transfer (BET) from MoS_2 to ZnPc. Spin-flipping would occur more rapidly in MoS_2 than in ZnPc because of the strong spin-orbit coupling in MoS_2. In ZnPc, the timescale for $S_1 - T_1$ transition is on the order of 100 ps to 1 ns.[145]

Similar S_1 and T_1 dynamics were observed for 0.5 nm. However, for thicker ZnPc films, these interfacial dynamics were less pronounced. For 10 nm thick ZnPc film (Figure 5.3c) neither quick S_1 signal decay nor T_1 intensity rise were observed. Instead, the lifetime of the S_1 state is much longer than that observed in the 1 nm sample. Because photoemission is a surface sensitive technique, only excitons near the surface region are probed. In the 10 nm ZnPc sample, excitons need to diffuse to the ZnPc-MoS_2 interface before CT can occur at the deeper interface. The time needed for the exciton to diffuse a distance of ~ 10 nm is rather long (> 100 ps)[71]. Therefore, the TR-TPPE spectrum for the 10 nm sample essentially represents the exciton dynamics of a standalone ZnPc and its longer S_1 lifetime suggests that fast decay in thin film originates from the CT at the interface. Furthermore, 1 nm ZnPc grown on SiO_2/Si substrate does

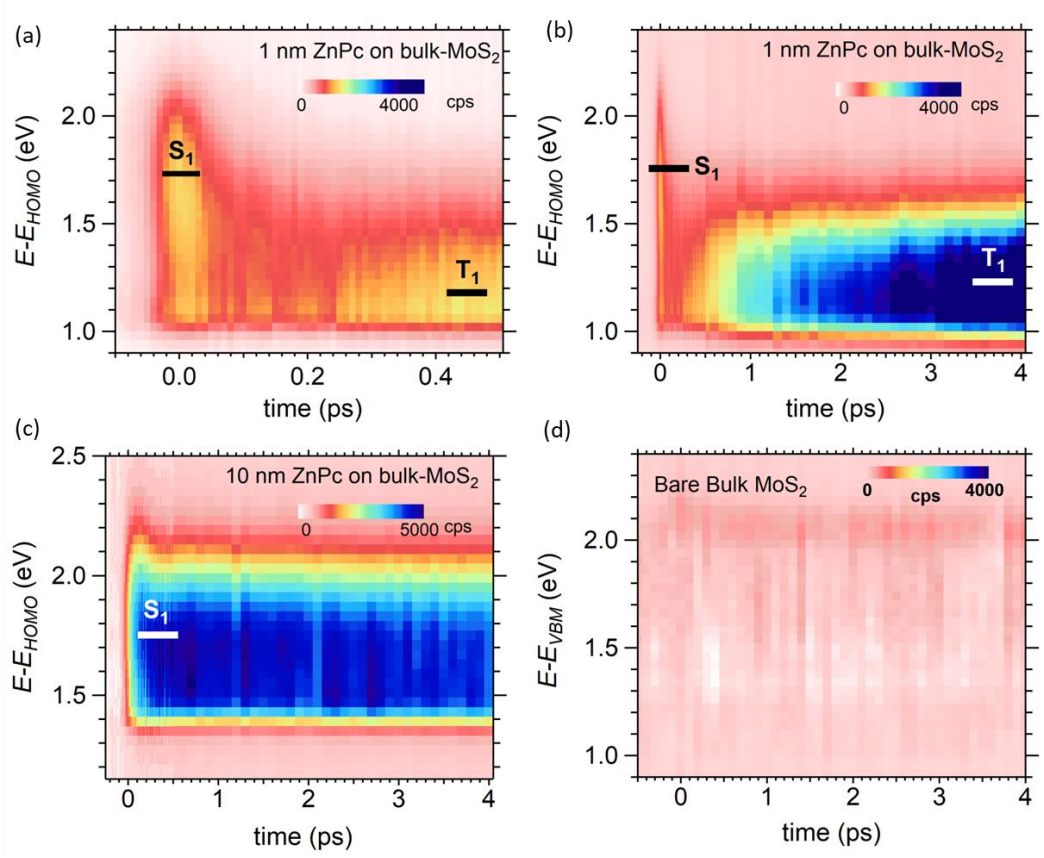

Figure 5.3: (a, b) TR-TPPE spectrum of the 1 nm ZnPc on MoS2 sample at two different time-scales. TR-TPPE spectrum of (c) 10 nm ZnPc on MoS2 and (d) bare MoS2. "Figures (b, c and d) adapted from reference [146].[146] Copyright (2017) American Chemical Society."

not show quick decay of S_1 signal (see Figure 5.4c in next section) because CT is not expected at the interface of ZnPc – SiO_2/Si. It has a lifetime similar to that of 10 nm ZnPc – MoS_2. On the other hand, controlled experiment was performed on bare bulk-MoS_2. The pump-induced signal (Figure 5.3d) from MoS_2 was below the noise level to be detected. We propose two possible reasons for the weak TPPE signal from the MoS_2 crystal. First, the CBM in MoS_2 is located at the K point in the *k*-space and requires large probe photon energy to fulfill the momentum conservation (~ 10 – 20 eV) and photoionize electrons residing near the K point *via* a direct optical process.[147] In our experiment, probe photon energy was 4.68 eV. Hence, the excited electrons in MoS_2 can only be ionized *via* indirect processes that involve the emission or

absorption of phonons, which have much weaker ionization cross-sections. Second, although the bulk MoS_2 has an indirect bandgap of 1.3 eV, the absorption coefficient is much smaller due to the indirect nature of the bandgap. The minimum energy needed for direct optical transition is ~ 1.85 eV,[129, 148] which is larger than our pump photon energy (1.77 eV). Therefore, the concentration of optically excited electrons in MoS_2 is expected to be much smaller than that in ZnPc. For the ZnPc – MoS_2 sample, the first factor, i.e. the weak TPPE signal from excited electrons in MoS_2, explains the rapid decay of the photoemission intensity when the optically-excited electron transfers from ZnPc to MoS_2. The second factor suggests that the pump excites ZnPc primarily and the observed signal should be dominated by the excited electrons originated from the ZnPc layer. These all observations support our claim that that the decay of the S_1 intensity observed in the thin ZnPc samples (Figure 5.3a,b) is originated from the interfacial CT rather than the intrinsic property of the ZnPc or MoS_2 alone.

To further understand the details of the CT and $S_1 – T_1$ transition dynamics, the TPPE spectra for the 1 nm sample at some representative delay times are plotted in Figure 5.4a. At t = 0 ps, it is found that the S_1 peak of ZnPc is populated upon optical excitation. The S_1 population decays with a sub-100 fs time constant, as evidence by the disappearance of the S_1 peak in the time 0.1 ps spectrum. The decay of the S_1 state can be attributed to the CT from ZnPc to MoS_2. At t ~ 0.3 – 0.5 ps, the signal intensity reaches global minimum with a slight hump at ~ 1.5 – 1.6 eV (blue spectra). We refer this as CT state, where the excited electrons reside in MoS_2 layer. The low intensity of the CT feature is consistent with our earlier argument of the indirect optical band gap and the need of large probe energy for photoionization of electrons from the MoS_2 layer. As we will show, the intensity at low energy ~ 1.15 eV, T_1 state, continues to grow, but at

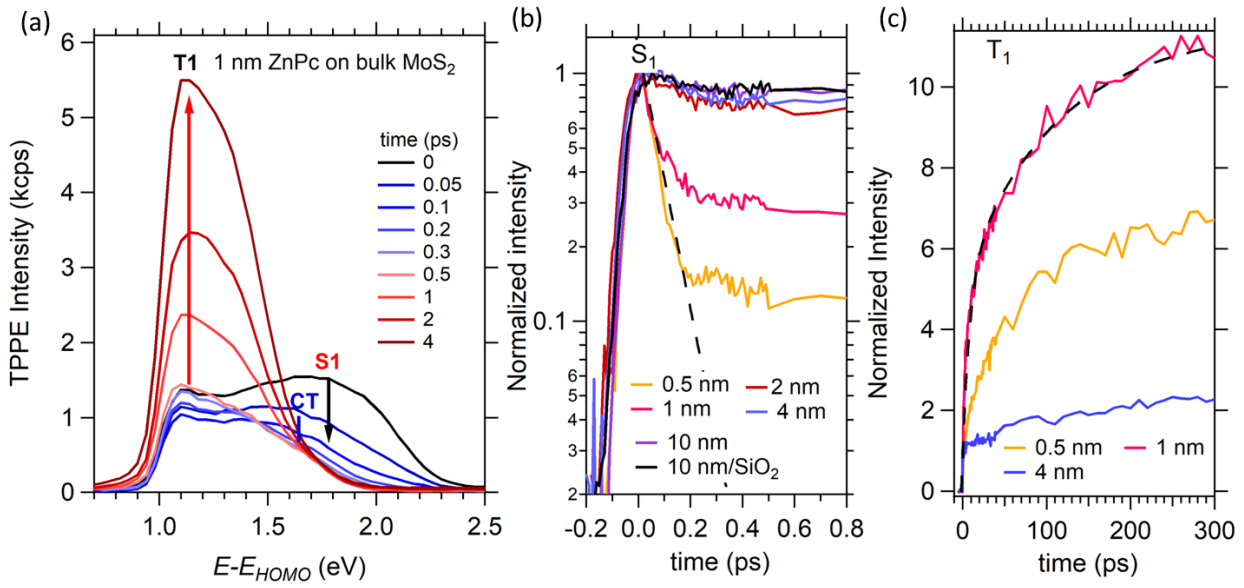

Figure 5.4: (a) TPPE spectra at selected delay times for the 1 nm ZnPc on MoS_2 sample. (b) Temporal evolution of the intensity of the S_1 state for different ZnPc thicknesses. The fast intensity decay in the thinner samples (0.5 and 1 nm) is attributed to CT to MoS2. An exponential fit (dashed line) shows a decay time of 80 fs. (c) Temporal evolution of the intensity of the T_1 state for different ZnPc thicknesses. For the 1 nm sample, the intensity rise is fitted with a biexponential function (dashed line). Time constants of 2.7 and 81 ps are found. "Figures (b, c) adapted from reference [146].[146] Copyright (2017) American Chemical Society."

a slower rate, on the 10 – 100 ps timescale. As mentioned earlier, the T_1 state can be populated by BET from MoS_2 to ZnPc after the spin of the electron is flipped in MoS_2. The energy of the assigned CT state is ~ 0.3 eV higher than the CBM of MoS_2 (Figure 5.2f). It is known that hot carrier relaxation is rather slow in bulk MoS2 (about ~10 ps). At t ~ 0.3−1 ps, it is likely that the transferred electron in MoS_2 has not fully relaxed to the CBM after the initial CT process. Moreover, a recent theoretical calculation shows that the binding energy of CT excitons at organic−TMD interfaces is rather weak (<40 meV).[149] Exciton binding is not likely to lower the electron energy significantly.

The temporal evolution of the normalized photoemission intensity of S_1 state for various ZnPc thicknesses is plotted in Figure 5.4b. For thin (0.5 nm, 1 nm) ZnPc samples, the initial

rapid decay is attributed to CT to MoS_2. An exponential fit yields a decay time of 80 fs (dashed line). For thicker samples (4 nm and 10 nm), the excitons in the surface region must diffuse to the interface before CT can occur. As mentioned earlier, incoherent exciton, diffusion to the interface occurs on a much longer time-scale. Therefore, the rapid decay originated from the CT is not observed for these thicknesses. Indeed, for these thicker ZnPc samples, the dynamics closely resembles to those found in the ZnPc layer deposited on a SiO_2/Si substrate (black curve). No CT is expected at the ZnPc/SiO_2 interface. Therefore, the results from the ZnPc – MoS_2 samples with a thick ZnPc layer essentially represent the exciton dynamics in a standalone ZnPc film.

Figure 5.4c shows the temporal evolution of the intensity around the T_1 peak for different ZnPc thicknesses. The intensity is normalized by the intensity at $t \sim 0$ ps. We note that the T_1 intensity is not zero near time zero because the signal is contributed from the broad spectrum of S1 state. For all samples, the T_1 intensity continues to grow up to the longest time (300 ps) that is accessible by our setup. The rise times determined from a bi-exponential fit (dashed line) to the 1 nm data are 2.7 ps and 81 ps. The bi-exponential rise would be originated from the formation of a manifold of CT states with different delocalization sizes[55, 150] and each of these CT states has different BET kinetics. Another possible cause for the multiple rise times would be the dependence of the spin relaxation time on the spin direction.[151-152] Theoretical models show that for monolayer MoS_2, the out-of-plane spin relaxation time is an order of magnitude larger than the in-plane spin relaxation time. The calculated spin relaxation times for in-plane (a few ps) and out-of-plane (10s of ps)[152] are also consistent to our measured rises times. A strong T_1 intensity is observed in the 0.5 nm and 1 nm sample. The intensity becomes much weaker for the 4 nm sample. In the 4 nm spectrum, a major portion of the intensity is contributed by the S_1 state

because of the spectral overlapping with the longer-lived S_1 state. Again, because photoemission is a surface sensitive probe, any T_1 excitons formed at the interface must diffuse to the surface before it can be detected. Triplet diffusion is a rather slow process, which justifies a weak T_1 intensity observed in the 4 nm sample. For the 10 nm sample, we do not observe a clear T_1 intensity that emerges from the spectrum (Figure 5.3c).

Pump fluence dependence T_1 dynamics

In order to understand the BET and the triplet formation process, the temporal evolution of the T_1 intensity was measured for different pump fluences. In the BET process, if the original electron-hole pair in a S_1 exciton recombines to form the T_1 exciton (germinate recombination), the process is first-order and the kinetics should be independent of the pump fluence. On the other hand, if an electron excited independently in MoS_2 transports to the interface and combines with the residue hole in the ZnPc (non-germinate recombination), the process is second-order and the kinetics should depend on the pump fluence. Pump laser fluences of 4.4, 14 and 42 μJ cm^{-2} are used to study the triplet formation dynamics in the 1 nm-ZnPc sample. The intensity is normalized so that the kinetics can be compared. The kinetic traces for different fluences are shown in Figure 5.5. We found that the kinetics is almost identical for different pump fluences. The inset in Figure 5.5 plots the actual 2PPE intensity at t = 200 ps as a function of the pump laser fluence, which shows a linear dependence. This behavior indicates that the triplet formation is a first-order process, which is presumably due to germinate recombination.

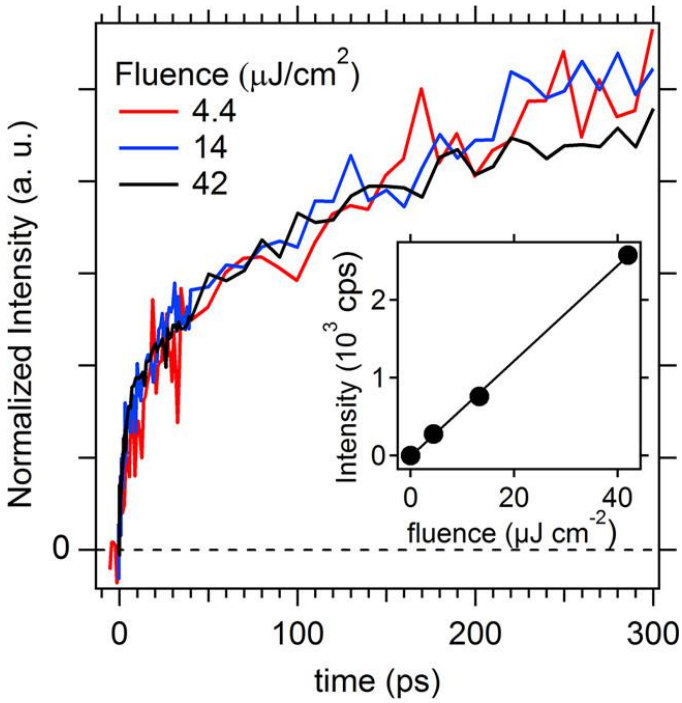

Figure 5.5: The normalized intensity evolution of the T_1 state for the 1 nm ZnPc sample. Three different pump laser fluences are used. The kinetics is essentially independent of the pump fluences. The inset shows the actual TPPE intensity at 200 ps as a function of the laser fluence. A linear dependence was found. "Figure reproduced from reference [146].[146] Copyright (2017) American Chemical Society."

Here we summarize our findings on ZnPc – bulk-MoS_2 interface. There is ultrafast CT, within sub 100 fs, from ZnPc to MoS_2. After CT, the electron-hole pair does not fully dissociate into free carriers instead, they form a bound CT exciton at the interface. The spin of the transferred electron is flipped in MoS_2. After the spin-flipping, the BET becomes energetically feasible via the formation of a triplet excitons in ZnPc. Note that if the CT exciton dissociates before the BET, the hole in ZnPc and the electron in MoS_2 that form the triplet exciton will be independent from each other. In this case, the BET will be a second-order non-germinate process, which is inconsistent to the measured fluence dependence.

5.3.3 Charge transfer and free charge carrier generation at ZnPc – ML MoS_2

As discussed earlier in section 5.3.1, ZnPc – ML-MoS_2 interface has a type II band alignment, which should allow ultrafast electron transfer from ZnPc to ML-MoS_2. In addition, the face-on orientation of ZnPc on ML-MoS_2 (see section 5.2) would facilitate the CT process. The experimental conditions for ZnPc – ML-MoS_2 system was kept similar to ZnPc – bulk-MoS_2 system. Figure 5.6 (a) and (b) are the TR-TPPE spectrum of a 1 nm ZnPc – ML-MoS_2 sample at two different timescales, obtained with pump beam energy centered at energy 1.77 eV that resonantly excited the ZnPc sample.[65] The energy of excited states (vertical axis) is referenced with respect to the ZnPc's HOMO position determined from our UPS experiment. The pseudocolor represents the pump-induced photoemission intensity. At delay time $t \approx 0$ ps, a peak at ~1.75 eV is observed similar to ZnPc – bulk-system. We attribute this peak to the S_1 state of ZnPc because the peak position agrees well with the energy of the S_1 exciton. Another peak located at ~ 0.2 eV below the S_1 peak can be found in the spectrum within 0.1 ps. These peaks are more apparent in the energy spectrum plotted in Figure 5.7a. Details on the CT states will be discussed later. On further increasing the probe delay time, we observe the intensity rise at lower energy (~1.20 eV) upto a few ps (~2 ps) and then it almost dies within the next few tens of ps. Since this state evolves after the relaxation of CT_h state, we label it as CT_0 state, a localized CT exciton state.

Figure 5.7b shows the time dynamics of S_1 state for various thicknesses of ZnPc films. The S_1 lifetime obtained from a single decay exponential fit for 1 nm ZnPc is 70 fs. The S_1 signal decays quickly for other thin films (0.5 and 2 nm) a well. The short lifetime of the S_1 signal can be attributed to the CT from ZnPc to MoS_2.[120, 142] We note that the decay of these signals are not originated from excitons in ML-MoS_2 because in a control experiment conducted on the bare MoS_2 sample, TR-TPPE signal was below the noise level (Figure 5.6d). This is reasonable

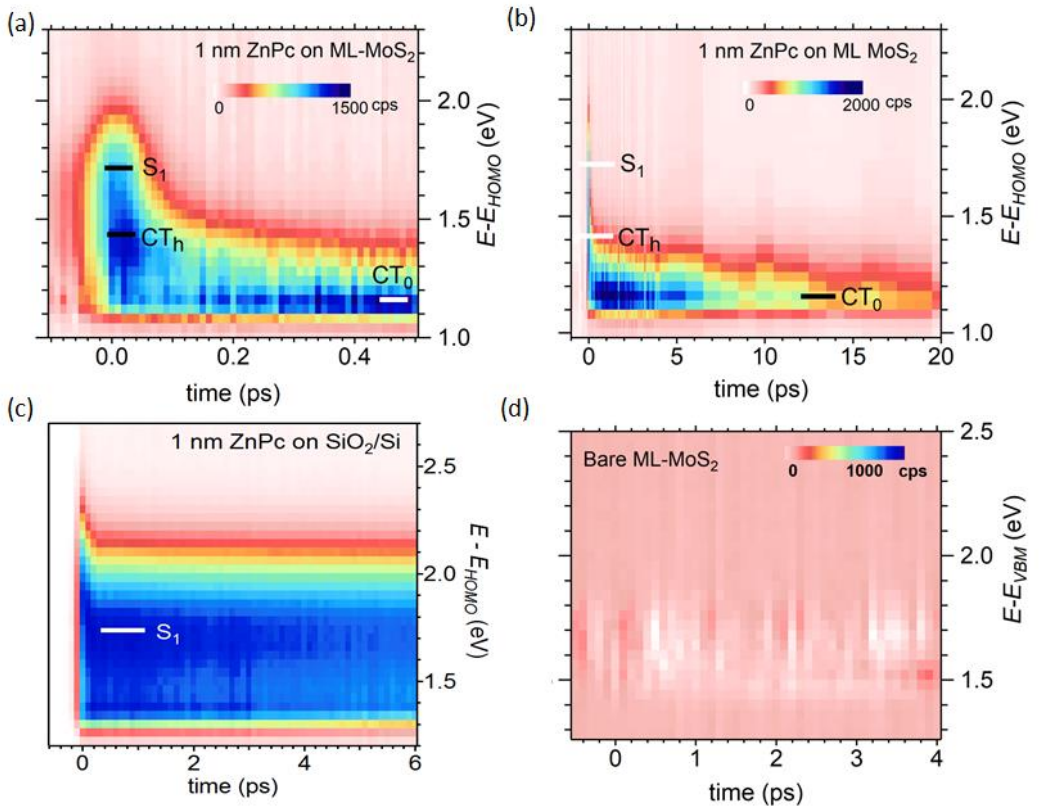

Figure 5.6: (a, b): TR-TPPE spectrum of the 1 nm-ZnPc–ML-MoS_2 sample at two different timescales. The pump beam excites the ZnPc film selectively and the interfacial CT exciton is produced by electron transfer from ZnPc to MoS_2. (c) TR-TPPE spectrum of the 1 nm-ZnPc–SiO_2 and TR-TPPE spectrum of bare ML-MoS_2.

because the pump photon energy is less than the optical band gap of ML-MoS_2. Furthermore, in section 5.3.1 we explained that electrons resided in the k-valley of ML-MoS_2 needs a large photon energy (10 – 20 eV) to ionize the electrons via direct optical process and our probe energy is only 4.68 eV. Measurement on 1 nm ZnPc on SiO_2/Si (Figure 5.6c) was also taken to confirm that the decay of S_1 signal in Figure 5.6 (a) and (b) is the characteristic of ZnPc – ML-MoS_2 interface. As expected, a longer lifetime of S_1, similar to ZnPc standalone, was observed because ZnPc – SiO_2/Si interface does not favor charge transfer. In absence of charge transfer, S_1 signal decays slowly via relaxation and recombination channels that occur at a sufficiently long timescale (ps–ns timescale). Thick films of ZnPc exhibits the S_1 dynamics similar to ZnPc

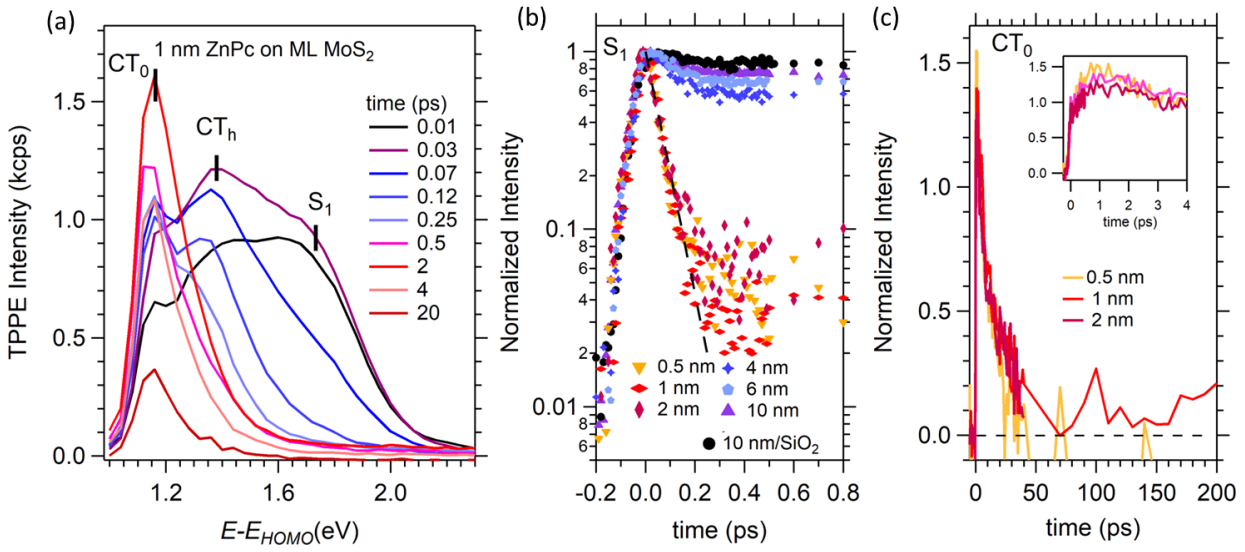

Figure 5.7: (a) TPPE spectra of 1 nm ZnPc – Ml-MoS_2 at some selected pump-probe delay times. The positions for the S_1, CT_h and CT_0 states are shown with black vertical bars. (c) The normalized intensity dynamics of the S_1, and CT_0 states as a function of time.

standalone for the reasons explained in section 5.3.1 (see Figure 5.3d). This is evident from the plot of S_1 dynamics in Figure 5.7b. The S_1 dynamics for the ZnPc films greater than 4 nm are similar to standalone ZnPc film (black trace).

The TR-TPPE energy spectra in Figure 5.7a show a peak at ~ 1.44 eV that rises in intensity at a time slightly slower than S_1 state but has a comparatively longer lifetime. However, we observed the decay of this signal within 0.5 ps (blue trace). As a convention, we assign this state to a hot charge transfer state (CT_h) since it is immediately populated and has a shorter lifetime. The CT_h state can be originated from the CT from ZnPc to MoS_2, hence the electron resides in MoS_2. The energy of this state is ~ 1.7 eV above the MoS_2's VBM (1.44 eV with respect to the ZnPc's HOMO). This energy is slightly lower compared to the A-exciton energy of ML-MoS_2 (1.87 eV), but it is within our experimental uncertainty (~ ± 0.1 eV). In our experiment, error would be introduced in determining the relative energy position of the HOMO (in the UPS spectrum) and the excited state (in the TPPE spectrum) because different light

sources used in the two experiments would introduce different sample charging conditions. The slightly lower energy of the CT exciton indicates that it would have a larger binding energy as compared to the A-exciton of MoS_2, which can be resulted from the more localized nature of the molecular orbit. Finally, a CT_0 state at $E - E_{HOMO} \approx 1.20$ eV can be found, which clearly shows a delayed population rise. This state can be populated from the relaxation of the CT_h state. Though the energy level of the CT_0 state agrees with that of T_1 state in ZnPc – bulk-MoS_2, one striking difference is that CT_0 states are not long-loved. The CT_0 intensity rises for 2 ps, then it gradually decays and almost vanishes within 20 ps (red traces). Figure 5.7c is the temporal dynamics of CT_0 state for thin films of ZnPc (0.5, 1 and 2 nm). The inset figure shows the same temporal dynamics at a shorter timescale. An increase in the intensity is observed for 2 ps and for all the films and slowly it vanishes within ~ 20 ps. The lower energy state, $CT_{0,}$ is not observed for thicker films similar to T_1 state in bulk-MoS_2 system because these dynamics occur at the deep interface and photoemission technique is surface sensitive. We think of two possible scenarios for the disappearance of the CT_0 signals; first, the recombination of electron and hole could occur such that there are no excited signals to be detected. However, the exciton recombination time is in the range of ps-ns scale for ZnPc observed from our previous studies. Second, the exciton dissociation must occur such that free electrons reside at K valley in the momentum space. Since our probe pulse energy is low to detect these electrons in MoS_2 and is insensitive to holes in ZnPc, the CT_0 signals must have disappeared. In the following section, we will discuss the technique applied to investigate the missing signals.

Evidence of free charge carrier generation

To distinguish the above two scenarios, another time-resolved probe is used to detect long-lived excited states that may have been missed out by the TR-TPPE experiment. Transient

absorption measurement is done on the 2 nm ZnPc – ML-MoS_2 sample to find out whether long-lived states exist. In this experiment, the sample is pumped at 710 nm (1.75 eV, similar to the

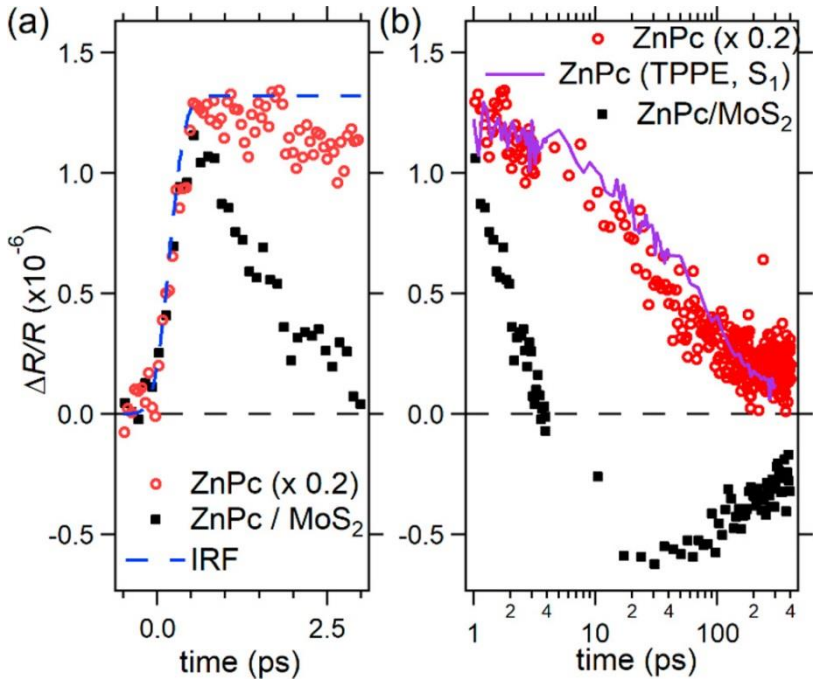

Figure 5.8: Transient absorption of the 2 nm ZnPc–ML-MoS_2 and 10 nm ZnPc samples measured at 420 nm. The samples are pumped at 710 nm, which selectively excites the ZnPc's S_1 exciton. For comparison, the signal for the standalone ZnPc sample is divided by 5 to account for the difference in the ZnPc film thickness. Panel (a) and (b) show the dynamics on two different timescales. In panel (b), the S_1 peak intensity of the standalone ZnPc sample measured by the TR-TPPE experiment (solid line) is shown for comparison. "Figure reproduced from reference [126].[126] Copyright (2019) American Chemical Society."

pump wavelength used in the TPPE experiment) and the transient change in reflectance at 420 nm was measured. Details of the experimental set-up can be found in the section 5.2 of this chapter. The pump photons selectively excite ZnPc and no significant signal was observed in the bare ML-MoS_2 sample. The choice of the probe wavelength was limited by the experimental set-up. Nevertheless, this probe wavelength can detect excitation in both ZnPc and MoS_2. In Figure 5.8, the transient change in the reflectance ($\Delta R/R$) for the ZnPc – ML-MoS_2 sample is shown (solid square, black), which is compared to the data obtained from a 10 nm ZnPc/SiO_2/Si sample (open circle, red). For comparison, the signal from the ZnPc-only sample is divided by a factor

of 5 to account for its larger thickness. The positive signal in both traces indicates that the signal was originated from the ZnPc layer, which can be attributed to the photobleaching of the ZnPc's B-band (an increase in *R* can be resulted from a decrease in absorption). The measured dynamics for the standalone ZnPc sample is comparable to the S_1 exciton population in the same sample measured by TR-TPPE (solid line).

For the ZnPc – ML-MoS_2 sample, the positive signal decreases rapidly in the first 1 – 2 ps, which is consistent to the annihilation of the S_1 exciton *via* ultrafast CT discussed above. Then, the signal changes to negative after a few ps. The magnitude of this negative signal decays on a 100 ps timescale. First, we note that the decay time of the positive signal is similar to that of the CT_0 population observed in the TR-TPPE experiment (Figure 5.7c). Following the decay of the positive signal, a long-lived negative signal appears at $t \sim 20$ ps. We attribute the long-lived negative signal to the population of electrons in ML-MoS_2 resulted from the dissociation of CT excitons. The time for CT exciton dissociation corresponds to the disappearance of CT_0 signal in TPPE (Figure 5.7c). Since, the probe photon energy is close to the C-exciton resonance of MoS_2,[153] the signal is originated from the change of C-exciton resonance by the separated electrons. The decay time of several 100 ps is also consistent with lifetime of electrons in MoS_2 when they are spatially separated from holes by a vdW interface in TMDC heterobilayers[154-155]. Based on both the transient absorption and the TR-TPPE measurements, we conclude that the CT_0 exciton does not recombine. Instead, they dissociate into free electrons in MoS_2 and holes in ZnPc.

5.3.4 Interfacial electron dynamics from energetics perspective: Bulk vs ML system

In general, the excited particle (electron) has a tendency to follow the energy path that requires minimum expense of its energy, in analogous to a hiker choosing his path based on the

height contour map. Hence, the energy position of electronic states at donor – acceptor interface could direct the local pathway of electron. In this section, we will compare our earlier results on electron dynamics between bulk and ML system from the perspective of energy landscape at the ZnPc – MoS_2 interface. Further, we will deduce the coherent size of excitons therefrom.

CT dynamics/ S_1 dynamics

At first, we would like to reiterate that the ZnPc-HOMO – MoS_2-VB-edge offset is similar for thin ZnPc films despite of energy difference more than ~ 0.6 eV between the VB-edges at Γ point of ML and bulk MoS_2. We also observed increased band bending of ZnPc's HOMO in bulk system (see section 5.3.1 for more detail). To visualize the effect of the interfacial energetics on the electron dynamics, the HOMO – VB-edge offset is replotted (Figure 5.9a). In the previous section of this chapter, we reported that electron transfer from ZnPc (thin films) to MoS_2 occurs at sub-100fs timescale for both ML and bulk systems, which is consistent with the similar HOMO – VB-edge offsets for thin films, 0.5 and 1 nm (see Figure 5.9a). However, when the ZnPc film becomes thicker (see Figure 5.9b), we find that there is a subtle difference in the spatial range of the CT, i.e. the distance from the interface at which the ultrafast CT would still occur. The temporal evolution of the normalized S_1 peak intensity for ZnPc – ML-MoS_2 and ZnPc – bulk MoS_2 samples with various ZnPc film thicknesses have been shown in Figure 5.4b and 5.7b respectively. As the ZnPc thickness is increased to 1 – 2 nm, the S_1 peak intensity starts to show a slower decay for the bulk-MoS_2 samples. By contrast, the decay dynamics is independent of thickness (in the range of 0.5 – 2 nm) for the ML-MoS_2 samples. This suggests that the ZnPc's S_1 exciton size is at least 2 nm in ML but smaller in bulk-MoS_2. Figure 5.9b illustrates this concept where ultrafast S_1 quenching is shown for thin films but for thicker samples S_1 excitons near the ZnPc surface need to transport to the interface *via*

incoherent diffusion, hence it takes has a longer S_1 decay time. Eventually, the S_1 decay dynamics is thickness-independent when the thickness is beyond 4 nm for both samples.

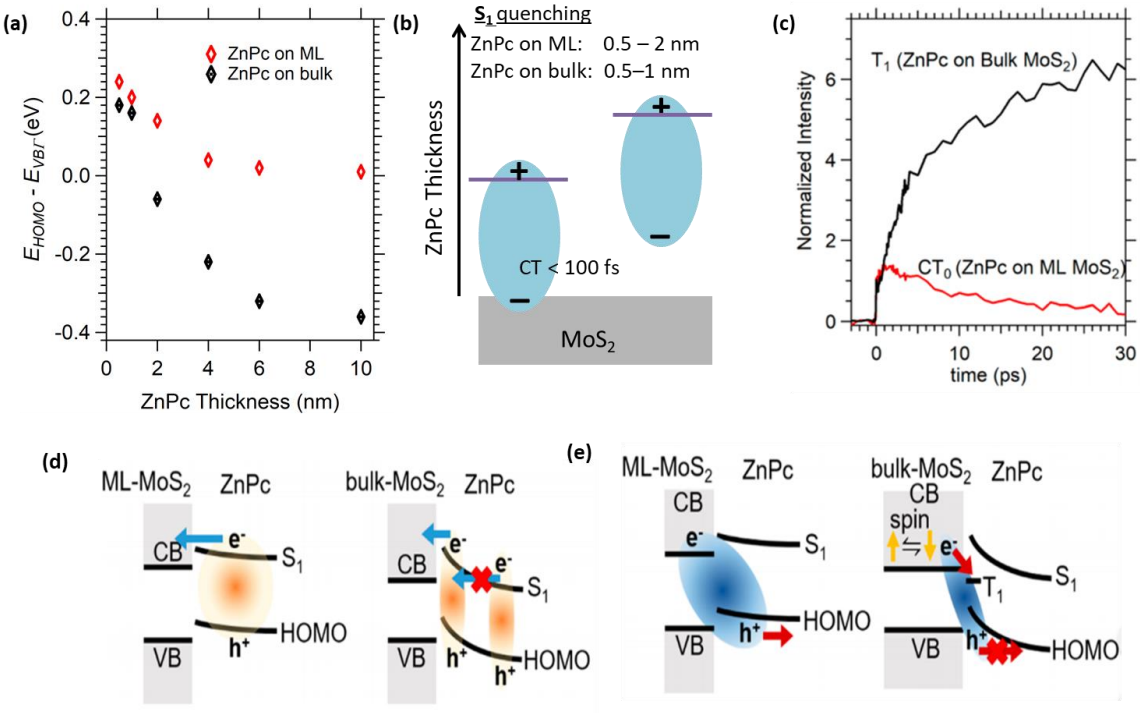

Figure 5.9: (a) The HOMO – VB-edge offset as a function of ZnPc thickness. (b) A schematic diagram to determine the coherent size of S_1 exciton in ZnPc – MoS_2 interface based on S_1 dynamics. (c) The temporal evolution of the intensity for the CT_0 and T_1 states in the 1 nm ZnPc – ML-MoS_2 and the 1 nm ZnPc – bulk-MoS_2 samples respectively. (d) A schematic diagram shows that a large band bending in ZnPc on bulk MoS_2 can limit the extent of exciton delocalization and prohibit electron injection. These two factors limit the spatial range of the coherent CT. (e) Large band bending in ZnPc on bulk MoS_2 can trap the hole of the CT exciton near the interface. The hole trapping together with the faster spin flipping rate in bulk-MoS_2 favor back electron transfer (BET) and T_1 formation at the ZnPc/bulk-MoS_2 interface. "Figures (a, c, d, and e) reproduced from reference [126].[126] Copyright (2019) American Chemical Society."

The thickness sensitive S_1 decay dynamics is directly related to the difference in the delocalization size, which can be correlated to the amount of band bending found in the UPS measurement. For the ZnPc – bulk-MoS_2, the amount of the band bending (> 0.5 eV, Figure 5.9a) is larger than the electronic coupling between neighboring phthalocyanine molecules (~0.1 eV)[156-157]. This uneven energy landscape would limit the coherent size of the S_1 exciton. The key

differences between the two interfaces are summarized schematically in Figure 5.9d. The steeper curves for ZnPc's HOMO and S_1 states indicate more band bending and uneven energy landscape. For ZnPc – bulk-MoS_2, a S_1 exciton slightly farther away from the interface cannot transfer its electron coherently to the MoS_2. On the other hand, the lesser band bending in ZnPc on ML-MoS_2 facilitates in the larger delocalization size of the S_1 exciton, which can enable coherent CT even though the exciton is farther away from the interface.

Back electron transfer vs exciton dissociation

After the initial CT process in sub-fs time scale for both bulk and ML-MoS_2 samples, we observed T_1 exciton formation in ZnPc – bulk-MoS_2 system *via* spin flipping in MoS_2 and BET to ZnPc, whereas free charge carriers were generated in ZnPc – ML-MoS_2 system. The T_1 formation kinetics for a 1 nm-ZnPc – bulk-MoS_2 sample is reproduced in Figure 5.9c (black tace). The spectral signature of the T_1 exciton is distinctive compared to other states as it shows an intense intensity rise and has a very long lifetime (100's of ps). However, such T_1 state is not observed for the ZnPc – ML-MoS_2 interface. The longest-lived state identifiable in the 1 nm ZnPc – ML-MoS_2 spectrum is the CT_0 state. For comparison with bulk, the intensity evolution of this state is shown in Figure 5.9c (red trace). After the intensity is peaked at ~ 2 ps, it decreases monotonically with time. Hence, we do not observe the signature for the BET and T_1 formation at the ZnPc – ML-MoS_2 interface.

For the ZnPc – bulk-MoS_2 interface, we suggest two factors that favor the T_1 formation. First, the large band bending in the ZnPc film on bulk-MoS_2 can essentially trap the hole of the CT exciton very close to the interface (Figure 5.9e). Note that the hole has tendency to move to higher energy states in contrast to electron that tends to relax to lower energy states. The close proximity of the hole in ZnPc to the electron in MoS_2 can increase the chances of the BET rather

than the separation. Indeed, the exchange interaction that provides the energetic driving force for the T_1 formation is a very short-range interaction (within the size of a molecule). Hence, hole trapping at the interface would be a crucial step for T_1 formation *via* the BET. The concept of the band bending to explain the T_1 formation has been recently invoked at CuPc – GaAs interface.[158] Second, the spin lifetime is supposed to be longer in ML-MoS_2 as compared to bulk-MoS_2 because of spin-momentum locking in ML-MoS_2.[152, 159] Indeed, recent works on ML-TMDC heterostructures have shown that CT excitons in these heterostructures can have a very long spin lifetime.[160]

We do not observe significant T_1 formation in ZnPc – ML-MoS_2. Instead, the CT_0 intensity is found to decay on the order of 10s of ps (Fig. 5.9e). The disappearance of the CT_0 is due to exciton dissociation with the holes in ZnPc and the electrons in MoS_2. Details on exciton dissociation are explained in section 5.3.3. From the interfacial energy landscape perspective, the ZnPc – ML-MoS_2 has less band bending (~ 0.2 eV) (Figure 5.9e). In addition, the energy offset between S_1 – CBM is less. This creates an even energy landscape at ZnPc – ML-MoS_2 interface which promotes the delocalization size of exciton. Unlike the pinning of hole at the interface in bulk system, the hole can go farther away from the interface, eventually causing the exciton dissociation.

5.3.5 Charge transfer at ZnPc – bulk-WS_2 interface

We also investigated the CT dynamics at the ZnPc−bulk WSe_2 interface. The experimental conditions were kept similar to ZnPc – bulk-MoS_2 sample. The indirect gap of bulk WSe_2 is taken to be 1.2 eV.[161] Figure 5.10a shows type I band alignment is formed at the interface of ZnPc−bulk WSe_2 as determined from our UPS technique. Figure 5.10b is the TR-TPPE spectrum for the 1 nm ZnPc on the WSe_2 sample. A short-lived S_1 state at ~1.7 eV can be

observed. Similar to the ZnPc−MoS_2 interface, the decay of the S_1 signal can be assigned to the CT from ZnPc to WSe_2.

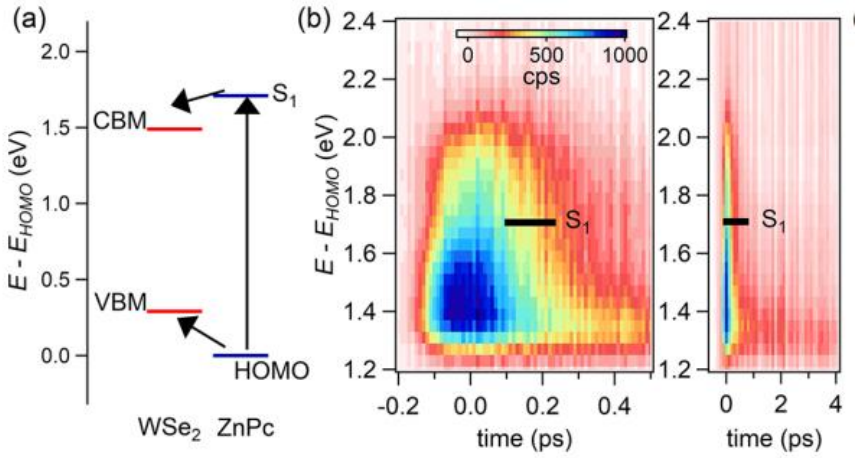

Figure 5.10: (a) Type I band alignment at the ZnPc−bulk WSe_2 interface measured by UPS experiment. Both electron and hole transfer occurs from ZnPc to WSe_2 (b) TR-TPPE spectrum for the 1 nm ZnPc−WSe_2 sample. "Figures adapted from reference [146].[146] Copyright (2017) American Chemical Society."

Notably, the long-lived T_1 state was not observed in the ZnPc−WSe_2 spectrum because type-I band alignment allows both electron transfer and hole transfer from ZnPc to WSe_2 to occur. Without a hole in ZnPc, BET from WSe_2 to ZnPc is not energetically feasible. Thus, the formation of T_1 excitons is not possible.

5.4 Summary

We thoroughly studied the CT dynamics at ZnPc – ML-MoS_2 and ZnPc – bulk-MoS_2 system. Both the system had type II band alignment, a pre-requisite for exciton dissociation. However, exciton dissociation was only observed in ZnPc – ML-MoS_2 system. In ZnPc – bulk-MoS_2 system, long-lived T_1 excitons were formed *via* faster spin flipping and BET from MoS_2 to ZnPc. Thus, type II band alignment alone is not enough to determine the fate of CT excitons. We demonstrated that the interfacial energetics, together with the spin lifetime in the TMDCs, can

govern the exciton dynamics. At first, we observed that for the thin films of ZnPc, VBM_{MoS2} – $HOMO_{ZnPc}$ energy offset was found to be similar at the interface despite of large energy offset between the VB-edges of ML and bulk. In addition, larger band bending of ZnPc was observed in ZnPc – bulk-MoS_2 system that limited the size of coherent CT. By contrast, the smaller band bending and comparatively larger size of coherent CT in ZnPc – ML-MoS_2 system was observed. The band bending played a critical role in determining the interfacial electron dynamics. The hole in ZnPc was trapped at the interface due to the large potential gradient associated with the stronger band bending, which favored the BET and formation of T_1 excitons. On the other hand, the flatter band structure at the ZnPc – ML-MoS_2 interface along with the longer spin lifetime in ML-MoS_2 favored the dissociation of the CT excitons. In general, we demonstrated that the potential energy landscape has a significant role in governing the spatial range of the coherent interfacial CT process and the subsequent evolution of the CT excitons.

6. Conclusion and Outlook

6.1 Introduction

Solar energy is one promising renewable energy source for sustainable energy in the future. One method for converting solar energy into electricity is the use of organic photovoltaics, which have gained increasing attention due to their low cost production and flexibility. However, one obstacle for the commercial application of organic photovoltaics is its low efficiency that arises from ineffective splitting of excitons into free carriers. The ultimate efficiency of these devices correlates with how effectively free charge carriers can be generated from bound charge transfer excitons (CT excitons) at donor–acceptor interfaces. Numerous theoretical and experimental attempts have been made to understand the exciton dissociation (ED) mechanism. The plausible mechanisms for ED that stem from these attempts base on concepts such as entropy,[20, 79, 82-83] electric field, structural and energetic disorder,[162-163] crystallinity,[22] molecular orientation,[164-167] energy landscape at the interface,[168-171] molecular aggregate size and packing,[76] vibronic coupling,[84, 172] and delocalization size of wavefunction.[28, 55, 75] Both the "hot CT pathway" and "cold CT pathway" have been proposed as a route for the ED[78-81, 91-92]. Indeed, the underlying mechanism for the effective ED remains unclear. The pursuit of heterostructures for efficient ED pathway continues.

The motivation of this dissertation is to investigate the underlying mechanism for effective ED process at donor–acceptor interfaces. Among several claimed mechanims for effective ED, our study focuses mainly on investigating the roles of size and orientation of electron-hole wavefunction, and the energy landscape at the interface. Whether CT exciton recombines or separates directly relates to the exciton binding energy, which in turn depends on

the exciton delocalization size. The greater the delocalization size, the smaller the binding energy is between electron and hole, and hence ED is more likely. By using time resolved-two photon photoemission spectroscopy (TR-TPPE) technique, we probe temporal evolution of both energy and delocalization size of the CT excitons with fs temporal and nm spatial resolution (see Chapter 3). Our technique provides unprecedented details on how CT exciton evolves in time and space.

6.2 Summary of the experimental results

First, we summarize results from the wavefunction orientation dependence study (see chapter 4). The study was done on three different hybrid interfaces: F_8ZnPc – ZnPc on HOPG (face-on), F_8ZnPc – ZnPc on SiO_2/Si (edge-on) and ZnPc – C_{60} on Au (edge-on ZnPc). Interfaces with face-on and edge-on orientations of the same pair of donor and acceptor molecules (ZnPc and F_8ZnPc) were fabricated without any chemical modification. Moreover, the use of a non-fullerene planar acceptor molecule (F_8ZnPc) could have the potential to achieve better ED efficiency and solar cell efficiency than that with fullerene acceptors. has better orientation directionality over the widely used spherically symmetric fullerene acceptor, and enhances cell efficiency.[173-174] For the third system, ZnPc has an edge-on orientation on the C_{60} crystal. Excitingly, contrasting exciton behaviors were observed in the two different orientations despite the type II band alignment was found in all three systems. For the face-on molecular orientation, where both electron and hole wavefunctions are delocalized along normal direction of the interface, dissociation of CT excitons into free charge carriers (uphill energy process) was observed. On the other hand, the relaxation of the hot CT excitons to lower energy (downhill energy process) CT excitons was observed in the two interfaces with the edge-on orientation.

For the ZnPc – C_{60} interface, the coexistence of two CT states with different energies was observed after the relaxation of hot CT exciton. The CT exciton delocalization size is larger for the higher energy CT states. While the delocalized hot CT state could facilitate effective ED, a mechanism to quickly extract the charge from hot CT state is needed because the hot CT excitons have a short lifetime (< 1ps). Nevertheless, it is reported that cold exciton can dissociate *via* thermal activation,[90] but the yield for charge generation from cold excitons is low because it is too slow to compete with other recombination channels. Hence, we conclude that interfaces with face-on stacking are likely to provide efficient kinetic pathway for ED.

Moreover, we investigated the role of interfacial energy landscape on the ED dynamics using organic – TMD interfaces (ZnPc – bulk-MoS_2 and ZnPc – ML-MoS_2) as model systems (see chapter 5). This study is motivated from the fact that interfacial electronic states can govern electron dynamics and play a substantial role in ED process. ZnPc maintains face-on orientation on both bulk and ML MoS_2. Both interfaces have type II band alignment. Although CT from ZnPc to MoS_2 occurs at both interfaces on sub-fs timescale, the two interfaces exhibit very different exciton dynamics following the initial CT. This difference can be explained by considering the different amount of band bending in the ZnPc film deposited on ML-MoS_2 and bulk-MoS_2. At the ZnPc – ML-MoS_2 interface, CT excitons dissociate into free electrons and holes in ~ 10 ps. Such free charge carrier generation is attributed to the less band bending in ZnPc (~ 0.2 eV) deposited on ML-MoS_2. On the contrary, back electron transfer (BET) from bulk-MoS_2 to ZnPc is observed, which results in the formation of T_1 excitons in the ZnPc layer. This is explained by the larger band bending in ZnPc (> 0.5 eV) deposited on bulk-MoS_2, which caused hole trapping near the interface and the BET. The shorter spin lifetime in bulk-MoS_2 compared to ML-MoS_2 makes the triplet formation process kinetically favorable. Our finding

suggests that less band bending is favored for the separation of CT excitons, and hence the effective exciton generation. In addition, the type II band alignment at the interface by itself cannot be a sole predictor for determining whether free carriers can be generated effectively from the interface.

6.3 Closing remarks and future direction

Exciton dissociation at organic-based interfaces has been studied extensively for more than a decade; however, the dissociation mechanism is still intriguing. We have made our sincere efforts to understand the exciton dissociation mechanism *via* control of wavefunction orientation at interface. We demonstrated that certain geometrical constraint imposed on delocalized electron and hole wavefunction orientation enhances ED process. Next, we investigated organic – TMDs, a new class of mixed van der Waals heterostructure, to understand the role of interfacial energetics on ED process. Even energy landscape at the interface was favorable for coherent transport and free charge carrier generation. We hope our experimental findings will be helpful in understanding the fundamentals of effective exciton dissociation mechanism and will interest the readers, especially those working in the field of organic-based heterostructures.

In future, the concept of multilayer and energy level cascade structure applied in organic – organic and TMD – TMDs to effectively extract charge carriers could be employed in organic – TMDs heterostructures. More importantly, organic – TMDs can be easily stacked by van der Waals interaction and benefit by utilizing the complimentary properties of each other. The heterostructures can even come up with the new properties, which neither material possess. However, identifying interesting properties of the heterostructures from abundant sources of organic and TMDs would be challenging, but it can establish them as a promising flexible material in photovoltaic and optoelectronics fields.

References

1. EERE, The History of Solar. Energy, U. S. D. o., Ed. Office of Energy Efficiency and Renewable Energy: N/A; pp 1-12.

2. Devices, A. Alta Devices sets 29.1% solar efficiency record; NASA selects Alta Devices for International Space Station Test. https://www.altadevices.com/solar-world-record-nasa-selects-alta-devices/.

3. NREL Best Research Cell Eficiency Chart. https://www.nrel.gov/pv/cell-efficiency.html (accessed 2019).

4. Feldman, D. M., Robert, Solar Industry Update Q4/2018 Q1/2019. NREL, Ed. DOE: 2019.

5. Bagher, A. M., Comparison of organic solar cells and inorganic solar cells. *Int J Renew Sustain Energy* **2014,** *3*, 53-58.

6. Friend, R.; Gymer, R.; Holmes, A.; Burroughes, J.; Marks, R.; Taliani, C.; Bradley, D.; Dos Santos, D.; Bredas, J.; Lögdlund, M., Electroluminescence in conjugated polymers. *Nature* **1999,** *397* (6715), 121-128.

7. Shaheen, S. E.; Radspinner, R.; Peyghambarian, N.; Jabbour, G. E., Fabrication of bulk heterojunction plastic solar cells by screen printing. *Applied Physics Letters* **2001,** *79* (18), 2996-2998.

8. Spanggaard, H.; Krebs, F. C., A brief history of the development of organic and polymeric photovoltaics. *Solar Energy Materials and Solar Cells* **2004,** *83* (2), 125-146.

9. Ameri, T.; Li, N.; Brabec, C. J., Highly efficient organic tandem solar cells: a follow up review. *Energy & Environmental Science* **2013,** *6* (8), 2390-2413.

10. Aryanpour, K.; Muñoz, J. A.; Mazumdar, S., Does Singlet Fission Enhance the Performance of Organic Solar Cells? *The Journal of Physical Chemistry C* **2013,** *117* (10), 4971-4979.

11. Weiss, L. R.; Bayliss, S. L.; Kraffert, F.; Thorley, K. J.; Anthony, J. E.; Bittl, R.; Friend, R. H.; Rao, A.; Greenham, N. C.; Behrends, J., Strongly exchange-coupled triplet pairs in an organic semiconductor. *Nat Phys* **2016,** *advance online publication*.

12. Scharber, M. C.; Sariciftci, N. S., Efficiency of bulk-heterojunction organic solar cells. *Progress in polymer science* **2013,** *38* (12), 1929-1940.

13. Knupfer, M., Exciton binding energies in organic semiconductors. *Applied Physics A* **2003,** *77* (5), 623-626.

14. Qi, B.; Wang, J., Open-circuit voltage in organic solar cells. *Journal of Materials Chemistry* **2012,** *22* (46), 24315-24325.

15. Yao, J.; Kirchartz, T.; Vezie, M. S.; Faist, M. A.; Gong, W.; He, Z.; Wu, H.; Troughton, J.; Watson, T.; Bryant, D., Quantifying losses in open-circuit voltage in solution-processable solar cells. *Physical review applied* **2015,** *4* (1), 014020.

16. Rand, B. P.; Burk, D. P.; Forrest, S. R., Offset energies at organic semiconductor heterojunctions and their influence on the open-circuit voltage of thin-film solar cells. *Physical Review B* **2007,** *75* (11), 115327.

17. Arkhipov, V.; Heremans, P.; Bässler, H., Why is exciton dissociation so efficient at the interface between a conjugated polymer and an electron acceptor? *Applied Physics Letters* **2003,** *82* (25), 4605-4607.

18. Beljonne, D.; Cornil, J.; Muccioli, L.; Zannoni, C.; Brédas, J.-L.; Castet, F., Electronic Processes at Organic− Organic Interfaces: Insight from Modeling and Implications for Opto-electronic Devices†. *Chemistry of Materials* **2010,** *23* (3), 591-609.

19. Wilke, A.; Amsalem, P.; Frisch, J.; Bro¨ ker, B.; Vollmer, A.; Koch, N., Electric fields induced by energy level pinning at organic heterojunctions. *Applied Physics Letters* **2011,** *98* (12), 123304.

20. Gregg, B. A., Entropy of charge separation in organic photovoltaic cells: The benefit of higher dimensionality. *The Journal of Physical Chemistry Letters* **2011,** *2* (24), 3013-3015.

21. Chen, W.; Xu, T.; He, F.; Wang, W.; Wang, C.; Strzalka, J.; Liu, Y.; Wen, J.; Miller, D. J.; Chen, J., Hierarchical nanomorphologies promote exciton dissociation in polymer/fullerene bulk heterojunction solar cells. *Nano letters* **2011,** *11* (9), 3707-3713.

22. Vandewal, K.; Oosterbaan, W. D.; Bertho, S.; Vrindts, V.; Gadisa, A.; Lutsen, L.; Vanderzande, D.; Manca, J. V., Varying polymer crystallinity in nanofiber poly (3-

alkylthiophene): PCBM solar cells: Influence on charge-transfer state energy and open-circuit voltage. *Applied Physics Letters* **2009,** *95* (12), 123303.

23. Strobel, T.; Deibel, C.; Dyakonov, V., Role of polaron pair diffusion and surface losses in organic semiconductor devices. *Physical review letters* **2010,** *105* (26), 266602.

24. Gregg, B. A., Charged defects in soft semiconductors and their influence on organic photovoltaics. *Soft Matter* **2009,** *5* (16), 2985-2989.

25. Park, S. H.; Roy, A.; Beaupre, S.; Cho, S.; Coates, N.; Moon, J. S.; Moses, D.; Leclerc, M.; Lee, K.; Heeger, A. J., Bulk heterojunction solar cells with internal quantum efficiency approaching 100&percnt. *Nature photonics* **2009,** *3* (5), 297-302.

26. Bakulin, A. A.; Rao, A.; Pavelyev, V. G.; van Loosdrecht, P. H.; Pshenichnikov, M. S.; Niedzialek, D.; Cornil, J.; Beljonne, D.; Friend, R. H., The role of driving energy and delocalized states for charge separation in organic semiconductors. *Science* **2012,** *335* (6074), 1340-1344.

27. Heeger, A. J., 25th anniversary article: bulk heterojunction solar cells: understanding the mechanism of operation. *Advanced Materials* **2014,** *26* (1), 10-28.

28. Savoie, B. M.; Rao, A.; Bakulin, A. A.; Gelinas, S.; Movaghar, B.; Friend, R. H.; Marks, T. J.; Ratner, M. A., Unequal Partnership: Asymmetric Roles of Polymeric Donor and Fullerene Acceptor in Generating Free Charge. *J. Am. Chem. Soc.* **2014,** *136* (7), 2876-2884.

29. Hertz, H., Ueber einen Einfluss des ultravioletten Lichtes auf die electrische Entladung. *Annalen der Physik* **1887,** *267* (8), 983-1000.

30. Einstein, A., Zur elektrodynamik bewegter körper. *Annalen der physik* **1905,** *322* (10), 891-921.

31. Hüfner, S., Photoelectron spectroscopy: principles and applications. **1995**.

32. Hüfner, S., *Photoelectron spectroscopy: principles and applications*. Springer Science & Business Media: 2013.

33. Damascelli, A.; Hussain, Z.; Shen, Z.-X., Angle-resolved photoemission studies of the cuprate superconductors. *Reviews of modern physics* **2003,** *75* (2), 473.

34. Conversion, L. Orpheus-N, Non-Collinear Optical Parametric Amplifier. http://lightcon.com/Product/ORPHEUS-N.html.

35. Kafle, T. R.; Wang, T.; Kattel, B.; Liu, Q.; Gong, Y.; Wu, J.; Chan, W.-L., Hot Exciton Relaxation and Exciton Trapping in Single-Walled Carbon Nanotube Thin Films. *The Journal of Physical Chemistry C* **2016,** *120* (42), 24482-24490.

36. Bartels, L., Tailoring molecular layers at metal surfaces. *Nature chemistry* **2010,** *2* (2), 87-95.

37. Xiao, K.; Deng, W.; Keum, J. K.; Yoon, M.; Vlassiouk, I. V.; Clark, K. W.; Li, A.-P.; Kravchenko, I. I.; Gu, G.; Payzant, E. A., Surface-induced orientation control of CuPc molecules for the epitaxial growth of highly ordered organic crystals on graphene. *Journal of the American Chemical Society* **2013,** *135* (9), 3680-3687.

38. Thayer, G.; Sadowski, J.; Zu Heringdorf, F. M.; Sakurai, T.; Tromp, R., Role of surface electronic structure in thin film molecular ordering. *Physical review letters* **2005,** *95* (25), 256106.

39. Savoie, B. M.; Jackson, N. E.; Chen, L. X.; Marks, T. J.; Ratner, M. A., Mesoscopic Features of Charge Generation in Organic Semiconductors. *Acc. Chem. Res.* **2014,** *47* (11), 3385-3394.

40. Bredas, J. L.; Norton, J. E.; Cornil, J.; Coropceanu, V., Molecular Understanding of Organic Solar Cells: The Challenges. *Acc. Chem. Res.* **2009,** *42* (11), 1691-1699.

41. Ponseca, C. S.; Chabera, P.; Uhlig, J.; Persson, P.; Sundstrom, V., Ultrafast Electron Dynamics in Solar Energy Conversion. *Chem. Rev.* **2017,** *117* (16), 10940-11024.

42. Caruso, D.; Troisi, A., Long-range exciton dissociation in organic solar cells. *Proc. Natl. Acad. Sci. USA* **2012,** *109* (34), 13498-13502.

43. Ma, H. B.; Troisi, A., Direct Optical Generation of Long-Range Charge-Transfer States in Organic Photovoltaics. *Adv. Mater.* **2014,** *26* (35), 6163-6167.

44. D'Avino, G.; Muccioli, L.; Olivier, Y.; Beljonne, D., Charge Separation and Recombination at Polymer-Fullerene Heterojunctions: Delocalization and Hybridization Effects. *J. Phys. Chem. Lett.* **2016,** *7* (3), 536-540.

45. Huix-Rotllant, M.; Tamura, H.; Burghardt, I., Concurrent Effects of Delocalization and Internal Conversion Tune Charge Separation at Regioregular Polythiophene-Fullerene Heterojunctions. *J. Phys. Chem. Lett.* **2015,** *6* (9), 1702-1708.

46. Yao, Y.; Zhou, N. J.; Prior, J.; Zhao, Y., Competition between diagonal and off-diagonal coupling gives rise to charge-transfer states in polymeric solar cells. *Sci. Rep.* **2015,** *5*, 14555.

47. Gelinas, S.; Rao, A.; Kumar, A.; Smith, S. L.; Chin, A. W.; Clark, J.; van der Poll, T. S.; Bazan, G. C.; Friend, R. H., Ultrafast Long-Range Charge Separation in Organic Semiconductor Photovoltaic Diodes. *Science* **2014,** *343* (6170), 512-516.

48. Barker, A. J.; Chen, K.; Hodgkiss, J. M., Distance Distributions of Photogenerated Charge Pairs in Organic Photovoltaic Cells. *J. Am. Chem. Soc.* **2014,** *136* (34), 12018-12026.

49. Devizis, A.; De Jonghe-Risse, J.; Hany, R.; Nuesch, F.; Jenatsch, S.; Gulbinas, V.; Moser, J. E., Dissociation of Charge Transfer States and Carrier Separation in Bilayer Organic Solar Cells: A Time-Resolved Electroabsorption Spectroscopy Study. *J. Am. Chem. Soc.* **2015,** *137* (25), 8192-8198.

50. Bernardo, B.; Cheyns, D.; Verreet, B.; Schaller, R. D.; Rand, B. P.; Giebink, N. C., Delocalization and dielectric screening of charge transfer states in organic photovoltaic cells. *Nat. Commun.* **2014,** *5*, 3245.

51. Zusan, A.; Vandewal, K.; Allendorf, B.; Hansen, N. H.; Pflaum, J.; Salleo, A.; Dyakonov, V.; Deibel, C., The Crucial Influence of Fullerene Phases on Photogeneration in Organic Bulk Heterojunction Solar Cells. *Adv. Energy Mater.* **2014,** *4* (17), 1400922.

52. Pensack, R. D.; Guo, C. H.; Vakhshouri, K.; Gomez, E. D.; Asbury, J. B., Influence of Acceptor Structure on Barriers to Charge Separation in Organic Photovoltaic Materials. *J. Phys. Chem. C* **2012,** *116* (7), 4824-4831.

53. Dutton, G.; Quinn, D. P.; Lindstrom, C. D.; Zhu, X. Y., Exciton dynamics at molecule-metal interfaces: C-60/Au(111). *Phys. Rev. B* **2005,** *72* (4), 045441.

54. Chan, W. L.; Tritsch, J.; Dolocan, A.; Ligges, M.; Miaja-Avila, L.; Zhu, X. Y., Communication: Momentum-resolved quantum interference in optically excited surface states. *J. Chem. Phys.* **2011,** *135* (3), 031101.

55. Wang, T.; Kafle, T. R.; Kattel, B.; Chan, W.-L., A Multidimensional View of Charge Transfer Excitons at Organic Donor–Acceptor Interfaces. *J. Am. Chem. Soc.* **2017,** *139* (11), 4098-4106.

56. Wang, T.; Kafle, T. R.; Kattel, B.; Liu, Q.; Wu, J.; Chan, W.-L., Growing Ultra-flat Organic Films on Graphene with a Face-on Stacking via Moderate Molecule-Substrate Interaction. *Scientific Reports* **2016,** *6*.

57. Dutton, G.; Jin, W.; Reutt-Robey, J.; Robey, S., Ultrafast charge-transfer processes at an oriented phthalocyanine/C 60 interface. *Physical Review B* **2010,** *82* (7), 073407.

58. Huang, H.; Chen, W.; Chen, S.; Qi, D. C.; Gao, X. Y.; Wee, A. T. S., Molecular orientation of CuPc thin films on C 60/Ag (111). *Applied Physics Letters* **2009,** *94* (16), 112.

59. Chen, W.; Huang, H.; Chen, S.; Huang, Y. L.; Gao, X. Y.; Wee, A. T. S., Molecular orientation-dependent ionization potential of organic thin films. *Chemistry of Materials* **2008,** *20* (22), 7017-7021.

60. Duhm, S.; Heimel, G.; Salzmann, I.; Glowatzki, H.; Johnson, R. L.; Vollmer, A.; Rabe, J. P.; Koch, N., Orientation-dependent ionization energies and interface dipoles in ordered molecular assemblies. *Nat. Mater.* **2008,** *7* (4), 326-332.

61. Wang, T.; Kafle, T. R.; Kattel, B.; Liu, Q. F.; Wu, J.; Chan, W. L., Growing Ultra-flat Organic Films on Graphene with a Face-on Stacking via Moderate Molecule-Substrate Interaction. *Sci. Rep.* **2016,** *6*, 28895.

62. Duhm, S.; Heimel, G.; Salzmann, I.; Glowatzki, H.; Johnson, R. L.; Vollmer, A.; Rabe, J. P.; Koch, N., Orientation-dependent ionization energies and interface dipoles in ordered molecular assemblies. *Nature materials* **2008,** *7* (4), 326.

63. Wang, T.; Chan, W.-L., Dynamical localization limiting the coherent transport range of excitons in organic crystals. *The journal of physical chemistry letters* **2014,** *5* (11), 1812-1818.

64. Takahashi, T.; Suzuki, S.; Morikawa, T.; Katayamayoshida, H.; Hasegawa, S.; Inokuchi, H.; Seki, K.; Kikuchi, K.; Suzuki, S.; Ikemoto, K.; Achiba, Y., Pseudo-Gap at the Fermi Level in K3c60 Observed by Photoemission and Inverse Photoemission. *Phys. Rev. Lett.* **1992,** *68* (8), 1232-1235.

65. Davidson, A. T., The Effect of the Metal Atom on the Absorption-Spectra of Phthalocyanine Films. *J. Chem. Phys.* **1982,** *77* (1), 168-172.

66. Ozawa, Y.; Nakayama, Y.; Machida, S.; Kinjo, H.; Ishii, H., Maximum probing depth of low-energy photoelectrons in an amorphous organic semiconductor film. *J. Electron. Spectrosc. Relat. Phenom.* **2014,** *197*, 17-21.

67. Chan, W. L.; Ligges, M.; Jailaubekov, A.; Kaake, L.; Miaja-Avila, L.; Zhu, X. Y., Observing the Multiexciton State in Singlet Fission and Ensuing Ultrafast Multielectron Transfer. *Science* **2011,** *334* (6062), 1541-1545.

68. Jailaubekov, A. E.; Willard, A. P.; Tritsch, J. R.; Chan, W. L.; Sai, N.; Gearba, R.; Kaake, L. G.; Williams, K. J.; Leung, K.; Rossky, P. J.; Zhu, X. Y., Hot charge-transfer excitons set the time limit for charge separation at donor/acceptor interfaces in organic photovoltaics. *Nat. Mater.* **2013,** *12* (1), 66-73.

69. Wang, T.; Kafle, T. R.; Kattel, B.; Chan, W. L., Observation of an Ultrafast Exciton Hopping Channel in Organic Semiconducting Crystals. *J. Phys. Chem. C* **2016,** *120* (14), 7491-7499.

70. Kafle, T. R.; Wang, T.; Kattel, B.; Liu, Q.; Gong, Y.; Wu, J.; Chan, W.-L., Hot Exciton Relaxation and Exciton Trapping in Single-Walled Carbon Nanotube Thin Films. *J. Phys. Chem. C* **2016,** *120* (42), 24482-24490.

71. Wang, T.; Chan, W. L., Dynamical Localization Limiting the Coherent Transport Range of Excitons in Organic Crystals. *J. Phys. Chem. Lett.* **2014,** *5* (11), 1812-1818.

72. Kafle, T. R.; Kattel, B.; Wang, T.; Chan, W.-L., The relationship between the coherent size, binding energy and dissociation dynamics of charge transfer excitons at organic interfaces. *Journal of Physics: Condensed Matter* **2018,** *30* (45), 454001.

73. Schwalb, C. H.; Sachs, S.; Marks, M.; Scholl, A.; Reinert, F.; Umbach, E.; Hofer, U., Electron lifetime in a Shockley-type metal-organic interface state. *Phys. Rev. Lett.* **2008,** *101* (14), 146801.

74. Caplins, B. W.; Suich, D. E.; Shearer, A. J.; Harris, C. B., Metal/Phthalocyanine Hybrid Interface States on Ag(111). *J. Phys. Chem. Lett.* **2014,** *5* (10), 1679-1684.

75. Huix-Rotllant, M.; Tamura, H.; Burghardt, I., Concurrent effects of delocalization and internal conversion tune charge separation at regioregular polythiophene–fullerene heterojunctions. *The journal of physical chemistry letters* **2015,** *6* (9), 1702-1708.

76. Jakowetz, A. C.; Böhm, M. L.; Zhang, J.; Sadhanala, A.; Huettner, S.; Bakulin, A. A.; Rao, A.; Friend, R. H., What controls the rate of ultrafast charge transfer and charge separation efficiency in organic photovoltaic blends. *Journal of the American Chemical Society* **2016,** *138* (36), 11672-11679.

77. Green, M. A.; Hishikawa, Y.; Warta, W.; Dunlop, E. D.; Levi, D. H.; Hohl-Ebinger, J.; Ho-Baillie, A. W., Solar cell efficiency tables (version 50). *Progress in Photovoltaics* **2017,** *25* (NREL/JA-5J00-68932).

78. Brédas, J.-L.; Norton, J. E.; Cornil, J.; Coropceanu, V., Molecular understanding of organic solar cells: the challenges. *Accounts of chemical research* **2009,** *42* (11), 1691-1699.

79. Clarke, T. M.; Durrant, J. R., Charge photogeneration in organic solar cells. *Chemical reviews* **2010,** *110* (11), 6736-6767.

80. Ponseca Jr, C. S.; Chabera, P.; Uhlig, J.; Persson, P.; Sundstrom, V., Ultrafast electron dynamics in solar energy conversion. *Chemical reviews* **2017,** *117* (16), 10940-11024.

81. Ostroverkhova, O., Organic optoelectronic materials: mechanisms and applications. *Chemical reviews* **2016,** *116* (22), 13279-13412.

82. Gélinas, S.; Rao, A.; Kumar, A.; Smith, S. L.; Chin, A. W.; Clark, J.; van der Poll, T. S.; Bazan, G. C.; Friend, R. H., Ultrafast long-range charge separation in organic semiconductor photovoltaic diodes. *Science* **2014,** *343* (6170), 512-516.

83. Monahan, N. R.; Williams, K. W.; Kumar, B.; Nuckolls, C.; Zhu, X.-Y., Direct observation of entropy-driven electron-hole pair separation at an organic semiconductor interface. *Physical review letters* **2015,** *114* (24), 247003.

84. Falke, S. M.; Rozzi, C. A.; Brida, D.; Maiuri, M.; Amato, M.; Sommer, E.; De Sio, A.; Rubio, A.; Cerullo, G.; Molinari, E., Coherent ultrafast charge transfer in an organic photovoltaic blend. *Science* **2014,** *344* (6187), 1001-1005.

85. Chen, S.; Tsang, S. W.; Lai, T. H.; Reynolds, J. R.; So, F., Dielectric effect on the photovoltage loss in organic photovoltaic cells. *Advanced Materials* **2014,** *26* (35), 6125-6131.

86. Chen, W.; Qi, D. C.; Huang, Y. L.; Huang, H.; Wang, Y. Z.; Chen, S.; Gao, X. Y.; Wee, A. T. S., Molecular orientation dependent energy level alignment at organic− organic heterojunction interfaces. *The Journal of Physical Chemistry C* **2009,** *113* (29), 12832-12839.

87. Schwarze, M.; Tress, W.; Beyer, B.; Gao, F.; Scholz, R.; Poelking, C.; Ortstein, K.; Gunther, A. A.; Kasemann, D.; Andrienko, D.; Leo, K., Band structure engineering in organic semiconductors. *Science* **2016,** *352* (6292), 1446-9.

88. Zahn, D. R.; Gavrila, G. N.; Gorgoi, M., The transport gap of organic semiconductors studied using the combination of direct and inverse photoemission. *Chemical Physics* **2006,** *325* (1), 99-112.

89. Ozawa, Y.; Nakayama, Y.; Machida, S. i.; Kinjo, H.; Ishii, H., Maximum probing depth of low-energy photoelectrons in an amorphous organic semiconductor film. *Journal of Electron Spectroscopy and Related Phenomena* **2014,** *197*, 17-21.

90. Kattel, B.; Qin, L.; Kafle, T. R.; Chan, W.-L., Graphene Field-Effect Transistor as a High-Throughput Platform to Probe Charge Separation at Donor–Acceptor Interfaces. *The journal of physical chemistry letters* **2018,** *9* (7), 1633-1641.

91. Bässler, H.; Köhler, A., "Hot or cold": how do charge transfer states at the donor–acceptor interface of an organic solar cell dissociate? *Physical Chemistry Chemical Physics* **2015,** *17* (43), 28451-28462.

92. Kocherzhenko, A. A.; Lee, D.; Forsuelo, M. A.; Whaley, K. B., Coherent and incoherent contributions to charge separation in multichromophore systems. *The Journal of Physical Chemistry C* **2015,** *119* (14), 7590-7603.

93. Jailaubekov, A. E.; Willard, A. P.; Tritsch, J. R.; Chan, W.-L.; Sai, N.; Gearba, R.; Kaake, L. G.; Williams, K. J.; Leung, K.; Rossky, P. J., Hot charge-transfer excitons set

the time limit for charge separation at donor/acceptor interfaces in organic photovoltaics. *Nature materials* **2013,** *12* (1), 66.

94. Grancini, G.; Maiuri, M.; Fazzi, D.; Petrozza, A.; Egelhaaf, H.; Brida, D.; Cerullo, G.; Lanzani, G., Hot exciton dissociation in polymer solar cells. *Nature materials* **2013,** *12* (1), 29-33.

95. Lee, J.; Vandewal, K.; Yost, S. R.; Bahlke, M. E.; Goris, L.; Baldo, M. A.; Manca, J. V.; Van Voorhis, T., Charge transfer state versus hot exciton dissociation in polymer− fullerene blended solar cells. *Journal of the American Chemical Society* **2010,** *132* (34), 11878-11880.

96. van der Hofstad, T. G.; Di Nuzzo, D.; van den Berg, M.; Janssen, R. A.; Meskers, S. C., Influence of Photon Excess Energy on Charge Carrier Dynamics in a Polymer-Fullerene Solar Cell. *Advanced Energy Materials* **2012,** *2* (9), 1095-1099.

97. Vandewal, K.; Albrecht, S.; Hoke, E. T.; Graham, K. R.; Widmer, J.; Douglas, J. D.; Schubert, M.; Mateker, W. R.; Bloking, J. T.; Burkhard, G. F., Efficient charge generation by relaxed charge-transfer states at organic interfaces. *Nature materials* **2014,** *13* (1), 63.

98. Novoselov, K. S.; Jiang, D.; Schedin, F.; Booth, T.; Khotkevich, V.; Morozov, S.; Geim, A. K., Two-dimensional atomic crystals. *Proceedings of the National Academy of Sciences* **2005,** *102* (30), 10451-10453.

99. Guo, Y.; Robertson, J., Band engineering in transition metal dichalcogenides: Stacked versus lateral heterostructures. *Applied Physics Letters* **2016,** *108* (23), 233104.

100. Novoselov, K. S.; Mishchenko, A.; Carvalho, A.; Neto, A. H. C., 2D materials and van der Waals heterostructures. *Science* **2016,** *353* (6298), 461.

101. Zhang, W. J.; Wang, Q. X.; Chen, Y.; Wang, Z.; Wee, A. T. S., Van der Waals stacked 2D layered materials for optoelectronics. *2D Mater.* **2016,** *3* (2), 022001.

102. Das, S.; Robinson, J. A.; Dubey, M.; Terrones, H.; Terrones, M., Beyond Graphene: Progress in Novel Two-Dimensional Materials and van der Waals Solids. *Annu Rev Mater Res* **2015,** *45*, 1-27.

103. Ceballos, F.; Bellus, M. Z.; Chiu, H.-Y.; Zhao, H., Ultrafast charge separation and indirect exciton formation in a MoS2–MoSe2 van der Waals heterostructure. *ACS nano* **2014,** *8* (12), 12717-12724.

104. Lee, C. H.; Schiros, T.; Santos, E. J. G.; Kim, B.; Yager, K. G.; Kang, S. J.; Lee, S.; Yu, J.; Watanabe, K.; Taniguchi, T.; Hone, J.; Kaxiras, E.; Nuckolls, C.; Kim, P., Epitaxial Growth of Molecular Crystals on van der Waals Substrates for High-Performance Organic Electronics. *Adv. Mater.* **2014,** *26* (18), 2812-2817.

105. Jo, S. B.; Kim, H. H.; Lee, H.; Kang, B.; Lee, S.; Sim, M.; Kim, M.; Lee, W. H.; Cho, K., Boosting Photon Harvesting in Organic Solar Cells with Highly Oriented Molecular Crystals via Graphene-Organic Heterointerface. *Acs Nano* **2015,** *9* (8), 8206-8219.

106. Jariwala, D.; Marks, T. J.; Hersam, M. C., Mixed-dimensional van der Waals heterostructures. *Nature materials* **2017,** *16* (2), 170-181.

107. Huang, Y. L.; Zheng, Y. J.; Song, Z. B.; Chi, D. Z.; Wee, A. T. S.; Quek, S. Y., The organic-2D transition metal dichalcogenide heterointerface. *Chem. Soc. Rev.* **2018,** *47* (9), 3241-3264.

108. Wang, H. M.; Li, C. H.; Fang, P. F.; Zhang, Z. L.; Zhang, J. Z., Synthesis, properties, and optoelectronic applications of two-dimensional MoS2 and MoS2-based heterostructures. *Chem. Soc. Rev.* **2018,** *47* (16), 6101-6127.

109. Sun, J.; Choi, Y.; Choi, Y. J.; Kim, S.; Park, J.-H.; Lee, S.; Cho, J. H., 2D-Organic Hybrid Heterostructures for Optoelectronic Applications. *Adv. Mater.* **2019**, 1803831.

110. Choi, M. S.; Qu, D.; Lee, D.; Liu, X.; Watanabe, K.; Taniguchi, T.; Yoo, W. J., Lateral MoS2 p-n Junction Formed by Chemical Doping for Use in High-Performance Optoelectronics. *ACS Nano* **2014,** *8* (9), 9332-9340.

111. Li, H. M.; Lee, D.; Qu, D. S.; Liu, X. C.; Ryu, J. J.; Seabaugh, A.; Yoo, W. J., Ultimate thin vertical p-n junction composed of two-dimensional layered molybdenum disulfide. *Nat. Commun.* **2015,** *6*, 6564.

112. Yu, Z. H.; Pan, Y. M.; Shen, Y. T.; Wang, Z. L.; Ong, Z. Y.; Xu, T.; Xin, R.; Pan, L. J.; Wang, B. G.; Sun, L. T.; Wang, J. L.; Zhang, G.; Zhang, Y. W.; Shi, Y.; Wang, X. R., Towards intrinsic charge transport in monolayer molybdenum disulfide by defect and interface engineering. *Nat. Commun.* **2014,** *5*, 5290.

113. Li, Q.; Zhao, Y. H.; Ling, C. Y.; Yuan, S. J.; Chen, Q.; Wang, J. L., Towards a Comprehensive Understanding of the Reaction Mechanisms Between Defective MoS2 and Thiol Molecules. *Angew Chem Int Edit* **2017,** *56* (35), 10501-10505.

114. Lee, C. H.; Schiros, T.; Santos, E. J.; Kim, B.; Yager, K. G.; Kang, S. J.; Lee, S.; Yu, J.; Watanabe, K.; Taniguchi, T., Epitaxial growth of molecular crystals on van der Waals substrates for high-performance organic electronics. *Advanced Materials* **2014,** *26* (18), 2812-2817.

115. Kang, S. J.; Lee, G. H.; Yu, Y. J.; Zhao, Y.; Kim, B.; Watanabe, K.; Taniguchi, T.; Hone, J.; Kim, P.; Nuckolls, C., Organic field effect transistors based on graphene and hexagonal boron nitride heterostructures. *Advanced Functional Materials* **2014,** *24* (32), 5157-5163.

116. Wang, L.; Wu, M., Electron spin relaxation due to D'yakonov-Perel'and Elliot-Yafet mechanisms in monolayer MoS 2: role of intravalley and intervalley processes. *Physical Review B* **2014,** *89* (11), 115302.

117. Chen, X.; Yan, T.; Zhu, B.; Yang, S.; Cui, X., Optical control of spin polarization in monolayer transition metal dichalcogenides. *ACS nano* **2017,** *11* (2), 1581-1587.

118. Petoukhoff, C. E.; Krishna, M. B. M.; Voiry, D.; Bozkurt, I.; Deckoff-Jones, S.; Chhowalla, M.; O'Carroll, D. M.; Dani, K. M., Ultrafast Charge Transfer and Enhanced Absorption in MoS2-Organic van der Waals Heterojunctions Using Plasmonic Metasurfaces. *ACS Nano* **2016,** *10* (11), 9899-9908.

119. Homan, S. B.; Sangwan, V. K.; Balla, I.; Bergeron, H.; Weiss, E. A.; Hersam, M. C., Ultrafast Exciton Dissociation and Long-Lived Charge Separation in a Photovoltaic Pentacene-MoS2 van der Waals Heterojunction. *Nano Lett.* **2017,** *17* (1), 164-169.

120. Kafle, T. R.; Kattel, B.; Lane, S. D.; Wang, T.; Zhao, H.; Chan, W. L., Charge Transfer Exciton and Spin Flipping at Organic-Transition-Metal Dichalcogenide Interfaces. *ACS Nano* **2017,** *11* (10), 10184-10192.

121. Zhong, C. M.; Sangwan, V. K.; Wang, C.; Bergeron, H.; Hersam, M. C.; Weiss, E. A., Mechanisms of Ultrafast Charge Separation in a PTB7/Monolayer MoS2 van der Waals Heterojunction. *J. Phys. Chem. Lett.* **2018,** *9* (10), 2484-2491.

122. Zhu, T.; Yuan, L.; Zhao, Y.; Zhou, M. W.; Wan, Y.; Mei, J. G.; Huang, L. B., Highly mobile charge-transfer excitons in two-dimensional WS2/tetracene heterostructures. *Sci Adv* **2018,** *4* (1), 3104.

123. Zhang, Z.; Yates Jr, J. T., Band bending in semiconductors: chemical and physical consequences at surfaces and interfaces. *Chemical reviews* **2012,** *112* (10), 5520-5551.

124. Akaike, K.; Koch, N.; Oehzelt, M., Fermi level pinning induced electrostatic fields and band bending at organic heterojunctions. *Applied Physics Letters* **2014,** *105* (22), 181_1.

125. Yang, L.; Sinitsyn, N. A.; Chen, W.; Yuan, J.; Zhang, J.; Lou, J.; Crooker, S. A., Long-lived nanosecond spin relaxation and spin coherence of electrons in monolayer MoS 2 and WS 2. *Nature Physics* **2015,** *11* (10), 830.

126. Kafle, T. R.; Kattel, B.; Yao, P.; Zereshki, P.; Zhao, H.; Chan, W.-L., Effect of the Interfacial Energy Landscape on Photo-induced Charge Generation at the ZnPc-MoS2 Interface. *Journal of the American Chemical Society* **2019**.

127. Padilha, J. E.; Peelaers, H.; Janotti, A.; Van de Walle, C. G., Nature and evolution of the band-edge states in MoS2: From monolayer to bulk. *Phys. Rev. B* **2014,** *90* (20), 205420.

128. Yeh, P. C.; Jin, W. C.; Zaki, N.; Zhang, D. T.; Liou, J. T.; Sadowski, J. T.; Al-Mahboob, A.; Dadap, J. I.; Herman, I. P.; Sutter, P.; Osgood, R. M., Layer-dependent electronic structure of an atomically heavy two-dimensional dichalcogenide. *Phys. Rev. B* **2015,** *91* (4), 041407.

129. Mak, K. F.; Lee, C.; Hone, J.; Shan, J.; Heinz, T. F., Atomically Thin MoS2: A New Direct-Gap Semiconductor. *Phys. Rev. Lett.* **2010,** *105* (13), 136805.

130. England, C. D.; Collins, G. E.; Schuerlein, T. J.; Armstrong, N. R., Epitaxial Thin-Films of Large Organic-Molecules - Characterization of Phthalocyanine and Coronene Overlayers on the Layered Semiconductors Mos2 and Sns2. *Langmuir* **1994,** *10* (8), 2748-2756.

131. Franzen, H. F.; Umaña, M. X.; McCreary, J.; Thorn, R., XPS spectra of some transition metal and alkaline earth monochalcogenides. *Journal of Solid State Chemistry* **1976,** *18* (4), 363-368.

132. Kam, K.; Parkinson, B., Detailed photocurrent spectroscopy of the semiconducting group VI transition metal dichalcogenides. *Journal of Physical Chemistry* **1982,** *86* (4), 463-467.

133. Han, S. W.; Cha, G.-B.; Frantzeskakis, E.; Razado-Colambo, I.; Avila, J.; Park, Y. S.; Kim, D.; Hwang, J.; Kang, J. S.; Ryu, S., Band-gap expansion in the surface-localized electronic structure of MoS 2 (0002). *Physical Review B* **2012,** *86* (11), 115105.

134. McMenamin, J.; Spicer, W., Photoemission studies of layered transition-metal dichalcogenides: Mo S 2. *Physical Review B* **1977,** *16* (12), 5474.

135. Han, S. W.; Cha, G. B.; Frantzeskakis, E.; Razado-Colambo, I.; Avila, J.; Park, Y. S.; Kim, D.; Hwang, J.; Kang, J. S.; Ryu, S.; Yun, W. S.; Hong, S. C.; Asensio, M. C., Band-gap expansion in the surface-localized electronic structure of MoS2(0002). *Phys. Rev. B* **2012,** *86* (11), 115105.

136. Zahid, F.; Liu, L.; Zhu, Y.; Wang, J.; Guo, H., A generic tight-binding model for monolayer, bilayer and bulk MoS2. *Aip Adv* **2013,** *3* (5).

137. Choi, J.; Zhang, H. Y.; Choi, J. H., Modulating Optoelectronic Properties of Two Dimensional Transition Metal Dichalcogenide Semiconductors by Photoinduced Charge Transfer. *ACS Nano* **2016,** *10* (1), 1671-1680.

138. Canton-Vitoria, R.; Gobeze, H. B.; Blas-Ferrando, V. M.; Ortiz, J.; Jang, Y.; Fernández-Lázaro, F.; Sastre-Santos, Á.; Nakanishi, Y.; Shinohara, H.; D'Souza, F.; Tagmatarchis, N., Excited-State Charge Transfer in Covalently Functionalized MoS2 with a Zinc Phthalocyanine Donor–Acceptor Hybrid. *Angew. Chem.* **2019,** *131* (17), 5768-5773.

139. Liu, X. Y.; Xie, X. Y.; Fang, W. H.; Cui, G. L., Theoretical Insights into Interfacial Electron Transfer between Zinc Phthalocyanine and Molybdenum Disulfide. *J. Phys. Chem. A* **2018,** *122* (50), 9587-9596.

140. Amsterdam, S. H.; Stanev, T. K.; Zhou, Q.; Lou, A. J. T.; Bergeron, H.; Darancet, P.; Hersam, M. C.; Stern, N. P.; Marks, T. J., Electronic Coupling in Metallophthalocyanine–

Transition Metal Dichalcogenide Mixed-Dimensional Heterojunctions. *ACS Nano* **2019,** *13* (4), 4183-4190.

141. Oehzelt, M.; Akaike, K.; Koch, N.; Heimel, G., Energy-level alignment at organic heterointerfaces. *Sci Adv* **2015,** *1* (10), 1501127.

142. Wang, T.; Liu, Q. F.; Caraiani, C.; Zhang, Y. P.; Wu, J.; Chan, W. L., Effect of Interlayer Coupling on Ultrafast Charge Transfer from Semiconducting Molecules to Mono- and Bilayer Graphene. *Phys. Rev. Appl.* **2015,** *4* (1), 014016.

143. Jnawali, G.; Rao, Y.; Beck, J. H.; Petrone, N.; Kymissis, I.; Hone, J.; Heinz, T. F., Observation of Ground- and Excited-State Charge Transfer at the C-60/Graphene Interface. *Acs Nano* **2015,** *9* (7), 7175-7185.

144. Yoshino, K.; Hikida, M.; Tatsuno, K.; Kaneto, K.; Inuishi, Y., Emission-Spectra of Phthalocyanine Crystals. *J. Phys. Soc. Jpn.* **1973,** *34* (2), 441-445.

145. Sharma, D.; Huijser, A.; Savolainen, J.; Steen, G.; Herek, J. L., Active and passive control of zinc phthalocyanine photodynamics. *Faraday discussions* **2013,** *163*, 433-445.

146. Kafle, T. R.; Kattel, B.; Lane, S. D.; Wang, T.; Zhao, H.; Chan, W.-L., Charge Transfer Exciton and Spin Flipping at Organic–Transition-Metal Dichalcogenide Interfaces. *ACS nano* **2017,** *11* (10), 10184-10192.

147. Johannsen, J. C.; Ulstrup, S.; Cilento, F.; Crepaldi, A.; Zacchigna, M.; Cacho, C.; Turcu, I. C. E.; Springate, E.; Fromm, F.; Raidel, C.; Seyller, T.; Parmigiani, F.; Grioni, M.;

Hofmann, P., Direct View of Hot Carrier Dynamics in Graphene. *Phys. Rev. Lett.* **2013,** *111* (2), 027403.

148. Cheiwchanchamnangij, T.; Lambrecht, W. R. L., Quasiparticle band structure calculation of monolayer, bilayer, and bulk MoS2. *Phys. Rev. B* **2012,** *85* (20), 205302.

149. Liu, X.; Gu, J.; Ding, K.; Fan, D.; Hu, X.; Tseng, Y.-W.; Lee, Y.-H.; Menon, V.; Forrest, S. R., Photoresponse of an organic semiconductor/two-dimensional transition metal dichalcogenide heterojunction. *Nano letters* **2017,** *17* (5), 3176-3181.

150. Liu, X.; Gu, J.; Ding, K.; Fan, D. J.; Hu, X. E.; Tseng, Y. W.; Lee, Y. H.; Menon, V.; Forrest, S. R., Photoresponse of an Organic Semiconductor/Two-Dimensional Transition Metal Dichalcogenide Heterojunction. *Nano Lett.* **2017,** *17* (5), 3176-3181.

151. Riley, J. M.; Mazzola, F.; Dendzik, M.; Michiardi, M.; Takayama, T.; Bawden, L.; Granerod, C.; Leandersson, M.; Balasubramanian, T.; Hoesch, M.; Kim, T. K.; Takagi, H.; Meevasana, W.; Hofmann, P.; Bahramy, M. S.; Wells, J. W.; King, P. D. C., Direct observation of spin-polarized bulk bands in an inversion-symmetric semiconductor. *Nat. Phys.* **2014,** *10* (11), 835-839.

152. Wang, L.; Wu, M. W., Electron spin relaxation due to D'yakonov-Perel' and Elliot-Yafet mechanisms in monolayer MoS2: Role of intravalley and intervalley processes. *Phys. Rev. B* **2014,** *89* (11), 115302.

153. Liu, H. L.; Shen, C. C.; Su, S. H.; Hsu, C. L.; Li, M. Y.; Li, L. J., Optical properties of monolayer transition metal dichalcogenides probed by spectroscopic ellipsometry. *Appl. Phys. Lett.* **2014,** *105* (20), 201905.

154. Ceballos, F.; Bellus, M. Z.; Chiu, H. Y.; Zhao, H., Ultrafast Charge Separation and Indirect Exciton Formation in a MoS2-MoSe2 van der Waals Heterostructure. *ACS Nano* **2014,** *8* (12), 12717-12724.

155. Peng, B.; Yu, G. N.; Liu, X. F.; Liu, B.; Liang, X.; Bi, L.; Deng, L. J.; Sum, T. C.; Loh, K. P., Ultrafast charge transfer in MoS2/WSe2 p-n Heterojunction. *2D Mater.* **2016,** *3* (2), 025020.

156. Norton, J. E.; Bredas, J. L., Theoretical characterization of titanyl phthalocyanine as a p-type organic semiconductor: Short intermolecular pi-pi interactions yield large electronic couplings and hole transport bandwidths. *J. Chem. Phys.* **2008,** *128* (3), 034701.

157. Tant, J.; Geerts, Y. H.; Lehmann, M.; De Cupere, V.; Zucchi, G.; Laursen, B. W.; Bjornholm, T.; Lemaur, V.; Marcq, V.; Burquel, A.; Hennebicq, E.; Gardebien, F.; Viville, P.; Beljonne, D.; Lazzaroni, R.; Cornil, J., Liquid crystalline metal-free phthalocyanines designed for charge and exciton transport. *J. Phys. Chem. B* **2005,** *109* (43), 20315-20323.

158. Lim, H.; Kwon, H.; Kim, S. K.; Kim, J. W., Delayed Triplet-State Formation through Hybrid Charge Transfer Exciton at Copper Phthalocyanine/GaAs Heterojunction. *The journal of physical chemistry letters* **2017,** *8* (19), 4763-4768.

159. Yang, L. Y.; Sinitsyn, N. A.; Chen, W. B.; Yuan, J. T.; Zhang, J.; Lou, J.; Crooker, S. A., Long-lived nanosecond spin relaxation and spin coherence of electrons in monolayer MoS2 and WS2. *Nat. Phys.* **2015,** *11* (10), 830-834.

160. Jin, C. H.; Kim, J.; Utama, M. I. B.; Regan, E. C.; Kleemann, H.; Cai, H.; Shen, Y. X.; Shinner, M. J.; Sengupta, A.; Watanabe, K.; Taniguchi, T.; Tongay, S.; Zettl, A.; Wang, F., Imaging of pure spin-valley diffusion current in WS2-WSe2 heterostructures. *Science* **2018,** *360* (6391), 893-896.

161. Traving, M.; Boehme, M.; Kipp, L.; Skibowski, M.; Starrost, F.; Krasovskii, E.; Perlov, A.; Schattke, W., Electronic structure of WSe 2: A combined photoemission and inverse photoemission study. *Physical Review B* **1997,** *55* (16), 10392.

162. Shi, L.; Lee, C. K.; Willard, A. P., The Enhancement of Interfacial Exciton Dissociation by Energetic Disorder Is a Nonequilibrium Effect. *ACS central science* **2017,** *3* (12), 1262-1270.

163. Govatski, J.; da Luz, M.; Koehler, M., Anomalous maximum and minimum for the dissociation of a geminate pair in energetically disordered media. *Chemical Physics Letters* **2015,** *620*, 123-128.

164. Tumbleston, J. R.; Collins, B. A.; Yang, L.; Stuart, A. C.; Gann, E.; Ma, W.; You, W.; Ade, H., The influence of molecular orientation on organic bulk heterojunction solar cells. *Nature Photonics* **2014,** *8* (5), 385.

165. Jo, J. W.; Jung, J. W.; Ahn, H.; Ko, M. J.; Jen, A. K. Y.; Son, H. J., Effect of Molecular Orientation of Donor Polymers on Charge Generation and Photovoltaic Properties in Bulk Heterojunction All-Polymer Solar Cells. *Advanced Energy Materials* **2017,** *7* (1), 1601365.

166. Ran, N. A.; Roland, S.; Love, J. A.; Savikhin, V.; Takacs, C. J.; Fu, Y.-T.; Li, H.; Coropceanu, V.; Liu, X.; Brédas, J.-L., Impact of interfacial molecular orientation on radiative recombination and charge generation efficiency. *Nature communications* **2017,** *8* (1), 79.

167. Lee, H.; Lee, D.; Sin, D. H.; Kim, S. W.; Jeong, M. S.; Cho, K., Effect of donor–acceptor molecular orientation on charge photogeneration in organic solar cells. *NPG Asia Materials* **2018,** *10* (6), 469.

168. McMahon, D. P.; Cheung, D. L.; Troisi, A., Why holes and electrons separate so well in polymer/fullerene photovoltaic cells. *The Journal of Physical Chemistry Letters* **2011,** *2* (21), 2737-2741.

169. Bartelt, J. A.; Beiley, Z. M.; Hoke, E. T.; Mateker, W. R.; Douglas, J. D.; Collins, B. A.; Tumbleston, J. R.; Graham, K. R.; Amassian, A.; Ade, H., The importance of fullerene percolation in the mixed regions of polymer–fullerene bulk heterojunction solar cells. *Advanced Energy Materials* **2013,** *3* (3), 364-374.

170. Westacott, P.; Tumbleston, J. R.; Shoaee, S.; Fearn, S.; Bannock, J. H.; Gilchrist, J. B.; Heutz, S.; DeMello, J.; Heeney, M.; Ade, H., On the role of intermixed phases in organic photovoltaic blends. *Energy & Environmental Science* **2013,** *6* (9), 2756-2764.

171. Burke, T. M.; McGehee, M. D., How high local charge carrier mobility and an energy cascade in a three-phase bulk heterojunction enable> 90% Quantum Efficiency. *Advanced Materials* **2014,** *26* (12), 1923-1928.

172. De Sio, A.; Lienau, C., Vibronic coupling in organic semiconductors for photovoltaics. *Physical Chemistry Chemical Physics* **2017,** *19* (29), 18813-18830.

173. Hou, J.; Inganäs, O.; Friend, R. H.; Gao, F., Organic solar cells based on non-fullerene acceptors. *Nature materials* **2018,** *17* (2), 119.

174. Cheng, P.; Li, G.; Zhan, X.; Yang, Y., Next-generation organic photovoltaics based on non-fullerene acceptors. *Nature Photonics* **2018,** *12* (3), 131-142.